UNIVERSIDADE TÉCNICA DE LISBOA
INSTITUTO SUPERIOR TÉCNICO

On the stability and magnetic microstructure of $YFe_{11-x}Ti_y$, $YFe_{11-x}Mo_y$, and $NdFe_{11-x}Ti_y$ compounds

Daniela da Silva Nunes
Licenciada

Dissertação para obtenção do Grau de Mestre em Ciência e Engenharia de Materiais

Abril de 2008

CONTENTS

Abstract

Microstructures and magnetic domain configurations in Y:11Fe:Ti, Y:11Fe:Mo and Nd:11Fe:Ti polycrystalline aggregates have been investigated by transmission electron microscopy, Lorentz microscopy, magnetic force microscopy and magnetization measurements. The materials were prepared by arc-melting or splat-quenching and have crystallized adopting essentially the $ThMn_{12}$ structure. However, the presence of α-Fe(Ti) and α-Fe(Mo), even after long annealing treatments, indicates that the $RFe_{11}M$ stoichiometry is not strictly followed under equilibrium.

In fine splat-quenched $RFe_{11-x}M_y$ crystallites the domain walls are energetically unfavourable in the structure and have been expelled to the grain boundaries. Large $RFe_{11-x}M_y$ grains present internal domain walls forming stripe/maze patterns characteristic of high anisotropy materials, while large α-Fe(Ti) and α-Fe(Mo) grains exhibit non-equilibrium vortex configurations related to the magnetization of adjacent $RFe_{11-x}M_y$ grains. Induction mapping determined from Fresnel images indicated the presence of Bloch and Néel character in the vortex walls. Domain wall energy of 8-17 erg/cm^2 has been estimated for $YFe_{11-x}Ti_y$. Twins and antiphase boundaries have been observed in $RFe_{11-x}M_y$ grains but showed weak or no interaction with domain walls, justifying the low coercivity of the materials. A random distribution of planar defects on (022) planes was extensively present in the $ThMn_{12}$-type $NdFe_{11-x}Ti_y$ phase. These defects originate from a partly displacive $ThMn_{12}$-type $NdFe_{11-x}Ti_y$ $\rightarrow$ Th_2Zn_{17}-type $Nd_2(Fe,Ti)_{17-w}$ solid state transformation.

Key-words: $ThMn_{12}$ compounds, magnetic domain configurations, vortex configurations, planar defects, Lorentz microscopy, magnetic force microscopy, magnetization measurements.

3

Resumo

As microestruturas e as configurações de domínios magnéticos em agregados policristalinos de Y:11Fe:Ti, Y:11Fe:Mo e Nd:11Fe:Ti foram investigadas por microscopia electrónica de transmissão, microscopia de Lorentz, microscopia de força magnética e medidas de magnetização. Os materiais foram preparados por fusão em forno de arco ou arrefecimento rápido, e cristalizaram adoptando essencialmente a estrutura $ThMn_{12}$. No entanto, a presença de α-Fe(Ti) e α-Fe(Mo) depois de tratamentos térmicos longos, indica que em condições de equilíbrio a estequiometria $RFe_{11}M$ não é seguida.

Em microestruturas finas, as paredes de domínios magnéticos revelaram-se energeticamente desfavoráveis, tendo sido expelidas para os limites de grão. Grãos grosseiros de $RFe_{11-x}M_y$ apresentaram paredes de domínios formando padrões do tipo listas/labiríntos, característicos de materiais de elevada anisotropia, enquanto grãos grosseiros de α-Fe(Ti) e de α-Fe(Mo) exibiram configurações vortex metaestáveis, relacionadas com a magnetização de grãos adjacentes. Mapas de indução, calculados a partir de imagens de Fresnel, indicaram a presença de carácter Bloch e Néel nas paredes de domínio dos vórtices. Estimou-se uma energia de parede de domínio entre 8 e 17 erg/cm^2 para $YFe_{11-x}Ti_y$. Foram observadas maclas e fronteiras de antifase em grãos de $RFe_{11-x}M_y$. Estes defeitos cristalográficos apresentaram fraca ou nenhuma interacção com as paredes de domínio, justificando a baixa coercividade dos materiais. A fase $NdFe_{11-x}Ti_y$, com estrutura do tipo $ThMn_{12}$, apresentou uma distribuição aleatória de defeitos planares nos planos (022). A presença destes defeitos teve origem numa transformação de fase de estado sólido da estrutura $ThMn_{12}$ para a estrutura Th_2Zn_{17}, que possui um carácter parcialmente deslocativo.

Palavras-chave: configurações de domínios magnéticos, configurações vortex, defeitos planares, microscopia de Lorentz, microscopia de força magnética, medidas de magnetização.

Acknowledgments

1. Introduction

Rare-earths (R) are a relatively abundant group of elements, which are generally considered to include scandium and yttrium as well as the lanthanide series. These elements are used in the manufacture of permanent magnets, automobile catalytic converters and catalysts for petroleum refining, and are also employed as alloying elements in metals.

Rare-earth intermetallic compounds adopting the $ThMn_{12}$ structure have attracted considerable attention in the field of permanent magnets due to their relatively high Curie temperature, saturation magnetization and magnetocrystalline anisotropy [1-2]. Iron based $ThMn_{12}$-type systems are regarded as having the greatest potential of the class, since iron has a large magnetic moment (2.1 μ_B per atom) and low cost. The discovery that interstitial atoms, such as nitrogen, carbon and hydrogen can lead to a considerable improvement of the magnetic properties has further increased the interest in this class of compounds [3-7].

RMn_{12} binary intermetallics crystallize with the $ThMn_{12}$ prototype structure, yet no binary RT_{12} compound exists for T metals such as Fe, Co and Ni. In these cases, the system can be stabilized by partially replacing T with M, an early 3d element (Ti, V or Cr) or other non-magnetic element (Al, Si, Mo, W or Re). The $ThMn_{12}$ structure belongs to the *I4/mmm* space group and contains 26 atoms per unit cell. In $RT_{12-x}M_x$ ternary compounds, the rare-earth atoms occupy the *2a* Th sites, while the T and M atoms are distributed over the *8f*, *8j* and *8i* Mn sites (Table 1 and Figure 1). In the specific case of $RFe_{12-x}M_x$ compounds, Fe atoms fully occupy the *8f* and *8j* sites, while *8i* sites are populated by a mixture of Fe and M atoms (except for Si that tends to replace Fe in the *8f* positions).

Table 1 – Crystallographic information for $ThMn_{12}$ $RFe_{12-x}M_x$ structures [1].

Elements	Atomic Positions	*x*	*y*	*z*
R	*2a*	0.000	0.000	0.000
Fe	*8f*	0.250	0.250	0.250
Fe	*8j*	0.277	0.500	0.000

| Fe/M | 8i | 0.361 | 0.000 | 0.000 |
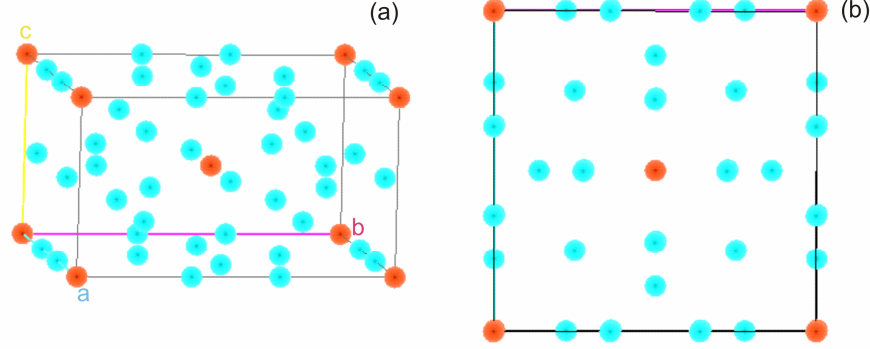
Figure 1 – (a) Cell of the ThMn$_{12}$ structure. (b) Projection view of the ThMn$_{12}$ cell along the *c* axis. The red atoms correspond to Th and the blues ones to Mn.

Among the iron-based ThMn$_{12}$-type systems, the RFe$_{11}$Ti and RFe$_{11}$Mo series have been extensively investigated in order to evaluate the temperature dependence of the magnetic properties and to clarify the existence and nature of field-induced magnetic transitions [5-35]. However, only very limited studies have been reported on the microstructure [36-38] and magnetic domain configurations [39-41] of these materials. In addition, scarce direct observation seems to have been carried out for the rest of the whole class of RT$_{12-x}$M$_x$ compounds [42-48].

In the present work, polycrystalline aggregates with the nominal Y:11Fe:Ti, Y:11Fe:Mo, and Nd:11Fe:Ti compositions, prepared by arc melting and splat-quenching, have been studied by X-ray diffraction (XRD), scanning and transmission electron microscopy (respectively SEM and TEM), Lorentz microscopy under Fresnel mode (LTEM), atomic force microscopy (AFM) and magnetization measurements.

2. Methods

2.1. X-Ray diffraction analysis

When X-rays are scattered by an atom, the atom re-radiates waves with the same frequency; this phenomenon is known as the Rayleigh scattering (or elastic scattering). Re-emitted waves from atomic structures with long range order interfere with each other either constructively or destructively, producing a regular interference pattern or diffraction pattern. Interference is constructive when the phase shift is proportional to 2π (see Figure 2); this condition is expressed by Bragg's law:

$$n\lambda = 2d_{hkl}.sin\theta \tag{1}$$

where n is an integer, λ is the wavelength of X-rays, d is the spacing between the planes in the atomic lattice, and θ is the angle between the incident ray and the scattering planes.
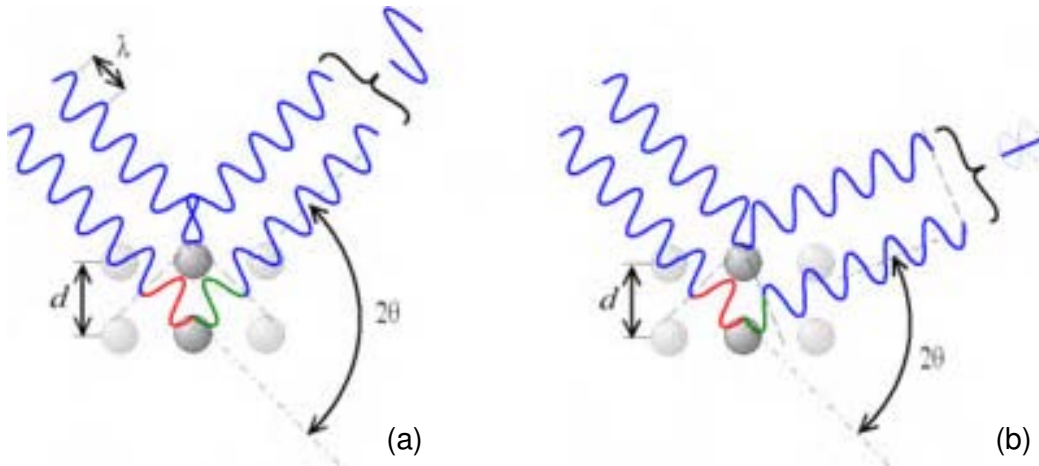
Figure 2 – According to the wave path difference, $2d_{hkl}.sin\theta$, the phase shift causes either (a) constructive or (b) destructive interference.

An X-ray diffractometer comprises a source of X-rays, a diffractometer assembly, together with X-ray data collection and analysis systems. The diffractometer assembly controls the alignment of the beam, as well as the position and orientation of both the specimen and the X-ray detector.

In the X-ray source, X-rays are generated by accelerating a beam of electrons on to a pure metal target contained in a vacuum ampoule. The high-energy electrons eject ground-state electrons from the atoms of the target material and refilling of these ground states induces X-ray emission. When an electron from a K-shell is displaced, it leaves a vacancy, which destabilises the atom, and an electron from a higher-energy level will tend to occupy the vacancy. If the electron is provided by the L-shell, the transfer corresponds to the emission of a K_α photon with energy equal to the difference between the K and L shells (see Figure 3). Such a transfer results also in a vacancy being created in the L-shell which in turn can be filled by an M-shell electron, with emission of a L_α photon. If the electron vacancy on the K shell would be filled by an M-shell electron, a K_β photon would be generated. Emission of this radiation allows the atom to return to a more stable energy-state. The specific energy of the emitted radiation is *characteristic* of the atoms present in the target material. Photons generated by decelerating collisions are also produced, and result in a continuous distribution of energies and wavelengths in the X-rays emitted from the target, known as white radiation.
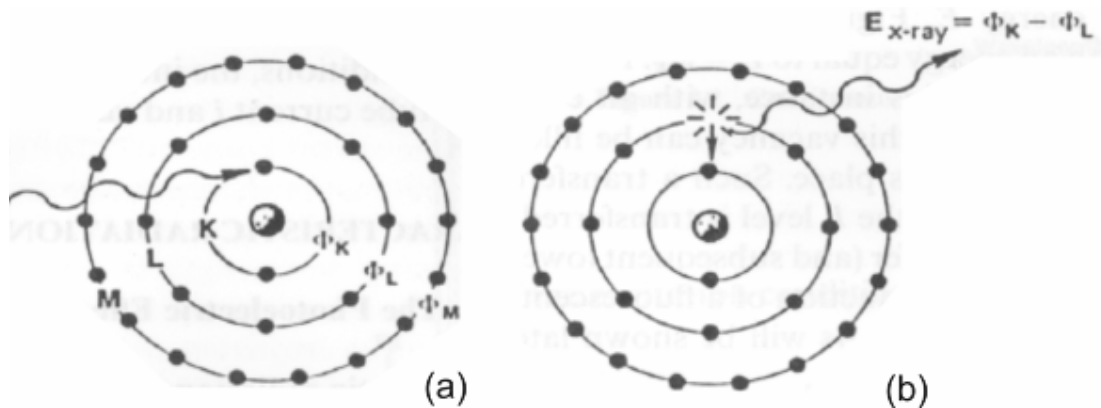
Figure 3 - K, L or M-shells, and emission of X-rays during the refilling of ground states. The energy of the electron beam must be sufficient to displace electrons in the K, L or M shells of the atoms present in the target, which haveΦ binding energies.

X-ray diffraction experiments with polycrystalline materials usually require monochromatic radiation. Monochromatic radiation is generated by exciting the K-radiation from a pure metal target and then filtering the beam by interposing a foil that strongly absorbs both the white radiation and the β-component of the K-radiation, without any appreciable reduction of the α-component.

In a powder or polycrystalline diffractometer, divergent K_α rays exit the source and hit the sample at different points on its surface. After the diffraction process, the rays are refocused at the detector slit. The incident X-ray beam and diffracted beam slits move on a circle centred on the sample (see Figure 4). The angle between the incident and Bragg diffracted beams is equal to 2θ, whereas the sample is at θ to the incident X-ray beam. This is called the Bragg-Bretano geometry. The diffracted radiation is recorded by an X-ray detector mounted on the diffractometer goniometer stage and rotated about the sample.
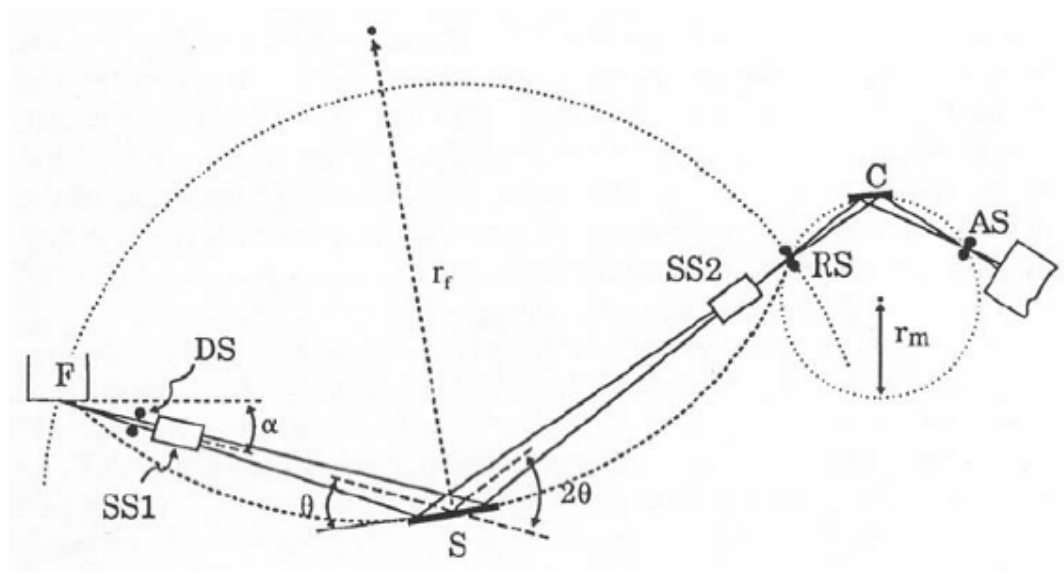
Figure 4 – Schematic representation of a sample mounted on a goniometer stage which can be rotated about one or more axis, and a detector which travels along the focusing circle in the Bragg-Brentano geometry. F is the X-ray source, DS is the divergence scatter slit, SS is the soller slit assembly (SS1 on "tube" side, SS2 on detector side). RS is the receiving slit, C is the monochromator crystal, r_m is the radius of the monochromator circle on which RS, C and AS (the detector slit) lie, r_f is the radius of the focusing circle. F, S and RS all fall on this circle. The angles are indicated [49].

2.2. Electron microscopy

When electrons are accelerated up to high energy levels (few tens to hundreds keV) and focused on a material, they can scatter or backscatter elastically or inelastically, and produce various interactions, source of other signals types such as secondary electrons, transmitted electrons, X-rays, Auger electrons and light (Figure 5). The several signal types generated can be detected to produce images, diffraction patterns and electromagnetic spectra in electron microscopy. The working principles of scanning electron microscopy and transmission electron microscopy will be briefly described in the following sections.
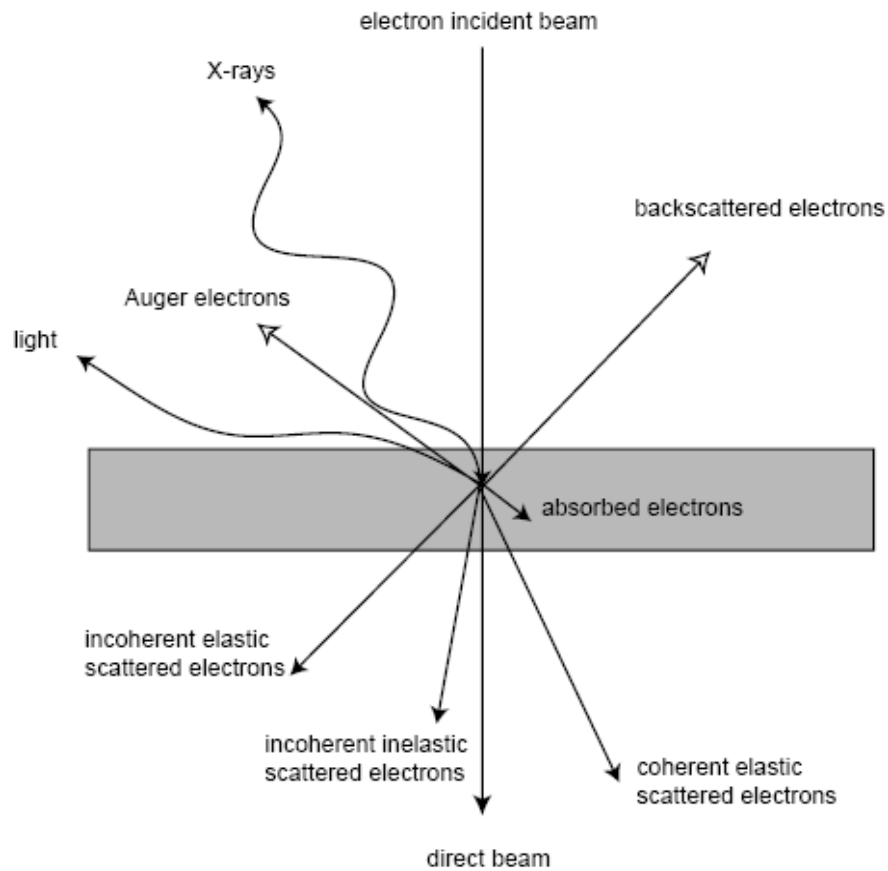
Figure 5 – Beam-specimen interactions.

2.2.1. Scanning electron microscopy

Scanning electron microscopy is capable of producing images with resolution around 1 nm. The scanning electron microscope includes a source of high-energy electrons (thermionically emitted from a tungsten or lanthanum hexaboride cathode or alternatively generated via field emission) which are accelerated towards an anode; and a condenser system, composed by electromagnetic lenses to focus the electron beam into a fine probe (sized 1 nm to 5 nm) that impinges on the specimen. The so-called "objective" lens, the ultimate electromagnetic probe lens, determines the resolution attainable by the microscope; however the probe lens is placed above the specimen, and has no part in collecting the image signal. The beam passes through pairs of scanning coils, which deflect the beam horizontally and vertically (see Figure 6) so that it scans in a raster fashion over a rectangular area of the sample surface.

Figure 6 – Image and diagram of a scanning electron microscope.

In the case of bulk samples when the primary electron beam is focused on the material, the electrons lose energy by repeated scattering and absorption within a teardrop-shaped volume of the specimen known as the interaction volume, which extends from less than 100 nm to around 5 µm into the sample. The size of the interaction volume (see Figure 7) depends on the beam accelerating voltage, the atomic number of the specimen and the specimen´s density.
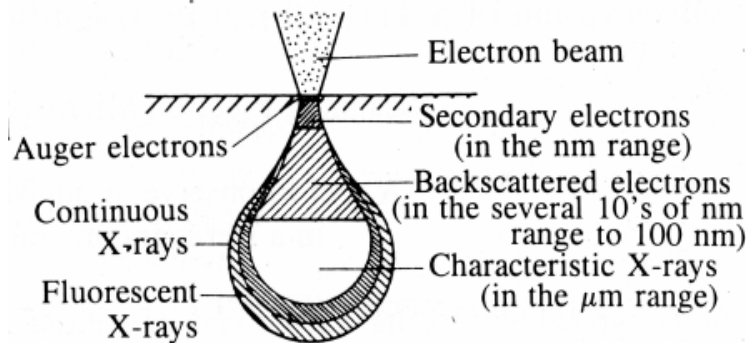
Figure 7 – Interaction teardrop volume with indication of signal origin.

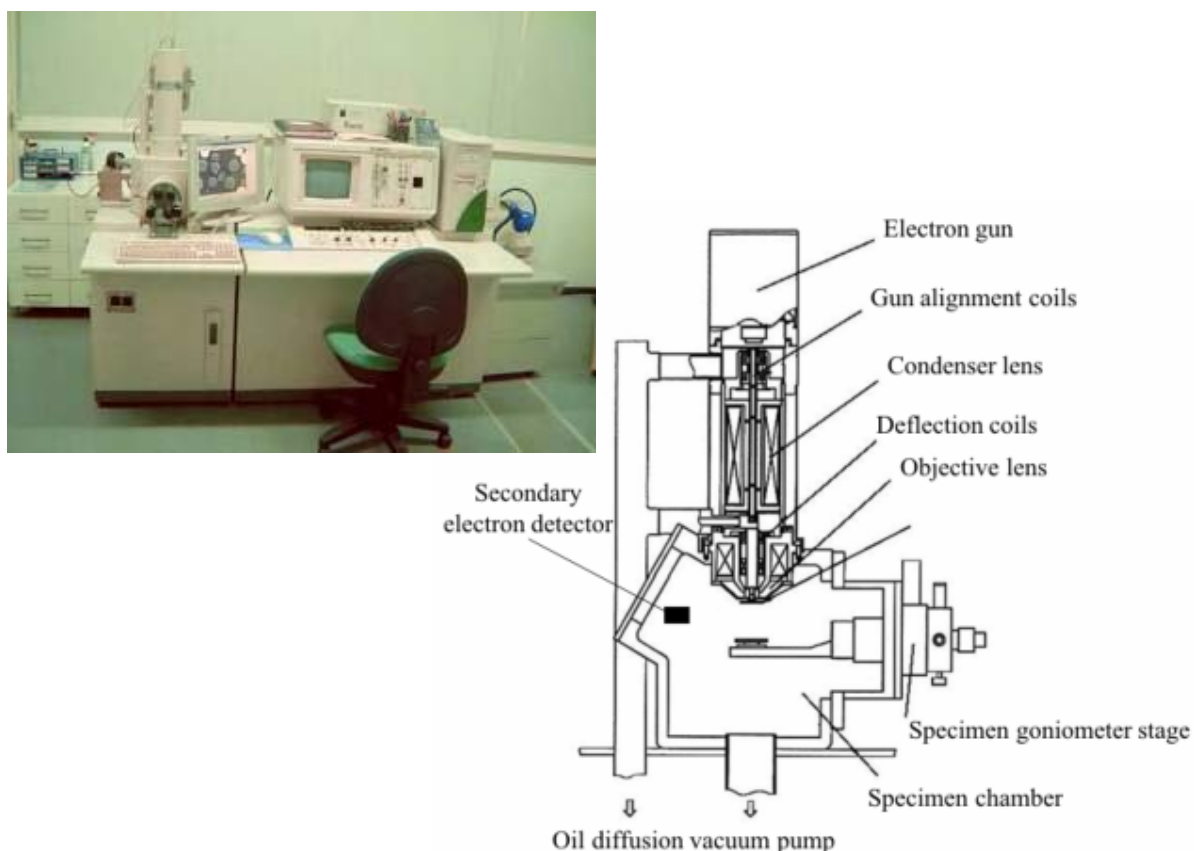Secondary electrons (SE) are defined as electrons emitted from the specimen with energy less than 50 eV, and are generally produced as a result of interactions between energetic primary electrons and weakly bound conduction electrons in the sample. An important characteristic of secondary electrons is their shallow sampling depth (see Figure 7), a direct consequence of the low kinetic energy with which they are formed [50]. SE are detected by an Everhart-Thornley detector which is a type of scintillator-photomultiplier device and the resulting signal is rendered into a two-dimensional intensity distribution that can be viewed and saved as a digital image. The brightness of the SE signal depends on the number of electrons reaching the detector. If the beam enters the sample perpendicularly to the surface, then the activated region is uniform about the axis of the beam and a certain number of secondary electrons "escape" from within the sample. As the angle of incidence increases, the "escape" distance of one side of the beam will decrease, and more secondary electrons will be emitted. Thus steep surfaces and edges tend to be brighter than flat surfaces, and this results in topographical images with well-defined, three-dimensional appearance. The SE signal allows spatial resolutions of less than 1 nm (see Figure 7).

Backscattered electrons (BSE) are high energy electrons and can escape from a much larger volume than SE (see Figure 7). The signal intensity will depend on the average atomic number of the specimen but is almost independent of the incident beam energy. BSE images have lower spatial resolution than SE images due to their larger volume of origin (see Figure 7), but can show contrast between areas with different chemical composition, since the signal intensity increases with the average atomic number in the sample. The average energy of the backscattered electrons is less than that of the primary incident electrons, but nevertheless of the same order of magnitude. The number of BSE leaving the sample surface upward might be significantly lower than those that follow trajectories toward the sides. Additionally, in contrast with the case of secondary electrons, the collection efficiency of backscattered electrons cannot be significantly improved by a positive bias (common on Everhart-Thornley detectors) due to their high kinetic energy. As a result, a detector positioned on one side of the sample has low detection efficiency for BSE due to the small collection angle. The use of a dedicated backscattered electron detector above the sample in a "doughnut" type arrangement, with the electron beam passing through the hole of the doughnut, greatly increases the solid angle of collection and allows for the detection of more backscattered electrons.

2.2.2. Transmission electron microscopy

In transmission electron microscopy a beam of electrons, focused by multiple electromagnetic lenses and apertures, is transmitted through a specimen. This imaging technique is able of achieving resolutions of less than 0.1 nm. The lens system is designed to eliminate stray electrons as well as to control and focus the electron beam. Various techniques can be used to collect data from the electrons that have passed through the sample: either by means of a fluorescent screen that is hit by the electron beam or, alternatively, the resulting image may be recorded on photographic film or with a CCD camera linked to a computer.

A transmission electron microscope consists of two or three condenser lenses that focus the electron beam on the sample; an objective lens to form the diffraction pattern in the back focal plane and the image of the sample in the image plane; and some intermediate and projection lenses to magnify the image or the diffraction pattern on the screen, film or CCD. The optical system of a TEM is shown in Figure 8.
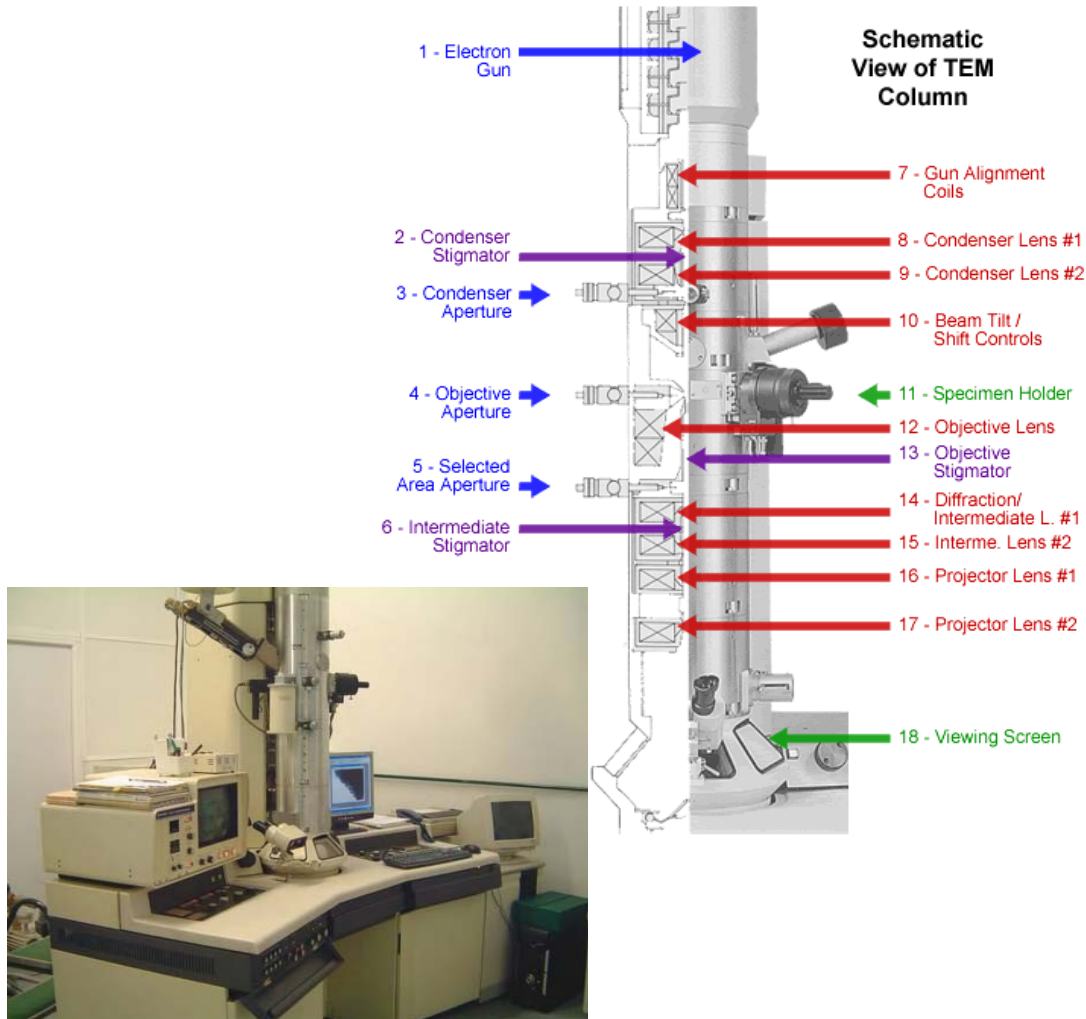
Figure 8 – Image and diagram of a transmission electron microscope.

The objective lens generates simultaneously the diffraction pattern and the first intermediate image. Figure 9 shows that the ray paths are identical until the intermediate lens, where the field strength is changed, depending on the desired operation mode. Higher field strength (shorter focal length) is used for imaging, whereas weaker field strength (longer focal length) is used for diffraction.
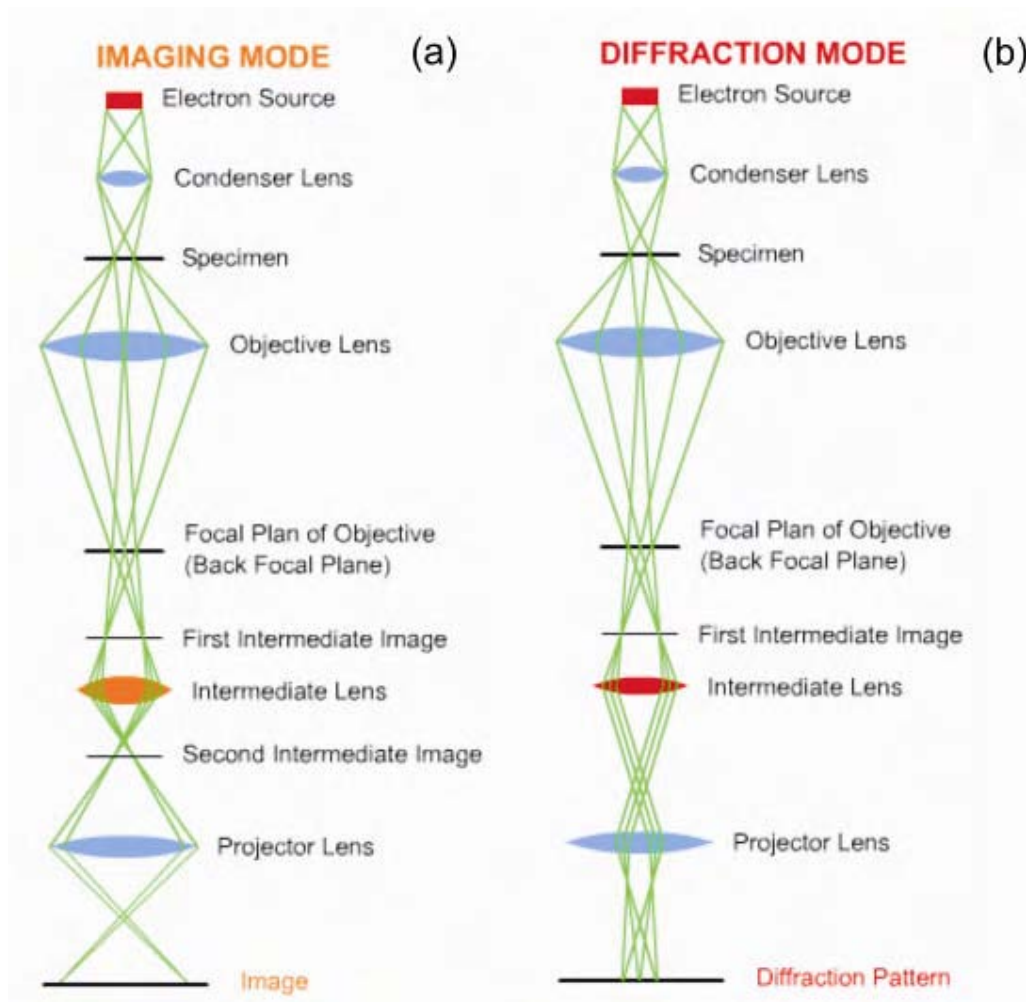
Figure 9 – Optical system of TEM: (a) imaging mode and (b) diffraction mode.

A crystalline material interacts with the electron beam mostly by diffraction rather than absorption, although the intensity of the transmitted beam is still affected by the volume and density of the material through which it passes. The intensity of diffraction depends on the orientation of the planes of atoms in a crystal relative to the electron beam; at certain angles the electron beam is strongly diffracted, while at other angles the beam is largely transmitted. The microscope is often equipped with a specimen holder that allows the user to tilt the specimen to a range of angles in order to obtain specific diffraction conditions. Apertures placed below the specimen allow the user to select electrons diffracted in a particular direction in order to form images with particular contrast.

The bright-field mode (BF) (Figure 10) is commonly used to obtain contrasted images in most observations. Under this mode, an objective aperture is inserted into the back focal plane of the objective lens, the same plane at which the diffraction pattern is formed, just below the sample. The aperture only allows transmitted electrons to contribute for the bright-field image, where intensively diffracting regions present hence dark contrast. Off-axis dark-field images are obtained by positioning the objective aperture around a specific diffracted beam, so that only this beam is allowed to form the image (Figure 11 (a)). In this case, the intensively diffracting regions appear bright in a dark background. In order to minimize lens aberrations under dark-field, the incident beam is usually deflected along the optic axis, so that the diffracted beam is aligned along the optical axis of the instrument resulting in on-Axis dark-field imaging (Figure 11 (b)).
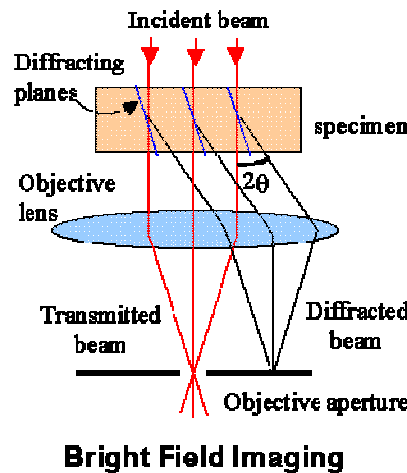
Figure 10 – Bright-field mode of imaging.
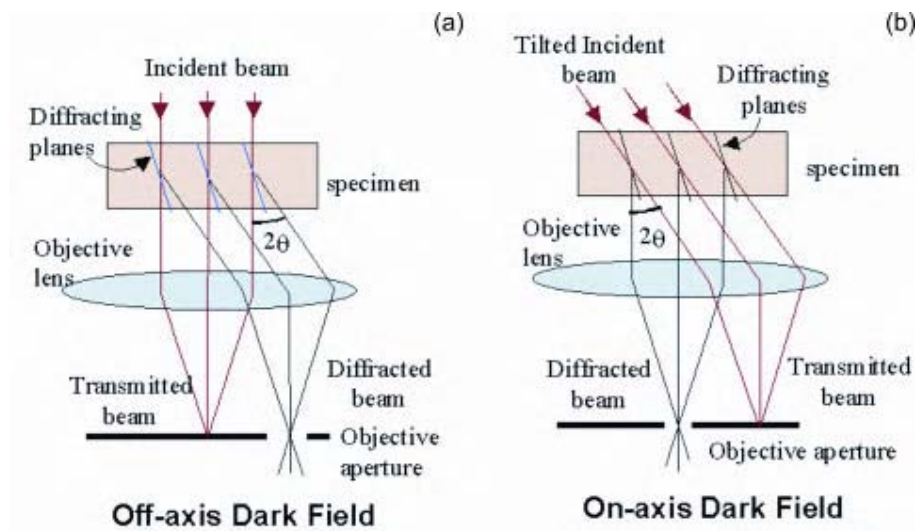
Figure 11 – (a) Off-axis dark field mode (higher aberrations) and (b) On-axis dark field mode (minimization of lens aberrations).

A selected area diaphragm can be used to collect diffracted electrons from a defined region of the imaged sample, for example, a particle or a precipitate. This diffraction mode is called selected area diffraction (SAD). Alternatively, diffraction patterns can be obtained by focusing the electron beam with the condenser lenses to obtain a small spot size on the object (2-10 nm). Under this diffraction mode, called microdiffraction, diffraction spots become disks whose radii depend on the condenser diaphragm size (Figure 12). SAD and microdiffraction patterns enable to determine the symmetry of crystalline lattices and therefore to identify specific phases in the microstructure.
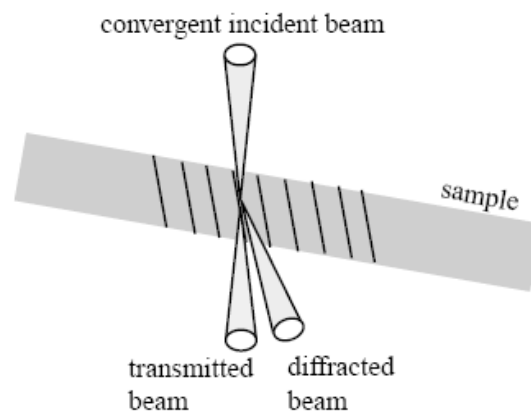
Figure 12 – Microdiffraction mode.

2.2.3. Lorentz microscopy

The name Lorentz microscopy has been given to the mode of transmission electron microscopy where the contrast mechanism is based on the Lorentz defection imposed on electrons by the passage through a magnetic specimen. This requires the specimen not to be immersed in the objective magnetic field; hence this lens is usually switched off and the magnetic domains are imaged by the intermediate lens (see Figure 8).

When the electrons pass through adjacent magnetic domains in the sample, they tend to be deflected in opposite directions by Lorentz forces:

$$\mathbf{F} = |e| \, (\mathbf{v} . \, \boldsymbol{B}) \tag{2}$$

where e and v are the charge and velocity of the electrons, and B is the magnetic induction in the specimen. Only components of the magnetic induction normal to the electron beam give rise to deflection, nevertheless, stray fields above and bellow the specimen also contribute to the image. The deflection direction depends on the magnetisation direction within the domain being imaged and is perpendicular to it.

Figure 13 shows ray diagrams indicating the way in which the electrons are deflected for a specimen containing two sets of domains magnetised in-plane and separated by 180° domain walls: the Lorentz deflections result in each spot in the electron diffraction pattern being split in two. There are then two methods by which the magnetic domain structure can be imaged: the Foucault mode and the Fresnel mode.

To image magnetic domains using the Foucault mode, the intermediate lens is kept in-focus but one of the split spots in the diffraction pattern is blocked by displacing an aperture. Contrast then results only from the domains contributing to the electrons deflected through the aperture. By knowing the relative position of the aperture and image, the direction of magnetisation within the various domains can be determined

For the Fresnel imaging mode the intermediate lens is defocused so that out-of-focus images of the specimen are formed. Under these conditions the magnetic domain walls are imaged as alternate bright (convergent) and dark (divergent) lines. For the overfocused image, bright lines occur at the position of domain walls for which the magnetisation on either side is deflecting the electrons towards the wall (A in Figure 13), whereas dark lines are observed at the walls for which the magnetisation on either side is deflecting the electrons away from the wall (B in Figure 13). The opposite contrast is observed at the underfocused image. If a coherent electron source is used, the convergent wall images consist of sets of electron diffraction fringes running parallel to the wall.
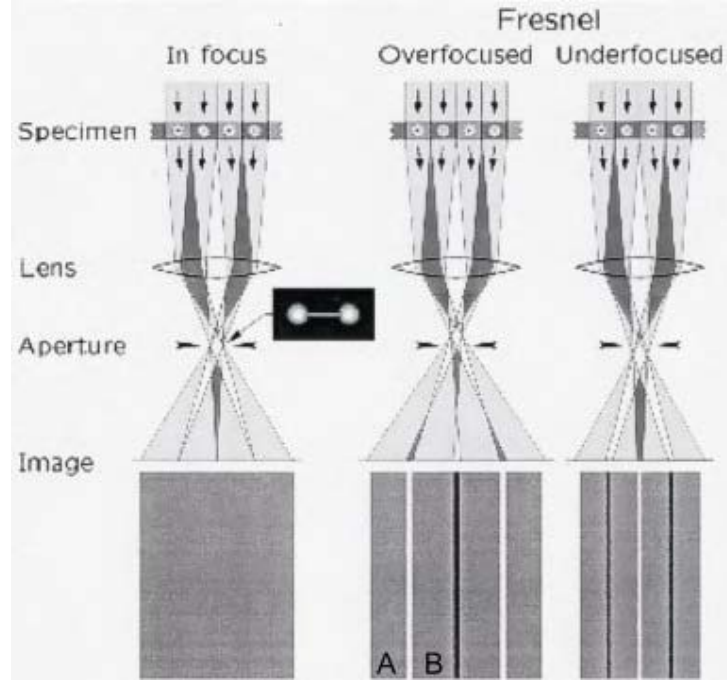
Figure 13 – Ray diagrams showing the in focus image, the overfocused and the underfocused image for a foil with 180° domains in which the magnetization is parallel to the plane of the foil and the domain wall, and in opposite directions in alternate domains. On passing through the magnetic induction in the specimen, the electrons are deflected by Lorentz forces into opposite directions in adjacent domains, leading to an excess of electrons due to overlap at A and deficiency of electrons at B.

In the absence of potential variation in the area of interest, the 2-D phase gradient of the exit wave function $(\nabla_\perp \phi)$ can be considered to be proportional to the in-plane magnetization components $B(\mathbf{r}_\perp)$, multiplied by the local thickness (t) of the foil [51]:

$$\nabla_\perp \phi(\mathbf{r}_\perp) = \frac{q}{h}[B(\mathbf{r}_\perp) \times \mathbf{e}_z]t(\mathbf{r}_\perp) \tag{3}$$

where $\mathbf{r}_\perp$ is the position within the image plane normal to the optical axis, q is the electron charge and h is the Planck constant.

Quantitative induction information can be obtained from Fresnel images using the phase reconstruction method proposed by Paganin and Nugent [52] that requires a through-focus series of three images: a set of equally under and overfocused Fresnel images and the in-focus image. The algorithm first aligns all three images with respect to a common origin, and then subtracts the overfocused image from the underfocused one to obtain the derivative of intensity (I) along the beam direction:

$$\frac{I\left(\mathbf{r}_{\perp},\Delta f\right)-I\left(\mathbf{r}_{\perp},-\Delta f\right)}{2\Delta f} \approx \left(\frac{\partial I\left(\mathbf{r}_{\perp},z\right)}{\partial z}\right)_{z=0} \tag{4}$$

where z denotes the coordinates along the optical axis and Δf is the equal defocus magnitude. From this derivative the algorithm reconstructs the phase, considering the Transport-of-Intensity Equation [53]:

$$\nabla_{\perp}.\left(I\left(\mathbf{r}_{\perp},z\right)\nabla_{\perp}\phi\right)=-\frac{2\pi}{\lambda}\frac{\partial I\left(\mathbf{r}_{\perp},z\right)}{\partial z} \tag{5}$$

which is valid in the limit of vanishing defocus and relates the intensity change of the electron wave along the optical axis to the intensity and phase of the wave in a plane normal to the axis. The proposed formal solution to this second order differential equation is [51]:

$$\phi\left(\mathbf{r}_{\perp},0\right)=-\frac{2\pi}{\lambda}\nabla_{\perp}^{-2}\left\{\nabla_{\perp}.\left[\frac{1}{I\left(\mathbf{r}_{\perp},0\right)}\nabla_{\perp}\left(\nabla_{\perp}^{-2}\frac{\partial I\left(\mathbf{r}_{\perp},0\right)}{\partial z}\right)\right]\right\} \tag{6}$$

where ∇^{-2} is the inverse Laplace operator. This equation can be numerically solved by a Fast Fourier Transform method using symmetric extensions of the original image to obtain periodic continuation in reciprocal space [54]. The 2-D phase reconstruction obtained with eq. (6) can then be used to derive induction variations according to eq. (3) by assuming invariant potential and constant thickness across the area of interest.

2.2.4. Energy dispersive X-ray spectroscopy

Energy dispersive x-ray spectroscopy (EDS) is an analytical technique that uses x-rays emitted from the specimen when bombarded by energetic electrons to identify its elemental composition. The convenience of EDS spectrometers association with electron microscopes is widely acknowledged: these instruments are intrinsically equipped with a cathode and magnetic lenses to create and focus a beam of high-energy electrons. An EDS spectrum is constituted by a continuous background and peaks characteristic of the elements present in the material. The x-ray generative principle is described in 2.1.

The energy dispersive x-ray spectrometer setup comprehends the following components: beam source, x-ray detector, pulse processor and analyzer (Figure 14). The detector is used to convert x-ray energy into voltage signals, and measures the number of emitted x-rays versus their energy; this information is sent to a pulse processor, which measures the signal and passes it onto an analyzer for data display and analysis.
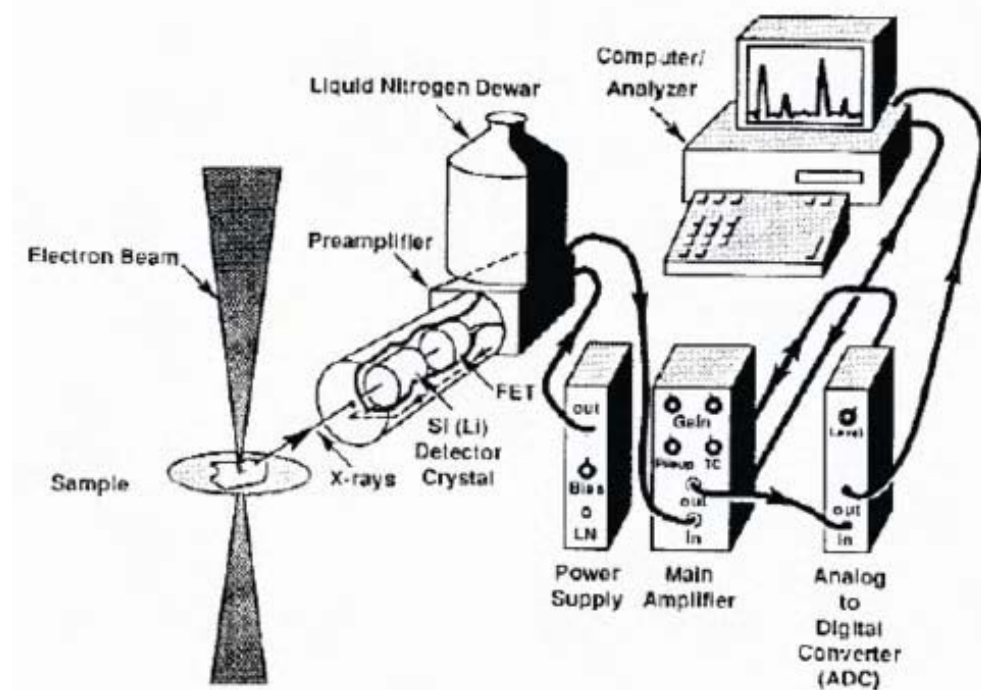
Figure 14 – Scheme of an energy dispersive X-ray spectrometer in a TEM microscope.

The analysis of EDS spectra is based on the link between the elemental fractions present in the sample and the generated intensity of the characteristics peaks. It requires therefore background removal and peak deconvolution before determination of integrated intensities. In standardless quantitative analysis, the dependence of the ionization cross section on the atomic number is theoretically considered, as well as matrix effects, such as absorption and fluorescence. Alternatively, standards with composition similar to the specimen can be used for comparative analysis and in this case the results are considered quantitative. In the present study no standards were available. Furthermore, standardless quantification has also not been carried out due to the fact that the matrix corrections implemented in the chemical analysis commercial software did not yield reliable elemental proportions.

2.3. Scanning probe microscopy

Scanning probe microscopy (SPM) is a branch of microscopy that forms images of surfaces using a physical probe to scan the specimen. An image of the surface is obtained by mechanically moving the probe in a raster scan over the specimen, line by line, and recording the probe-surface interaction as a function of position. Atomic force microscopy and magnetic force microscopy are established types of scanning probe microscopy as briefly described bellow.

2.3.1. Atomic force microscopy

The atomic force microscope is a high-resolution type of scanning probe microscope based on a microscale cantilever with a sharp tip (probe) at its end, which is used to scan the specimen surface. When the tip is brought into proximity of a sample surface, forces between the tip and the sample lead to a deflection of the cantilever according to Hooke's law. The extension produced is directly proportional to the load:

$$\vec{F} = -k\,\vec{x}$$

(7)

where x is displacement from the equilibrium position, F is the restoring force exerted by the material, and k is the force constant or spring constant. If the tip were scanned at a constant height, there would be a risk that it would collide with the surface, causing damage. Hence, in most cases a feedback mechanism is employed to adjust the tip-to-sample distance and maintain a constant force between the tip and the sample. Usually, the sample is mounted on a piezoelectric that can move the sample in the z direction to maintain the force constant, while the x and y directions are used for scanning the sample. Alternatively a 'tripod' configuration of three piezo crystals may be employed, with each responsible for scanning in the x, y and z directions. Typically, the deflection is measured using a laser beam reflected from the top of the cantilever into an array of photodiodes. A topographic map of a sample surface is obtained, for instance, by keeping the force constant while scanning the sample relative to the tip. The microscope can be operated under contact mode, tapping mode, or non-contact mode (where Van der Waals' forces are probed).

2.3.2. Magnetic force microscopy

For magnetic tip and sample, the spatial variation of the magnetic force interaction between them can be probed using force microscopy. If the tip scans the sample surface within a distance of typically 10 – 500 nm, magnetic interaction of the tip with the stray field emanating from the sample is noticeable, while Van der Waals' forces vanish. The magnetic interaction strength determines the amount of cantilever deflection, which can be monitored. The long-range magnetic dipole interaction is usually probed using an alternate current detection method that is sensitive to force gradients. Therefore, force gradients rather than magnetic dipole forces are usually measured. Due to the small size of the magnetic cantilever it is possible to consider it as a point magnetic dipole. In this approximation the force acting on the cantilever can be written in the form of:

$$F = (m \cdot \nabla)H \tag{8}$$

where m is the magnetic moment of the cantilever, and H is magnetic stray field emanating from the sample[55].

Magnetic force microscopy uses a two-pass technique to detect magnetic forces gradients. In the first scan an AFM topography image is produced with a magnetic tip under tapping mode. In a second scan the cantilever is lifted (non-contact mode) to a selected height and follows the stored topography without feedback (lift mode). During the second scan, as Van der Waals' forces vanish, tip-sample interactions are caused solely by magnetic effects and the resonance oscillations can be used to measure the derivative of the force in the direction normal to the sample surface acting on the magnetic cantilever. The phase shift ($\Delta\phi$), amplitude shift (ΔA), and the resonant frequency shift ($\Delta\omega_0$) are directly related to the local force derivative [56].

$$\Delta\phi = \frac{Q}{k}\frac{\partial F}{\partial z} \tag{9}$$

$$\Delta A = \frac{2A_0 Q}{3\sqrt{3}}\frac{\partial F}{\partial z} \tag{10}$$

$$\Delta\omega_0 = \frac{1}{2k}\frac{\partial F}{\partial z}\omega_0 \tag{11}$$

the Q is the vibrating system quality factor, k its spring constant, and A_0 is the amplitude of the cantilever oscillation at resonant frequency ω_o in absence of external force gradient. In practice, however, $\partial F / \partial z$ is usually determined by measuring the cantilever phase variation due to the higher spatial resolution of this signal.

2.4. Magnetization isotherm cycles

Magnetization curves can be measured using multi-measurement platforms that allow different automated measurements to be made by a series of dedicated probes, like for example the AC/DC susceptibility probe (see Figure 15). A common feature to all the probes is the possibility of performing measurements in a wide temperature range (4.2 to 400 K) and under DC fields up to 12 T, which are generated by a superconducting solenoid. Moving a sample with magnetic moment through a coil induces a voltage in that coil which is proportional both to the moment and to the speed of movement.

The DC probe consists of an extraction magnetometer having a sensitivity of 12 Tesla, which utilizes the same coil system as the AC probe. In DC magnetization measurements, a sample is magnetized by a static DC field arising from the superconducting magnet. Inductive measurements are performed by moving the sample relative to a set of pickup coils. The output signal from the detection coil can be measured and related to the material magnetic properties.

Figure 15 - *MagLab* 2000 system (Oxford Instruments) with magnetic fields up to 12 T.

3. Y-Fe-Ti system (Y:11Fe:Ti alloy)

3.1. Introduction

Among the iron-based $ThMn_{12}$-type systems, the $RFe_{11}Ti$ series has been extensively investigated [5,8,11-26]. In these fundamental studies, the compounds with the non-magnetic rare-earths Y and Lu have been used to establish the magnetization, exchange and anisotropy of the iron sublattice. $YFe_{11}Ti$ and $LuFe_{11}Ti$ are ferromagnetic, exhibit uniaxial magnetic anisotropy, that results from the Fe sub-lattice, with *c* as the easy magnetization axis. These characteristics have been subsequently used to deduce the R-Fe exchange for the rest of the compounds [8]; propose crystal-field models for the anisotropy of the 4f sublattice [8,15-18]; assess the nature of field-induced magnetic phase transitions [8,10]; and analyze thermal expansion anomalies [15,18], magnetic resistivity [22] and spontaneous magnetostriction [15] in the series. In spite of the vast fundamental work carried out on the magnetic behavior of $RFe_{11}Ti$ compounds only limited studies have been reported on magnetic domain configurations [39-41] and scarce microstructural characterization has been performed on these materials [36-38].

3.2. Experimental details

Alloy preparation and heat treatment

The alloys were prepared by melting the elements with ≥99.9 % purity in an arc furnace, under argon atmosphere and on a water-cooled crucible. In order to increase homogeneity, the samples were melted at least three times (as-cast condition). The weighted elemental quantities corresponding to the $YFe_{11}Ti$ stoichiometry were 1.8172 mg for iron, 0.2629 mg for yttrium and 0.1420 mg for titanium, with a mass loss after fusion of ~1 %.

Part of the as-cast material was subsequently sealed in evacuated quartz tubes and annealed at 950 °C for 1536 h (cast/annealed condition). Another portion of the as-cast material was remolten and splat-quenched by cooling down a droplet of the prepared alloy between two copper pistons shot against each other at ~9 ms^{-1}. A cooling rate of ~10^6 Ks^{-1} is obtained by this method and the resulting disks have a diameter of ~20 mm

and a thickness of ~100 μm (splat condition). A fraction of the splat-quenched material was subsequently sealed in evacuated quartz tubes and annealed at 800 °C for 2208 h (splat/annealed condition).

X-ray powder diffractograms

X-ray powder diffractograms of the materials have been obtained at room temperature using a Panalytical X'Pert Pro powder diffractometer. Samples were crushed down to a fine powder and deposited onto a low noise (single crystalline Si) sample holder. The data acquisition was made with a 2θ - step size of 0.03°. The software package PowderCell [57] was used to simulate diffractograms for comparison with experimental data. An YFe$_{11}$Ti unit cell with ThMn$_{12}$-type of structure was built based on the crystallographic information listed in [58] by assuming that 75% of the 8i positions were occupied by Fe and 25% by Ti, and using the lattice parameters reported in [20].

A cell of the Th$_2$Zn$_{17}$ type was built based on the crystallographic information and lattice parameters reported in [59] and, for simplicity, by assuming an Y$_2$Fe$_{17}$ stoichiometry. A cell of the Th$_2$Ni$_{17}$ type was built also assuming an Y$_2$Fe$_{17}$ stoichiometry and using the crystallographic information listed in [60] and lattice parameters derived from the relations between the Th$_2$Ni$_{17}$ and ThMn$_{12}$ structures [12] with base on YFe$_{11}$Ti values [20]. A cell for a Y$_3$(Fe,Ti)$_{29}$ phase with a Nd$_3$(Fe,Ti)$_{29}$-type structure has also been built considering the *A*2/*m* space group with base on the crystallographic information listed in [61] and using the lattice parameters presented in [62].

SEM

Sample preparation for scanning electron microscopy involved grinding with silicon carbide paper and consecutive polishing with 6, 3 and 1 μm diamond suspensions. A final polishing and light etching were obtained with a commercial alumina suspension in an acid solution (OPS-Struers). The observations have been performed with a Hitachi S2400 instrument equipped for EDS after further etching with acqua regia or with an aqueous solution of HF, HCl and HNO$_3$.

AFM and MFM

Sample preparation for atomic and magnetic force microscopy involved the metallographic steps described for SEM plus final polishing with a 0.1 μm diamond suspension. In some instances, light etching enabled to establish a clear correspondence between microstructure and magnetic configuration without critically impairing examination in lift mode. The observations have been performed with a Veeco di CP-II atomic force microscope using commercially available MFM cantilevers (MESP-CPMT) with nominal length of 225 μm and nominal spring constant of 2.8 N/m. The MESP-CPMT tips are coated by a CoCr alloy and have a nominal curvature radius of 25 nm. The tips are magnetized along their axis and have a coercivity of ~400 Oe. In lift mode the tip-sample separation (Z) was kept around 60 nm. MFM observations have been carried out under dynamic conditions using the sequential two-scan method.

TEM/Lorentz Microscopy

Sample preparation for transmission electron microscopy involved cutting discs with a diameter of 3 mm and grinding until a thickness around 80 μm was reached. The samples have been thinned to electron transparency by argon ion milling on a Gatan-Duo Mill machine, operating at an accelerated voltage of 4 kV, with a 14° incidence angle. TEM observations have been performed at 200 kV with a JEOL 2010F microscope and a Hitachi H8100 microscope, both equipped for energy dispersive X-ray spectroscopy. Magnetic domain observations by Lorentz microscopy have been performed using the JEOL 2010F instrument with the objective lens switched off, using the intermediate lens as image forming lens. A 2-D phase reconstruction has been carried out with eq. (6) from a set of Fresnel images and has been used to derive induction variations according to eq. (3).

Magnetization isotherm cycles

Magnetization isotherm cycles at room temperature were performed using a multipurpose characterization system *MagLab* 2000 (Oxford Instruments) with magnetic fields up to 5 T. Crushed powder particles of the splat-quenched and splat/annealed materials were fixed under random orientation with acetone soluble glue, which prevented rotation of individual particles under the applied magnetic field.

3.3. Results

X- Ray Diffraction

Figure 16 presents experimental X-ray diffractograms of the Y:11Fe:Ti alloy obtained for the as-cast, splat-quenched and annealed conditions, along with simulations for the $ThMn_{12}$ structure and other structures closely related to $ThMn_{12}$. The results indicate that both the as-cast and splat-quenched materials crystallized adopting essentially the $ThMn_{12}$-type structure. However, the presence of α-Fe(Ti) peaks at ~44.7° shows that the $YFe_{11}Ti$ stoichiometry is not strictly followed. For this reason the $ThMn_{12}$-type phase will be hereafter denominated $YFe_{11-x}Ti_y$, where x and y are variables that depend on the material condition. The α-Fe(Ti) peak intensity remained approximately constant for the as-cast condition after annealing at 950 °C, whereas for the splat condition annealing at 800 °C induced a conspicuous increase of the α-Fe(Ti) proportion. The peaks at 40.9° and 45.3° indicate the presence of Fe_2Ti. The lattice parameters of the tetragonal $YFe_{11-x}Ti_y$ phase in all the studied conditions (see legends in Figure 16) are in fair agreement with the ones reported for $YFe_{11}Ti$ [10,18,20]. The α-Fe(Ti) lattice parameter was $a_{cast} = 0.\,287$ nm for the as-cast condition and $a_{splat} = 0.288$ nm for the splat condition, the annealing treatments induced lattice parameter variations of, respectively, $(a_{cast/annealed} - a_{cast})/a_{cast} = $ -0.1 % and $(a_{splat/annealed} - a_{splat})/a_{splat} = $ -0.3 %.
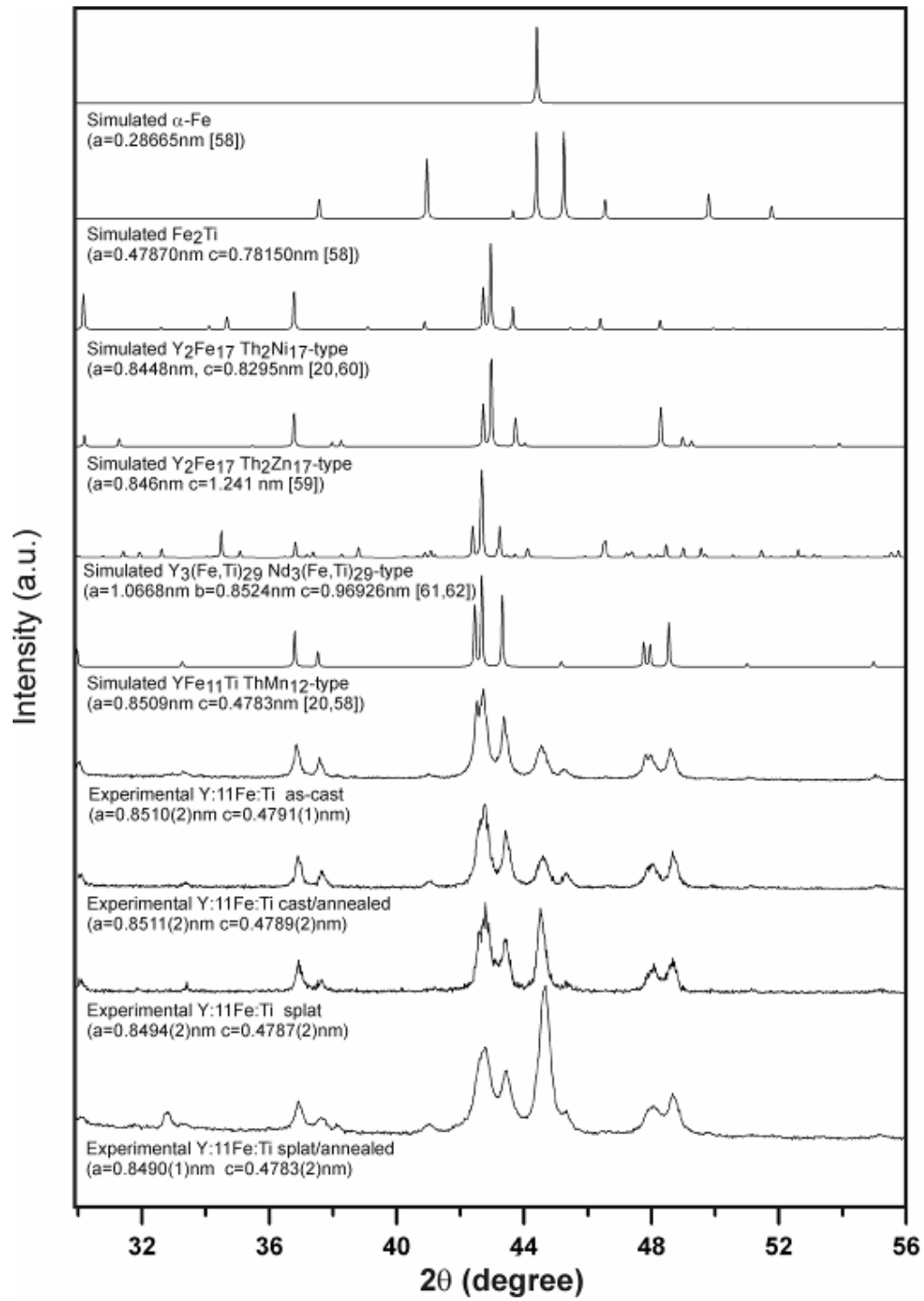
Figure 16 – Experimental X-ray diffractograms for the Y:11Fe:Ti alloy under as-cast, cast/annealed, splat and splat/annealed conditions (simulations for α-Fe, Fe_2Ti, Y_2Fe_{17} (Th_2Zn_{17} and Th_2Ni_{17}-types), $Y_3(Fe,Ti)_{29}$ ($Nd_3(Fe,Ti)_{29}$-type) and $YFe_{11}Ti$ ($ThMn_{12}$-type) are included. Lattice parameters, determined assuming a stoichiometric $YFe_{11}Ti$ structure, are indicated above each experimental diffractogram.

As-cast and cast/annealed microstructures

Figure 17 presents images of typical microstructures of the as-cast and cast/annealed materials obtained by SEM and the corresponding EDS maps. As expected from the XRD results, the predominant phase in the as-cast microstructure is the tetragonal $YFe_{11-x}Ti_y$ compound, which exhibits twins (indicated by arrows in Figure 17 (a)) and displays a faceted cellular configuration with intercellular distances typically in the 20-30 μm range. EDS point analysis showed a considerable presence of α-Fe(Ti) and a minor presence of Fe_2Ti at the intercellular regions, forming a fine eutectic mixture. Y was found only at the $YFe_{11-x}Ti_y$ cells (see Figure 17 (c)). The microstructure of the cast/annealed condition (Figure 17 (d)) evidences coarsening of the eutectic phases and a significant increase in the Fe_2Ti volume fraction (compare Figure 17 (c) and (f)), justifying the better definition of the XRD peaks at 40.9° and 45.3° in Figure 16. The scale and morphology of the $ThMn_{12}$-type phase showed moderate evolution with the long annealing treatment (1536 h at 950 °C). This behaviour may be related to the presence of eutectic phases around the faceted cells that due to a reduced Y solubility act as a barrier that contributes to delay $YFe_{11-x}Ti_y$ coalescence.
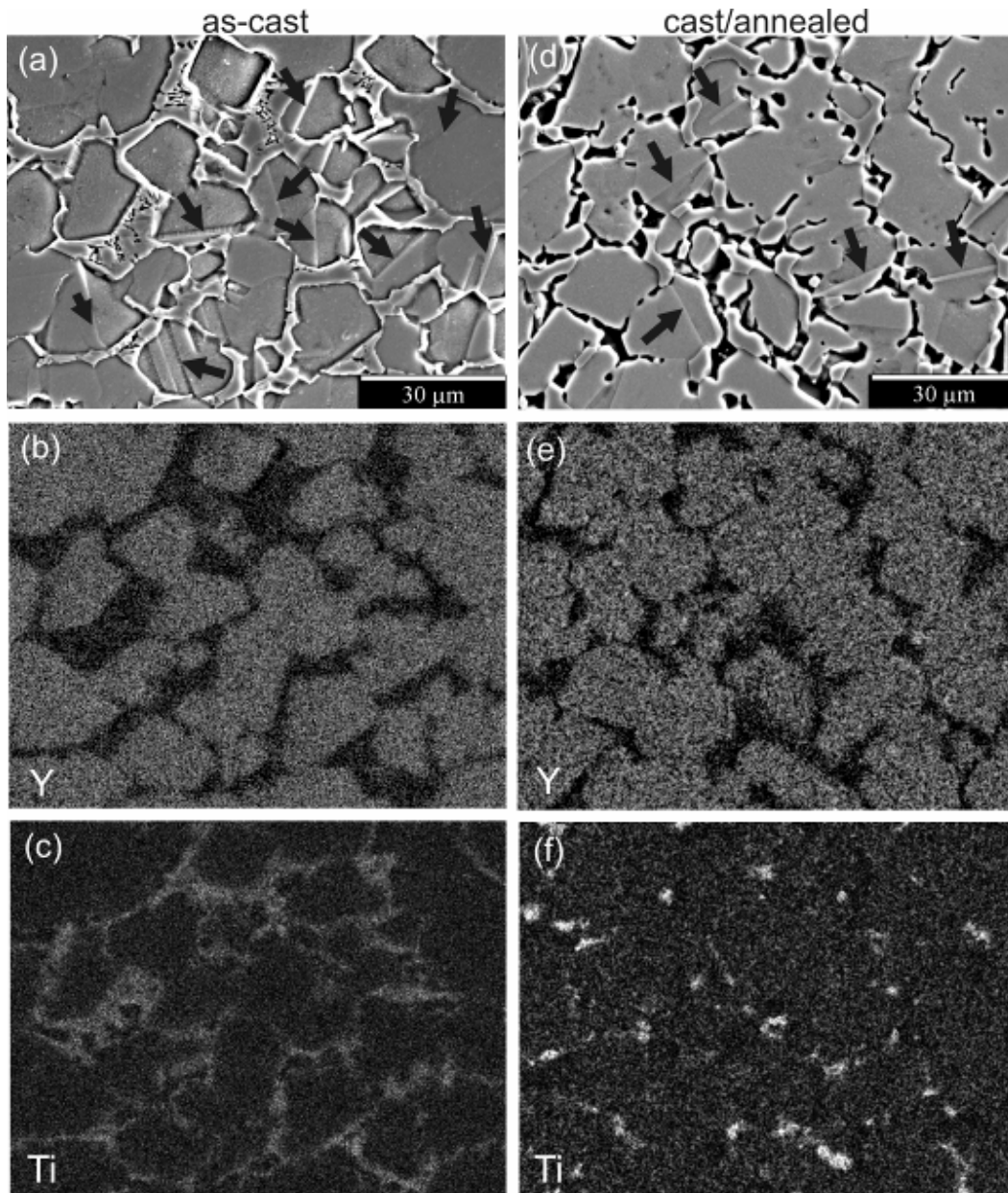
Figure 17 – Secondary electron images and X-ray maps of the etched Y:11Fe:Ti alloy. As-cast microstructure (a) and corresponding X-ray maps for Y (b) and Ti (c) showing $YFe_{11-x}Ti_y$ faceted cells with twins (arrows). EDS point analyses demonstrated that the intercellular regions consist of an eutectic mixture of α–Fe(Ti) and Fe_2Ti (minor phase). Cast/annealed microstructure (d) and corresponding X-ray maps for Y (e) and Ti (f), showing similar faceted cells, coarsened eutectic phases and a higher presence of Fe_2Ti (etched phase and bright regions in (f)).

Figure 18 shows MFM images of the cast/annealed material. The $YFe_{11-x}Ti_y$ grains exhibit domains with mixed stripe/maze patterns characteristic of bulk materials with uniaxial anisotropy and *c*-axes at an angle to the surface. The presence of small cone shaped reverse domains (reverse spikes with linear dimensions below 200 nm) and the jagged appearance of the stripe domains (see Figure 18 (b) and (c)) result from fine domain branching at the surface due to minimization of closure energy [63].
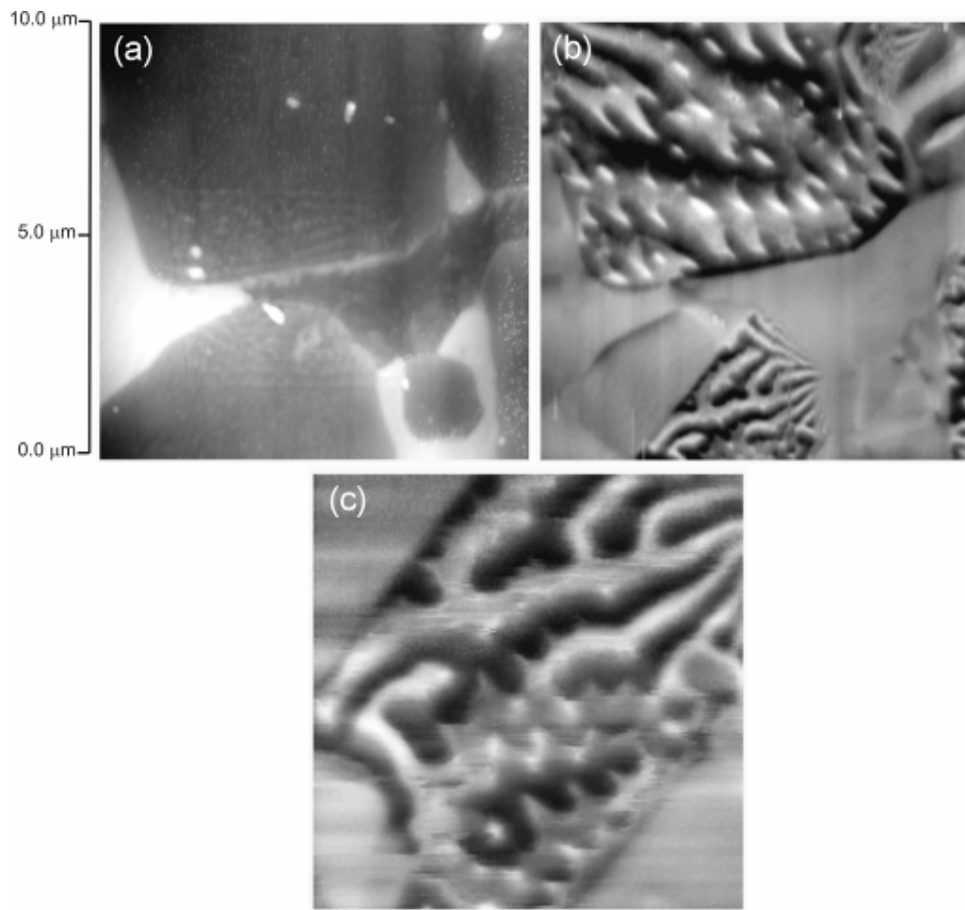

Figure 18 – MFM images of the Y:11Fe:Ti material surface under the cast/annealed condition (slightly etched). (a) Topographical image (tapping mode) where the bright elevated regions correspond to α-Fe(Ti), (b) phase image obtained under lift mode with a magnetized CoCr tip over the same area as (a) where the phase range is 58°. (c) Magnification of the bottom grain in (b) where the phase range is 18°.

Splat-quenched and splat/annealed microstructures

The bright-field image and the over and underfocused Fresnel images in Figure 19 present the typical microstructure and magnetic domain configuration of the splat-quenched Y:11Fe:Ti material under thin film form. EDS analyses showed a uniform distribution of α-Fe(Ti) and $YFe_{11-x}Ti_y$ crystallites while no Fe_2Ti could be detected. The grain size for both α-Fe(Ti) and $YFe_{11-x}Ti_y$ lies typically within 100 to 200 nm. A close inspection to the Fresnel images reveals that the magnetic contrast arises essentially at grain boundaries, indicating that the magnetic domains correspond roughly to individual crystallites. In a few instances, the magnetic domains included more than one grain and, in contrast, larger crystallites were able to contain internal domain walls (see arrows in Figure 19 (b) and (c)). Figure 20 presents typical MFM results obtained with the splat-quenched Y:11Fe:Ti material under the bulk form, where the microstructural scale shows that magnetic domains correspond essentially to individual crystallites.
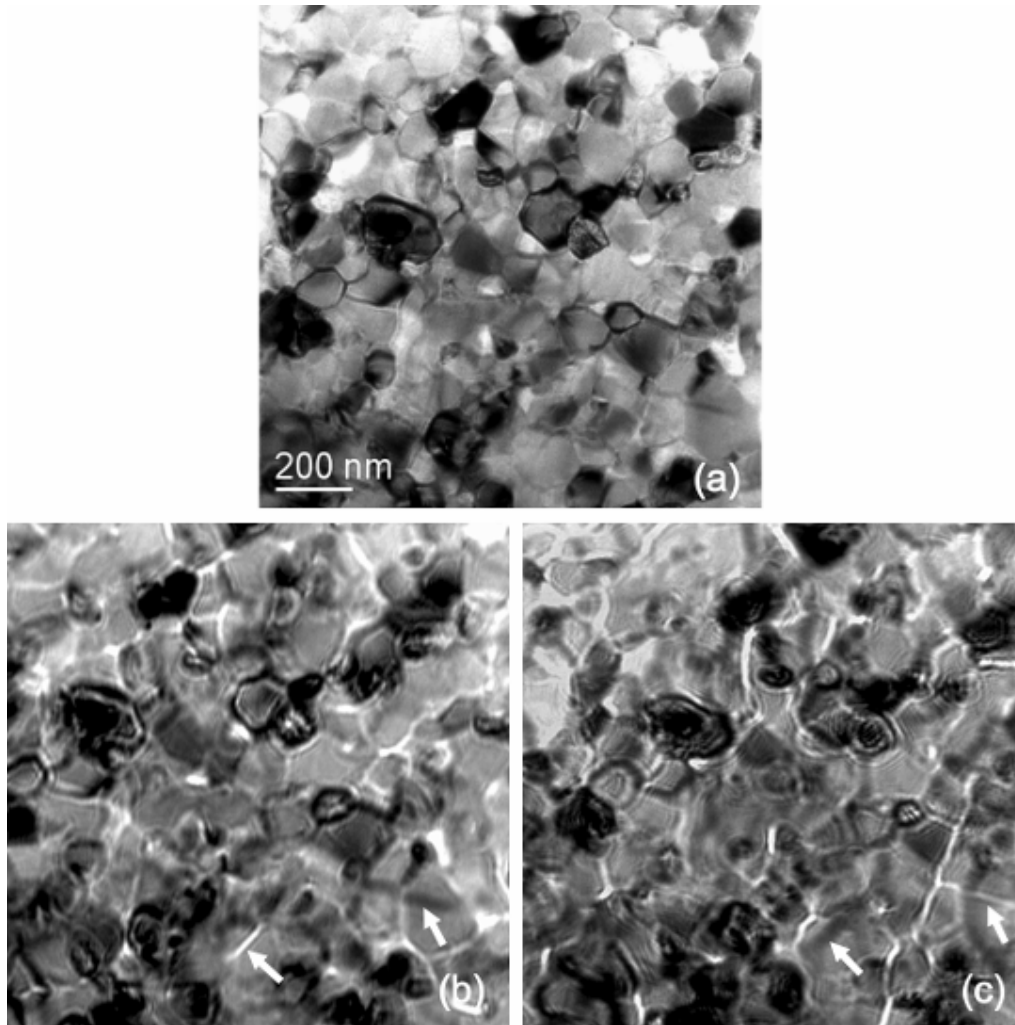
Figure 19 – Microstructure and underlying domain configuration of the splat-quenched Y:11Fe:Ti material: (a) in focus, (b) overfocused and (c) underfocused.
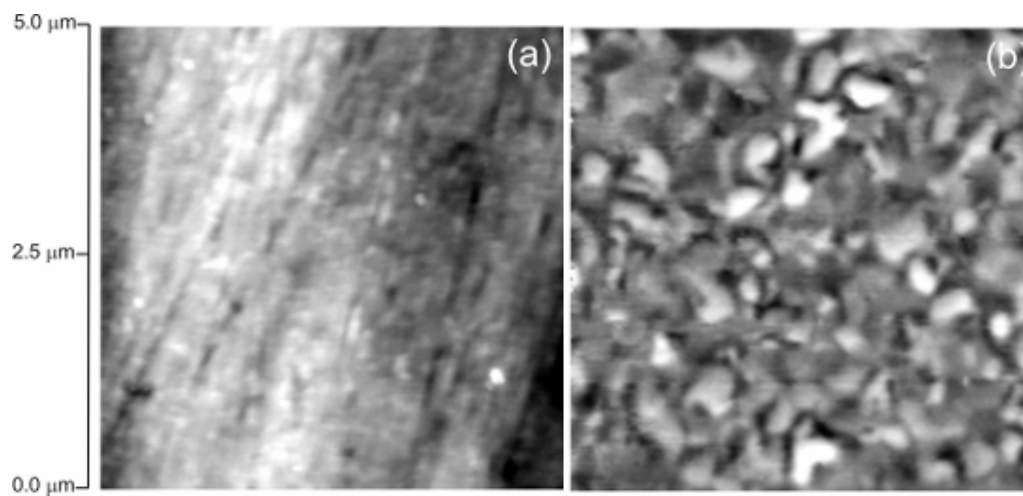

Figure 20 - MFM images of the Y:11Fe:Ti material surface under splat condition. (a) Topographical image (tapping mode) where the bright elevated region is foreign matter, (b) phase image obtained under lift mode with a magnetized CoCr tip over the same area as (a) where the phase range is 49°.

Figures 21 to 25 present the typical microstructure and magnetic domain configuration of the splat/annealed Y:11Fe:Ti material under thin film form, as well as chemical information. As compared to the splat condition, the annealed microstructure reveals an overall grain growth to sizes in the 200-800 nm range. In combination with the underlying microstructure, EDS point analyses revealed a more pronounced size increase for α-Fe(Ti) grains than for $YFe_{11-x}Ti_y$ ones. The convex surfaces of α-Fe(Ti) grains, such as A and B in Figure 21 (a), testify for an undergoing growth process that often resulted in abnormal growth. EDS analyses also showed that the annealing treatment induced a scattered presence of Fe_2Ti crystallites. Under the splat/annealed condition, grain boundaries continued to be largely associated with domain walls (see Figures 21 and 25). In addition, large grains presented internal magnetic structure: the few large $YFe_{11-x}Ti_y$ grains observed displayed internal domain walls following stripe/maze patterns characteristic of high anisotropy thin films with 50-100 nm domain width (see Figure 24 (a) and (b)), while vortex domains were common in large α-Fe(Ti) grains, such as A and B in Figure 21. A correlation between the position of vortex walls at the grain boundary and the arrangement of neighbouring grain is illustrated for A and B in Figure 21 (d). Due to the high number of interacting domains present in the microstructures and in order to optimize the magnetic contrast for visual inspection, Fresnel images have been obtained with relatively high and not equally under and overfocus values. Although these do not correspond to optimal conditions to solve eq. (5), a numerical solution to this equation (eq. (6)) has been used to reconstruct the phase of the exit wave function using the images presented in Figure 6 (a) to (c) and considering an averaged defocus ($|\Delta f|$) of 100 mm. In-plane induction components (multiplied by t) were subsequently calculated by a 2-D gradient operation and the resulting map is shown in Figure 6 (e).
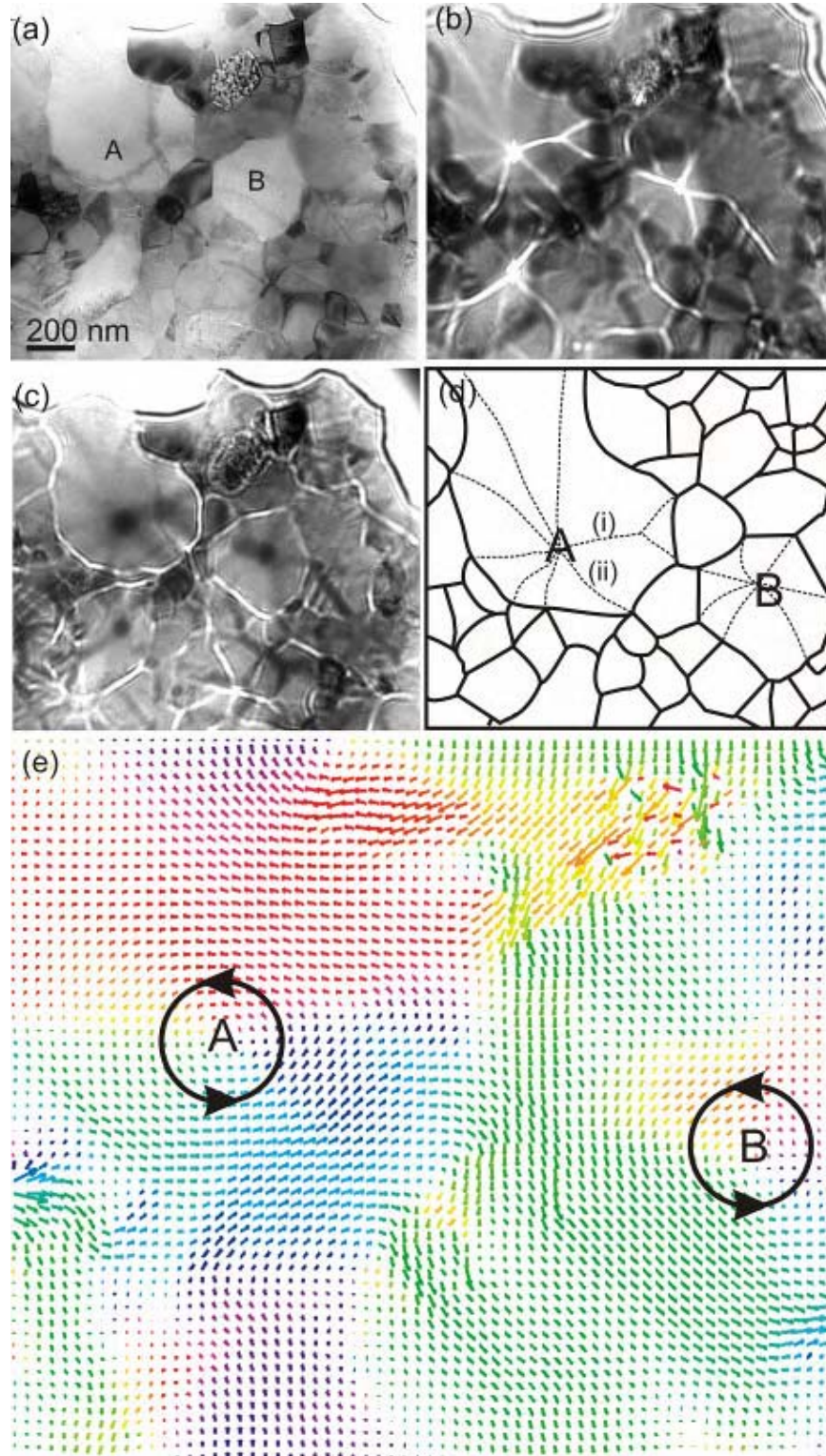
Figure 21 – Microstructure and underlying domain configuration of the splat/annealed Y:11Fe:Ti material. (a) Overfocused: $\Delta f = +213$ mm, (b) in focus: $\Delta f = 0$ mm, (c) underfocused: $\Delta f = -144$ mm. (d) Scheme showing the correspondence between domain wall position in grains A and B and the presence of neighbour grain boundaries. (e) Calculated projected local induction distribution for $\Delta f = \pm 100$ mm, where the circles indicate the magnetization curling around vortices in α-Fe(Ti) grains.

Figures 22 and 23 present averaged and normalized EDS spectra obtained at $YFe_{11-x}Ti_y$ and at α-Fe(Ti) grains in both splat-quenched and splat/annealed conditions as well as the respective differences. A spectrum obtained in a Fe_2Ti grain is also shown in Figure 23. The difference between the $YFe_{11-x}Ti_y$ spectra in Figure 22 (c) shows that both Fe and Ti rejection occurred during the heat treatment, i.e., x increased while y decreased during the heat treatment. On the other hand, the difference between the α-Fe(Ti) spectra in Figure 23 (c) demonstrates that this phase enriched in Ti during the heat-treatment. Segregation of Ti from $YFe_{11-x}Ti_y$ was in fact enough to supersaturate α-Fe(Ti) in Ti, as the Fe_2Ti precipitation demonstrates (see Figures 17 (f) and Figure 23 (d)), together with the better Fe_2Ti peak definition in the splat/annealed diffractogram in Figure 16).

Planar defects with twin appearance (arrows in Figure 24 (a) and Figure 25) and other 2-D defects displaying the strong contrast and contours characteristic of thermal antiphase boundaries have been observed in $YFe_{11-x}Ti_y$ grains (see Figure 24 (c)). The lack of contrast reversal at twin boundaries demonstrated that the twin planes themselves are not associated with domain walls (Figure 25). In Figure 25 (b) and (c) it is possible to distinguish that internal domain walls show higher contrast inside the twinned region, which suggests that the domain walls may have changed their character across the mirror plane. On the other hand, no wall disturbance or pinning effect by antiphase boundaries could be detected in $YFe_{11-x}Ti_y$ grains.
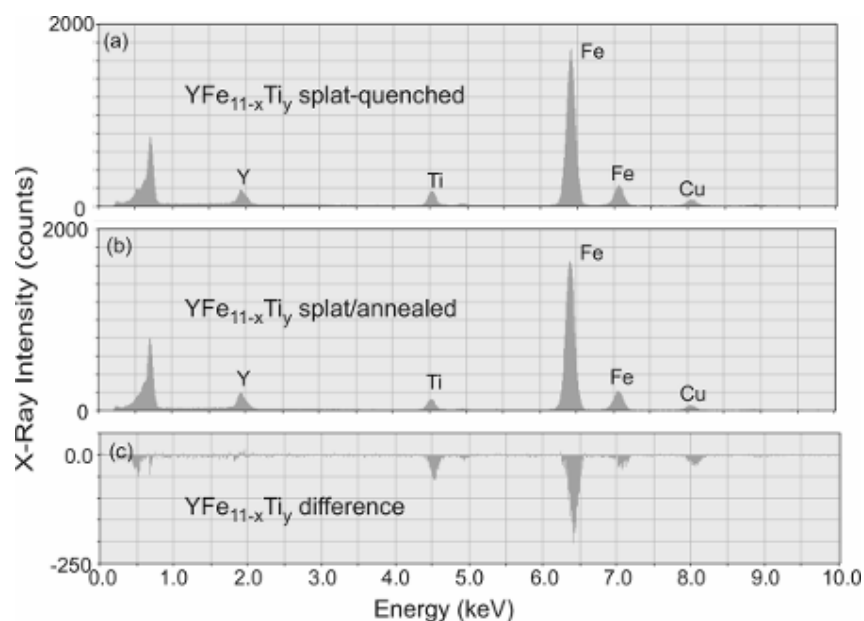
Figure 22 – EDS results obtained with Y:11Fe:Ti. Averaged spectra resulting from 5 point analyses performed on YFe$_{11-x}$Ti$_y$ grains of the splat-quenched material (a) and splat/annealed material (b). These averaged spectra were normalized by equalizing the Y counts. (c) Difference between the averaged spectra.

Figure 23 –EDS results obtained with Y:11Fe:Ti. Averaged spectra resulting from 5 point analyses performed on α-Fe(Ti) grains of the splat-quenched material (a) and splat/annealed material (b). These averaged spectra were normalized by equalizing the Fe counts. (c) Difference between the averaged spectra. (d) Spectrum obtained at a Fe$_2$Ti grain.
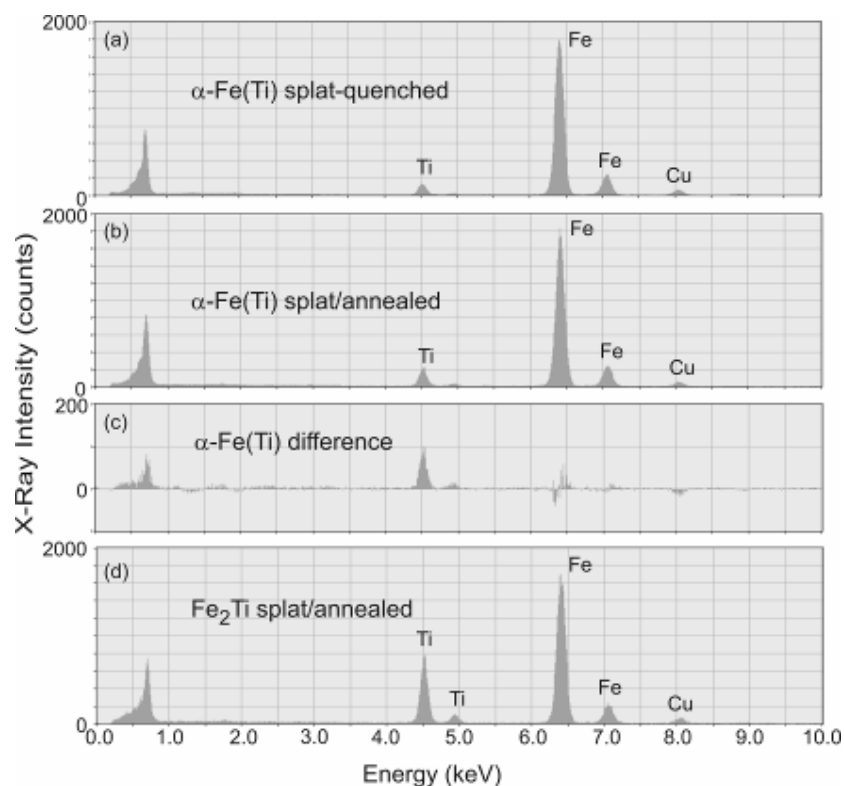
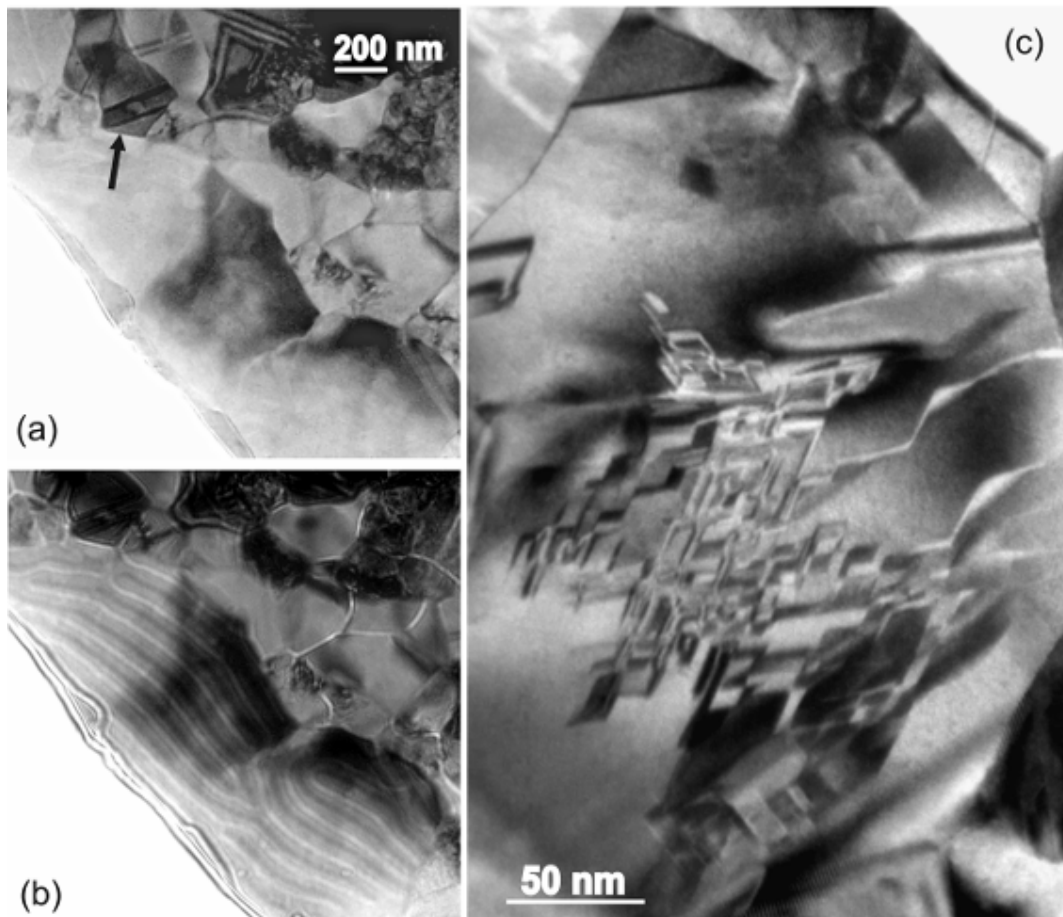Figure 24 – TEM and Lorentz images of the Y:11Fe:Ti splat-quenched/annealed material. In focus image showing a planar defect with twin appearance (a) and overfocused image (b) obtained at the same region showing magnetic domains with an antiparallel stripe pattern crossing two large $YFe_{11-x}Ti_y$ grains. Bright-field image of a large $YFe_{11-x}Ti_y$ grain presenting thermal antiphase boundaries (c).
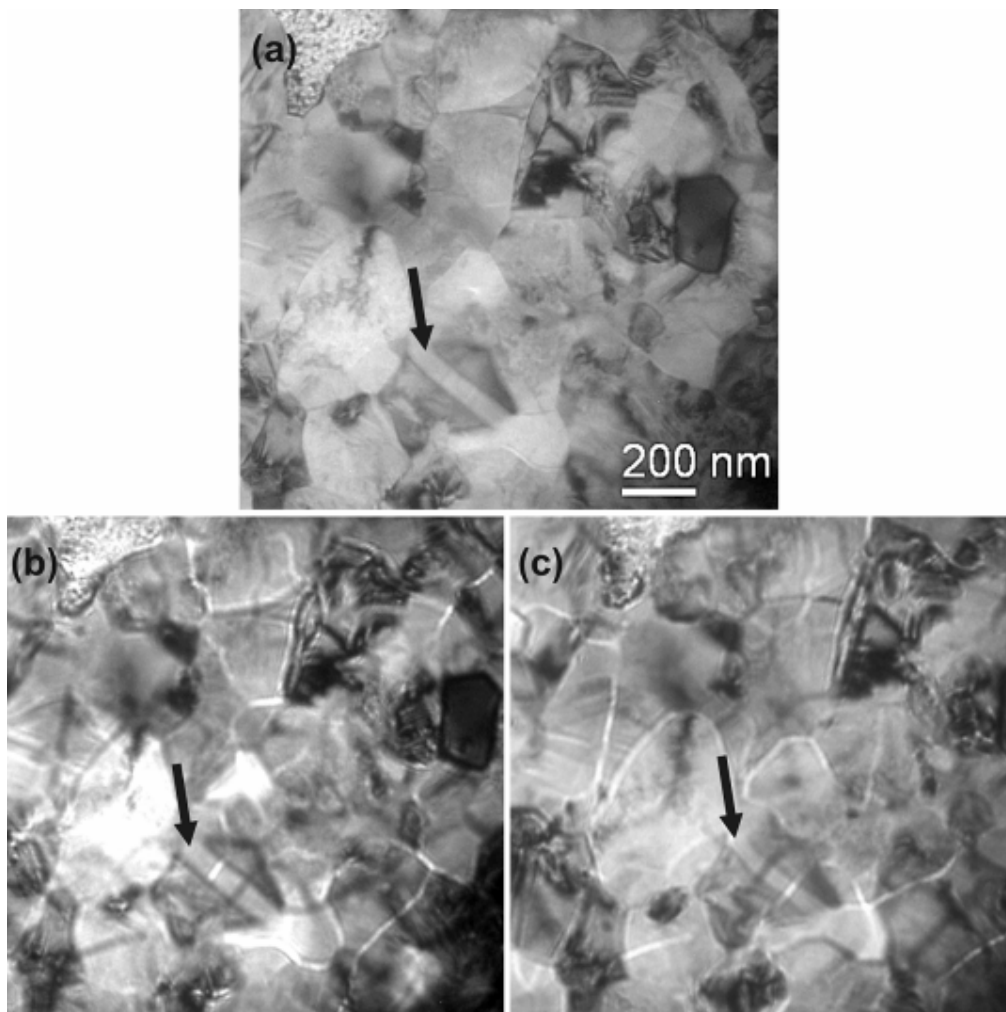
Figure 25 – Lorentz images of the Y:11Fe:Ti splat-quenched/annealed material. (a) In focus image of a region with a twinned grain (arrow), (b) corresponding overfocused image and (c) underfocused image.

The MFM results presented in Figure 26 show that for the splat/annealed condition, the material under the bulk form displays domain configurations slightly distinct from the ones observed by Lorentz Microscopy (Figures 22, 24 and 25). In both types of observation, domain walls are largely concentrated at grain boundaries. However, while stripe/maze domains are present in large $YFe_{11-x}Ti_y$ grains both at the surface of the bulk material (see the arrows in Figure 26 (b)) as well as in thin films (see Figure 24 (b)), vortices in large α-Fe(Ti) grains appear only in thin films (see Figure 21). Figure 26 demonstrates that the magnetic domain scale after annealing is comparable to the one of the splat-quenched material (compare with Figure 20).
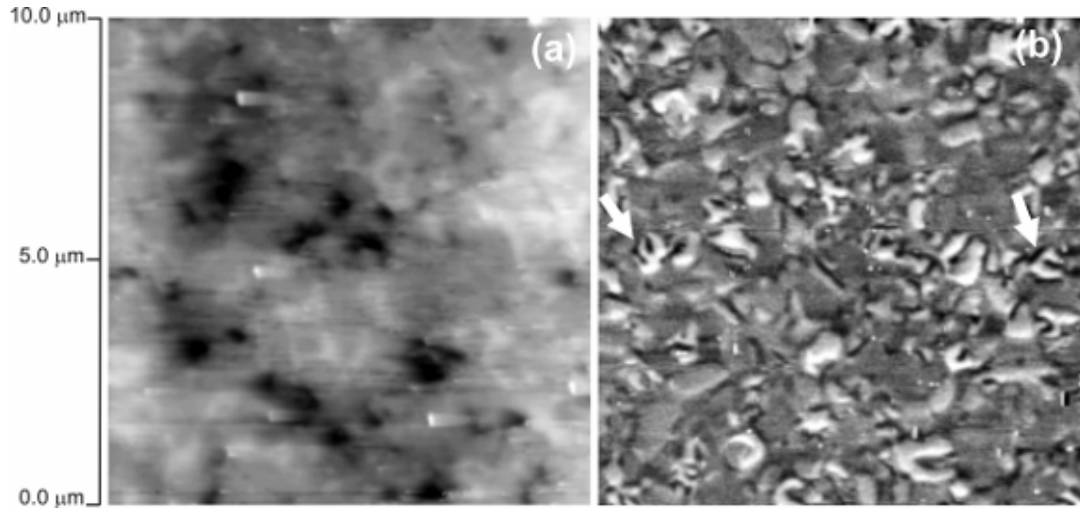

Figure 26 - (a) MFM images of the Y:11Fe:Ti splat/annealed material surface. (a) Topographical image (tapping mode) where the bright elevated regions are foreign matter, (b) phase image obtained under lift mode with a magnetized CoCr tip over the same area as (a) where the phase range is 10°. The arrows in (b) point to apparent stripe domains.

Magnetization curves at room temperature obtained with the splat-quenched and splat/annealed materials are presented in Figure 27. The smooth appearance indicates that both magnetic phases, $YFe_{11-x}Ti_y$ and α-Fe(Ti), exhibit similar magnetization behavior with combined saturation magnetization (M_s) at 5 Tesla of 18.0 μ_B/fu and 18.5 μ_B/fu for the splat-quenched and splat-annealed conditions, respectively. These results are slightly higher than 16.6 μ_B/fu at 293K, values published for $YFe_{11}Ti$ in the literature [1,9].
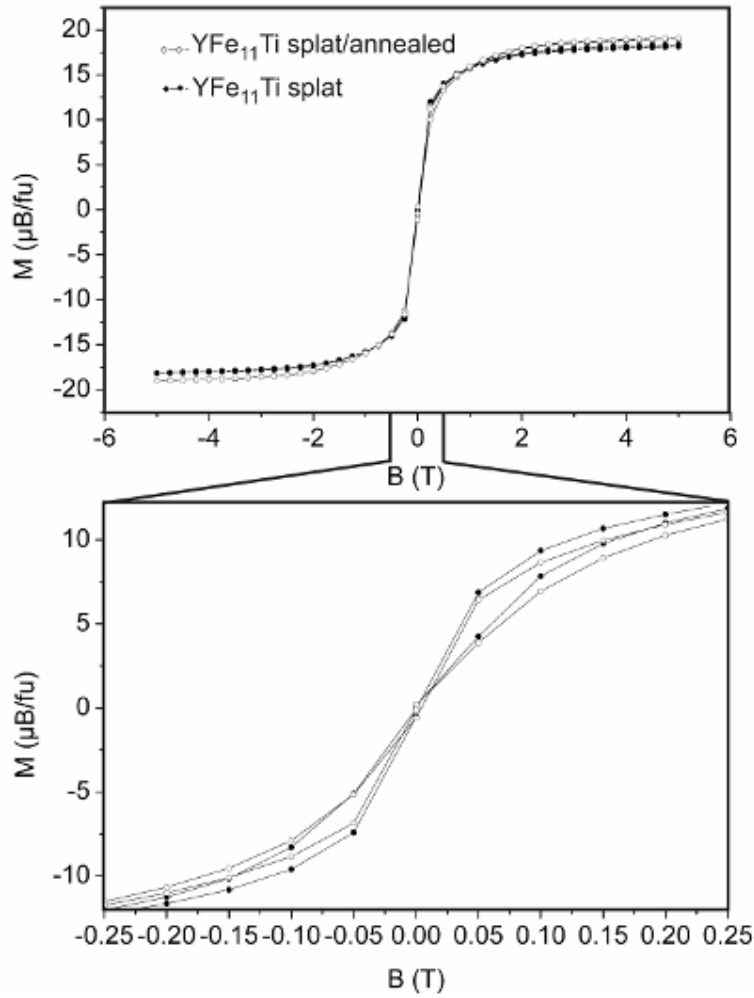

Figure 27 – Magnetic field dependence of the magnetization at 298 K for the splat and splat/annealed Y:11Fe:Ti materials.

3.4. Discussion

Structural Stability

The microstructure morphologies and the EDS results show that the primary crystallization structure in the Y:11Fe:Ti alloy is ThMn$_{12}$-type YFe$_{11-x}$Ti$_y$. Evidence for other primary crystallization structures has been found in similar systems. Namely, Margarian *et al* [36] showed that a monoclinic Nd$_3$(Fe,Ti)$_{29}$ structure forms in the Nd-Fe-Ti system. This phase has a composition close to the one corresponding to the ThMn$_{12}$-type phase and a structure derived as well from CaCu$_5$ [64], which is a basic structure for rare-earth-transition-metal (R-T) compounds. On the other hand, Hu *et al* [12] reported that alloys presenting an YFe$_{11-x}$Ti$_x$ stoichiometry with x<0.7 crystallize according to a hexagonal Th$_2$Ni$_{17}$-type structure, which can be obtained by an ordered substitution of dumbbell pairs of M atoms by R atoms in the CaCu$_5$-type structure [64]. In the current work, although the presence of α-Fe(Ti) implies a convergence of the Fe/R ratio towards the proportions of the above phases, no XRD peaks specific to monoclinic Y$_3$(Fe,Ti)$_{29}$ or hexagonal Y$_2$(Fe,Ti)$_{17}$ compounds could be detected in the as-cast or splat condition diffractograms (compare in Figure 16 the corresponding simulations with the experimental diffractograms, where the minor peaks at 40.9° are likely to origin from Fe$_2$Ti). Consequently, Nd$_3$(Fe,Ti)$_{29}$ or Th$_2$Ni$_{17}$ crystallization types are not occurring in the Y:11Fe:Ti alloy under the studied conditions.

The presence of α-Fe(Ti) demonstrates the existence of active solute partition between the liquid and solid phases during both solidification routes. Higher segregation levels denote a less efficient backdiffusion from the solidification front into the solid [65].Consequently, it can be inferred that backdiffusion has been more severely impaired in splat-quenching than in arc melting. Therefore, the cooling rate of the splat-quenching process was not high enough to set the solid/liquid interface under the severe non-equilibrium conditions necessary to prevent partition.

Regarding the stability of the ThMn$_{12}$-type phase, Jang and Stadelmaier demonstrated that the NdFe$_{11}$Ti compound is unstable at temperatures below 1000 °C, decomposing by a solid-state reaction into Nd$_2$(Fe,Ti)$_{17}$ (with a rhombohedral Th$_2$Zn$_{17}$-type structure), Fe$_2$Ti

and α-Fe(Ti) [66]. In the current system, the X-ray diffractograms of both annealed conditions (see Figure 16) do not evidence any of the peaks specific to a rhombohedral Y_2Fe_{17} structure nor its peak proportions and, furthermore, a structural transformation could not be detected in the microstructure. Therefore, these results indicate that the tetragonal $YFe_{11-x}Ti_y$ phase is in equilibrium with Fe_2Ti and α-Fe(Ti) at 950 °C and 800 °C and that the $ThMn_{12}$-type $\rightarrow$ $ThZn_{17}$-type + Fe_2Ti + α-Fe(Ti) transformation reported for the Nd-Fe-Ti system [36,64] does not take place in the present alloy at these temperatures. Nevertheless, the better definition of Fe_2Ti peaks at 40.9° and 45.3° in Figure 16 for both annealed conditions, together with the microstructures in Figure 17 and the EDS spectra presented in Figures 22 and 23, demonstrates that segregation from the $ThMn_{12}$-type phase during annealing was (relatively) higher for Ti than for Fe and that a $ThMn_{12}$-type $\rightarrow$ $ThMn_{12}$-type + Fe_2Ti + α-Fe(Ti) transformation took place at 950 °C and 800 °C. The precipitation of Fe_2Ti was also responsible for the α-Fe(Ti) lattice parameter decrease.

The Fe and Ti segregation during the heat-treatments (see Figure 16) are indicative of interesting structural modifications. The lower α-Fe peak intensity observed after the heat treatment at 950 °C (1536 h), as compared with annealing at 800 °C (2208 h), reveals that the equilibrium iron content in the $ThMn_{12}$-type structure is considerably higher at 950 °C. On the whole, the variations of α-Fe(Ti) proportion in the studied conditions evidence a homogeneity range such as the ones reported for the Y-Fe-Mo [67], Nd-Fe-Mo [65], and Gd-Fe-Mo [68] systems. This behavior has been proposed to result from the presence of structural point defects involving partial substitution of Fe/M by rare-earth atoms at the *8i* sites and from the presence of Fe vacancies at the *8f* and *8j* sites [68]. However, in view of (i) the Y-Y and Y-Fe/Ti interatomic distances (determined from the structure simulated with PowderCell: ~3 Å and ~2.6 Å, respectively), (ii) considering the difference in metallic radius (1.26 Å for Fe, 1.46 Å for Ti and 1.81 Å for Y, for a coordination number of 12 [69]) and taking into account the (iii) limited lattice parameter evolution, iron vacancies are more likely to be occurring. The lattice parameters of the splat-quenched $YFe_{11-x}Ti_y$ phase showed an extremely limited evolution during the heat-treatment in spite of the strong iron rejection as indicated by the XRD and EDS maps and point analysis. These results suggest that the fraction of structural point defects adapt to processing parameters such as cooling rate

and annealing temperature. Planar defects were commonly observed in $YFe_{11-x}Ti_y$ grains (Figure 24), however even if the R:11Fe:Ti proportion of chemical species is not preserved at the defects, their presence would not be sufficiently extensive to fully justify the observed homogeneity range. This contributes to reinforce the structural vacancy/replacement hypothesis.

It should be emphasized that reports on the occurrence of α-Fe(M) in R:11T:M alloys under similar processing conditions vary without a consistent justification. Namely, the presence of soft M(T) solid solutions has been reported for R:11T:M alloys with R = Y, Er; T = Fe, Co and M = Ti, V, Si after preparation by arc furnace and annealing at 900 °C [70]; α-Fe was observed in a series of R:11Fe:Ti alloys (with R =Y, Gd, Tb, Dy, Ho) prepared by melting in a resistance furnace and slowly cooled through the melting temperature [16]; however, α-Fe could not be detected after preparation of the Y:11Fe:Ti alloy by induction melting followed by annealing at 900 °C [13,14]. Since the stoichiometry/solubility range is seldom discussed in terms of thermodynamic stability and crystallization kinetics, a more comprehensive understanding of the structure and intrinsic properties of these compounds seems required.

Magnetic microstructure

In the non-interacting limit and under a 'hard magnetic tip response' regime, where the perturbation of the tip magnetic state by the sample stray fields can be neglected, contrast variations in dynamic MFM phase images can be simply ascribed to variations in the second gradient of the sample stray field with respect to the surface normal (flat sample) [62]. Under these conditions it has been shown that the type of contrast depends on the lift mode separation in relation to the domain size [71]: domain wall contrast appears for scan heights much lower than the magnetic configuration scale, otherwise domain contrast itself is produced. In the present work, MFM images display domain contrast, which seems to be justified by the fact that the scale of the domain configurations is comparable to the scan height (60 nm).

The domain configuration in the upper grain of Figure 18 (b) shows what appear to be conically shaped bright regions immersed in domains with (dark) reversed contrast. However, other bright conically shaped regions are surrounded by domains with similar contrast. This behavior suggests that the domain walls and/or the magnetization vectors are at a sharp angle to the surface, since MFM imaging is substantially insensitive to in-plane components of the magnetization and tends to generate small contrast variations for opposite nearly in-plane magnetizations. The domain configurations of the large grain in Figure 18 (b) and of the magnified detail in Figure 18 (c) can be interpreted as follows: sufficiently thin uniaxial ferromagnetic materials present stripe/maze domain configurations, however as specimens thicken the domain configuration firstly displays Block wall undulation near the surface, and finally the formation of surface reverse spikes occurs for still thicker crystals. Thus, the grain in Figure 18 (c) is thickening from the upper to the lower region, where spikes start to emerge, and the large grain at the top of Figure 18 (b) is even thicker. The fairly ragged domain configuration at the central/lower region of the grain in Figure 18 (c), as compared with the configurations observed for example for NdFeB crystals [72], is in agreement with the relatively more moderate anisotropy field reported for $YFe_{11}Ti$ (~2 T [1]).

The results presented in Figures 19 and 20 show that, at the finer microstructural scale of the splat-quenched material, the magnetic domains correspond roughly to individual crystallites. Therefore, formation of domain walls in the fine crystallites is energetically unfavorable and domain walls have been essentially expelled to the grain boundaries. Furthermore, at this microstructural scale the material displays similar domain configurations in bulk surfaces (MFM image in Figure 20 (b)) and thin films (Lorentz microscopy image in Figure 20 (b) and (c)). The results indicate that the critical size for single-domain behavior in both α-Fe(Ti) and $YFe_{11-x}Ti_y$ is close to 200 nm.

Although after annealing grain boundaries continued extensively associated with domain walls, internal magnetic structure was frequently observed in both α-Fe(Ti) and $YFe_{11-x}Ti_y$ grains as seen in Figures 22 and 25. Closure configurations with four magnetic domains have been reported previously for α-Fe particles [73]. However, the

high number of domains involved in the vortices of Figure 22 is unusual and points to non-equilibrium magnetization configurations. A close inspection to the magnetic structure of grains A and B shows that vortex internal walls and walls at the grain boundaries display opposite contrast (Figure 22 (b) and (c)). Furthermore, the position of vortex walls at the grain boundary coincides with the local presence of boundaries/walls of adjacent grains (Figure 22 (d)). Assuming that the second term of equation (4) is correctly calculated, the vectorial map shown in Figure 21 (e) can be used to roughly discuss the induction distribution in Figure 21 (a): the in-plane components of the magnetic induction show counterclockwise patterns in A and B vortices; if potential and thickness variations are not critically affecting the phase contrast, there is no simple relation between the magnetization of the vortex domains and the magnetization of adjacent grains; the induction distribution across α-Fe(Ti) domain walls suggests that, for example, (i) is a 90° wall with an out-of-plane Bloch character, whereas (ii) is a 45° wall with in-plane Néel character. The correlation between the position of the vortex walls at the grain boundaries and the arrangement of the neighbouring $YFe_{11-x}Ti_y$ grains (Figure 21 (d)) indicates that strong magnetostatic interactions are responsible for the observed magnetic microstructure in the isotropic α-Fe(Ti) grains, which show a flexible accommodation to the complex demagnetizing fields generated by $YFe_{11-x}Ti_y$ grains.

$YFe_{11}Ti$ is ferromagnetic and exhibits uniaxial magnetic anisotropy, with c as the easy magnetization axis, as a result of the Fe sub-lattice [1,2]. However, in spite of the reported anisotropy, the phase presents a soft behavior (see Figure 12). The lack of coercivity in the studied materials demonstrates that grain boundaries and planar defects are not effective pinning sites for domain walls. The saturation magnetization of the splat-quenched material (18.0 μ_B/f.u.) is higher than the value reported in the literature for $YFe_{11}Ti$ (16.6 μ_B/f.u. in Ref. [1]). This seems to be justified by the reinforcing presence of α-Fe(Ti) and is in agreement with the fact that the saturation magnetization increased for the splat/annealed condition (18.5 μ_B/f.u.) where the presence of α-Fe(Ti) is higher.

The domain structure of sufficiently thin uniaxial crystals with magnetic anisotropy can be described by Kittel's parallel-plate domain configuration [74], for which the dependence of domain width D on the crystal thickness L, taking into account the μ-correction introduced by Kooy and Enz [75], is given by:

$$D = \left[\frac{\gamma\left(1+\mu^{1/2}\right)}{3.4M_s^2} \right]^{1/2} . L^{1/2} \qquad (12)$$

where γ is the domain wall energy, M_s is the saturation magnetization and μ is the rotational permeability of the material given by:

$$\mu = 1 + \frac{2\pi M_s^2}{K} \qquad (13)$$

with K the magnetic anisotropy constant. The μ effect is related to the deviation of the magnetization from the magnetic easy axis due to the stray field [72]. As a result, the domain wall energy can be roughly derived from the domain width measured on fairly regular and parallel domain structures using eq. (12). Assuming a crystal thickness in the 40-80 nm range and a domain width of ~75 nm (Figures 24 and 25), using K=1.0x10^7 erg/cm^3 (K=1.0x10^6 J/m^3 or 1MJ/m^3 in Ref. [1]) and estimating M_s to be 886 G (8.86x10^5 Am^{-1} calculated from 16.6 μ_B/f.u. in Ref. [1] using the lattice parameters presented in Figure 16 to determine the specific mass) results in γ = 8-17 erg/cm^2 (8-17 x10^{-3} J/m^2). This value range can be tested through the scale of the magnetic configurations in Figure 18: the critical thicknesses for the occurrence of wavy structure and reverse spike domains are predicted to be $26.39\gamma/\mu^2 M_s^2$ [76,77] and $16\pi^2\gamma/1.73\mu^2 M_s^2$ [77,78], i.e. 1.3-2.5 µm and 4.4-8.8 µm, respectively. These values are in fair agreement with the grain scales in Figure 18 (b).

3.5. Summary

- The as-cast and splat-quenched materials crystallized adopting essentially the $ThMn_{12}$-type structure, though the $RFe_{11}M$ stoichiometry was not strictly followed.

- No evidence for $Nd_3(Fe,Ti)_{29}$ or Th_2Ni_{17} phase types could be found in the Y:11Fe:Ti alloy crystallization path. Moreover, a $ThMn_{12}$-type$\rightarrow$$Th_2Zn_{17}$-type structural transformation does not occur at the annealing temperatures investigated.

- The variation of the α-Fe phase proportion in the studied conditions demonstrates a homogeneity range such as the ones reported for the Y-Fe-Mo, Nd-Fe-Mo and Gd-Fe-Mo systems, which together with the limited latticed parameter evolution supports the hypothesis of iron vacancies in the $ThMn_{12}$-type structure.

- The splat condition displayed similar magnetic microstructures under both bulk and thin film forms. Formation of domain walls in the fine crystallites was energetically unfavorable and domain walls have been essentially expelled to the grain boundaries indicating that the critical size for single-domain behavior is close to 200 nm.

- In the splat/annealed condition grain boundaries were still largely associated with domain walls. However large $YFe_{11-x}Ti_y$ grains displayed internal domain walls following stripe/maze patterns, characteristic of high anisotropy thin films, both under thin film form and at bulk surfaces. Vortex configurations resulting from accommodation to the demagnetizing fields of neighboring $YFe_{11-x}Ti_y$ were common in large α-Fe(Ti) grains under thin film form. Out-of-plane Bloch and in-plane Néel character could be detected in the vortex walls.

- Planar defects with twin appearance and other 2-D defects displaying the strong contrast and contours characteristic of thermal antiphase boundaries have been observed in $YFe_{11-x}Ti_y$ grains. No pinning effect or wall disturbance by antiphase boundaries could be detected in $YFe_{11-x}Ti_y$ grains.

- A domain wall energy of 8-17 mJ/m^2 has been estimated for $YFe_{11-x}Ti_y$.

4. Y-Fe-Mo system (Y:11Fe:Mo alloy)

4.1. Introduction

Among the iron-based $ThMn_{12}$-type systems, the $RFe_{11}Mo$ series has been extensively investigated [6,7,27-29,79-82]. Systematic analyses carried out on the series enabled to evaluate the temperature dependence of magnetic properties and clarified field-induced magnetic transitions observed in the $ThMn_{12}$ intermetallic class [6,7,28,29,79,80,82]. $YFe_{11}Mo$ is ferromagnetic, exhibits uniaxial magnetic anisotropy that results from the Fe sublattice with c as the easy magnetization axis [1,2]. A homogeneity range for $Y(Fe,Mo)_{12}$ has been reported [67]. The Curie temperature of the phase decreases with Mo concentration, since Mo atoms substitute Fe atoms in the i sites of largest magnetic moment [6].

Nevertheless, in spite of the vast number of fundamental studies on the magnetic behavior of $RFe_{11}Mo$ compounds, no magnetic domain configuration or microstructural characterizations seem to have been carried out for these materials.

4.2. Experimental details

Alloys preparation and heat treatments

The alloys were prepared by melting the elements with ≥99.9 % purity in an arc furnace, under argon atmosphere on a water-cooled crucible. In order to increase homogeneity, the samples were melted at least three times (as-cast condition). The weighted elemental quantities corresponding to the $YFe_{11}Mo$ stoichiometry were 1.2767 mg for iron, 0.1846 mg for yttrium and 0.1900 mg for molybdenum, with a mass loss after fusion of ~1 %.

Part of the as-cast material was subsequently sealed in evacuated quartz tubes and annealed at 950 °C for 1536 h (cast/annealed condition). Another portion of the as-cast material was remolten and splat-quenched by cooling down a droplet of the prepared alloy between two copper pistons shot against each other at ~9 ms^{-1}. A cooling rate of

$\sim 10^6$ Ks^{-1} is obtained by this method and the resulting disks have a diameter of ~ 20 mm and a thickness of ~ 100 μm (splat condition). A fraction of the splat-quenched material was subsequently sealed in evacuated quartz tubes and annealed at 800 °C for 2208 h (splat/annealed condition).

X-ray powder diffractograms

X-ray powder diffractograms of the materials have been obtained at room temperature using a Panalytical X'Pert Pro powder diffractometer. Samples were crushed down to a fine powder and deposited onto a low noise (single crystalline Si) sample holder. The data acquisition was made with a 2θ - step size of 0.03º. The software package PowderCell [57] was used to simulate diffractograms for comparison with experimental data. An YFe$_{11}$Mo unit cell with ThMn$_{12}$-type of structure was built based on the crystallographic information listed in [58], and by assuming that 75% of the *8i* positions were occupied by Fe and 25% by Mo, using the lattice parameters reported in [82]. A cell of the Th$_2$Zn$_{17}$ type was built based on the crystallographic information and lattice parameters reported in [59] and, for simplicity, by assuming an Y$_2$Fe$_{17}$ stoichiometry. A cell of the Th$_2$Ni$_{17}$ type was built also assuming an Y$_2$Fe$_{17}$ stoichiometry and using the crystallographic information and lattice parameters listed in [60]. A cell for a Y$_3$Fe(Mo)$_{29}$ phase with a Nd$_3$(Fe,Ti)$_{29}$-type structure has also been built considering the *A2/m* space group with base on the crystallographic information listed in [61] and using the lattice parameters presented in [62].

SEM

Sample preparation for scanning electron microscopy involved grinding with silicon carbide paper and consecutive polishing with 6, 3 and 1 μm diamond suspensions. Final polishing and light etching were obtained with a commercial alumina suspension in an acid solution (OPS-Struers). The observations have been performed with a Hitachi S2400 instrument equipped for energy dispersive X-ray spectrometry and a field emission JEOL 7001F equipped for dispersive X-ray spectrometry after further etching with an aqueous solution of HF, HCl and HNO$_3$.

AFM and MFM

Sample preparation for atomic and magnetic force microscopy involved the metallographic steps described above plus final polishing with a 0.1 μm diamond suspension. The observations have been performed with a Veeco di CP-II atomic force microscope using commercially available MFM cantilevers (MESP-CPMT) with nominal length of 225 μm and nominal spring constant of 2.8 N/m. The MESP-CPMT tips are coated by a CoCr alloy and have a nominal curvature radius of 25 nm. The tips are magnetized along their axis and have a coercivity of ~400 Oe. In lift mode the tip-sample separation (Z) was kept aorund 60 nm. MFM observations have been carried out under dynamic conditions using the sequential two-scan method.

TEM/Lorentz Microscopy

For transmission electron microscopy, sample preparation involved cutting a disc with a diameter of 3 millimetres and grinding until a thickness around 80 micrometers was reached. The samples were thinned to electron transparency by argon ion milling using a Gatan-Duo Mill machine, operating at an accelerated voltage of 4 kV, with a 14° incidence angle. TEM observations have been performed at 200 kV with a JEOL 2010F microscope equipped for energy dispersive X-ray spectroscopy. Magnetic domain observations by Lorentz microscopy have been performed using the JEOL 2010F instrument with the objective lens switched off and using the intermediate lens as image forming lens.

Magnetization isotherm cycles

Magnetization isotherm cycles at room temperature were performed using a multipurpose characterization system *MagLab* 2000 (Oxford Instruments) with magnetic fields up to 5 T. Crushed powder particles of the splat-quenched and splat/annealed materials were fixed under random orientation with acetone soluble glue, which prevented rotation of individual particles under the applied magnetic field.

4.3. Results

X- Ray Diffraction

Figure 28 presents experimental X-ray diffractograms of the Y:11Fe:Mo alloy obtained for the as-cast, splat-quenched and annealed conditions, along with simulations for the ThMn$_{12}$ structure and other related structures. The results indicate that both the as-cast and splat-quenched materials crystallized adopting essentially the ThMn$_{12}$-type structure. However, the presence of α-Fe(Mo) peaks at ~44.7° shows that the YFe$_{11}$Mo stoichiometry is not strictly followed. For this reason the ThMn$_{12}$-type phase will be hereafter denominated YFe$_{11-x}$Mo$_y$, where x and y are variables that depend on the material condition. The peak intensities show that the volume fraction of α-Fe(Mo) resulting from splat-quenching is slightly lower than the one resulting from arc furnace solidification (as-cast condition). However, while the α-Fe(Mo) peak intensity remained approximately constant for the as-cast condition after annealing at 950 °C; annealing at 800 °C induced a significant increase of the α-Fe(Mo) proportion for the splat condition. The lattice parameters determined for the tetragonal YFe$_{11-x}$Mo$_y$ phase in all the studied conditions (legends in Figure 28) are in fair agreement with the ones reported for YFe$_{11}$Mo [7,29,82]. The α-Fe(Mo) lattice parameter was a_{cast} = 0.288 nm for the as-cast condition and a_{splat} = 0.289 nm for the splat condition, the annealing treatments induced lattice parameter decreases of, respectively, $\left(a_{\text{cast/annealed}} - a_{\text{cast}}\right)/a_{\text{cast}}$ = -0.4 % and $\left(a_{\text{splat/annealed}} - a_{\text{splat}}\right)/a_{\text{splat}}$ = -0.6 %. The α-Fe(Mo) lattice parameter reduction with the annealing treatments induced clearly evident peak shifts in Figure 28.

As-cast and cast/annealed microstructures

Figures 29 to 31 present typical microstructures of the as-cast and cast/annealed material obtained by SEM and corresponding EDS maps. As expected from the XRD results, the predominant phase in the as-cast microstructure is the tetragonal YFe$_{11-x}$Mo$_y$, which displays a cellular dendritic morphology, with intercellular distances typically in the 30 μm range. The microstructure shows a considerable presence of α-Fe(Mo), which together with YFe$_{11-x}$Mo$_y$ forms a coarse intercellular eutectic mixture. Y was found only at the YFe$_{11-x}$Mo$_y$ cells and no compositional variation could be detected in these regions by either X-ray mapping or point analysis. A homogeneous Mo concentration was detected in both phases (see Mo map in Figure 29).
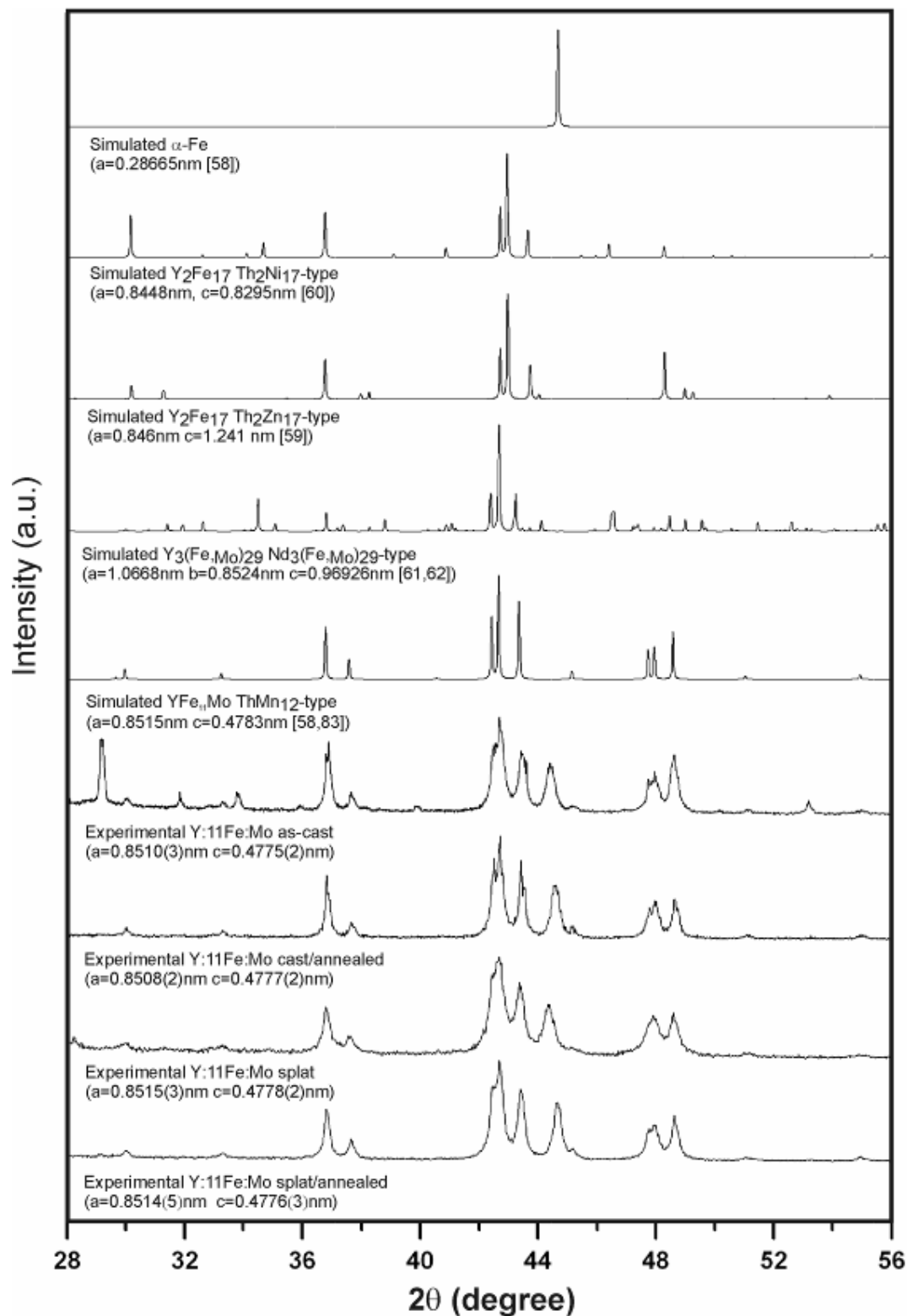
Figure 28 – Experimental X-ray diffractograms for the Y:11Fe:Mo alloy under as-cast, cast/annealed, splat and splat/annealed conditions (simulations for α-Fe, YFe$_{11}$Mo (ThMn$_{12}$-type), Y$_2$Fe$_{17}$ (Th$_2$Zn$_{17}$ and Th$_2$Ni$_{17}$-types) and Y$_3$Fe(Mo)$_{29}$ (Nd$_3$(Fe,Ti)$_{29}$-type) are included. Lattice parameters, determined assuming a stoichiometric YFe$_{11}$Mo structure, are indicated above each experimental diffractogram.
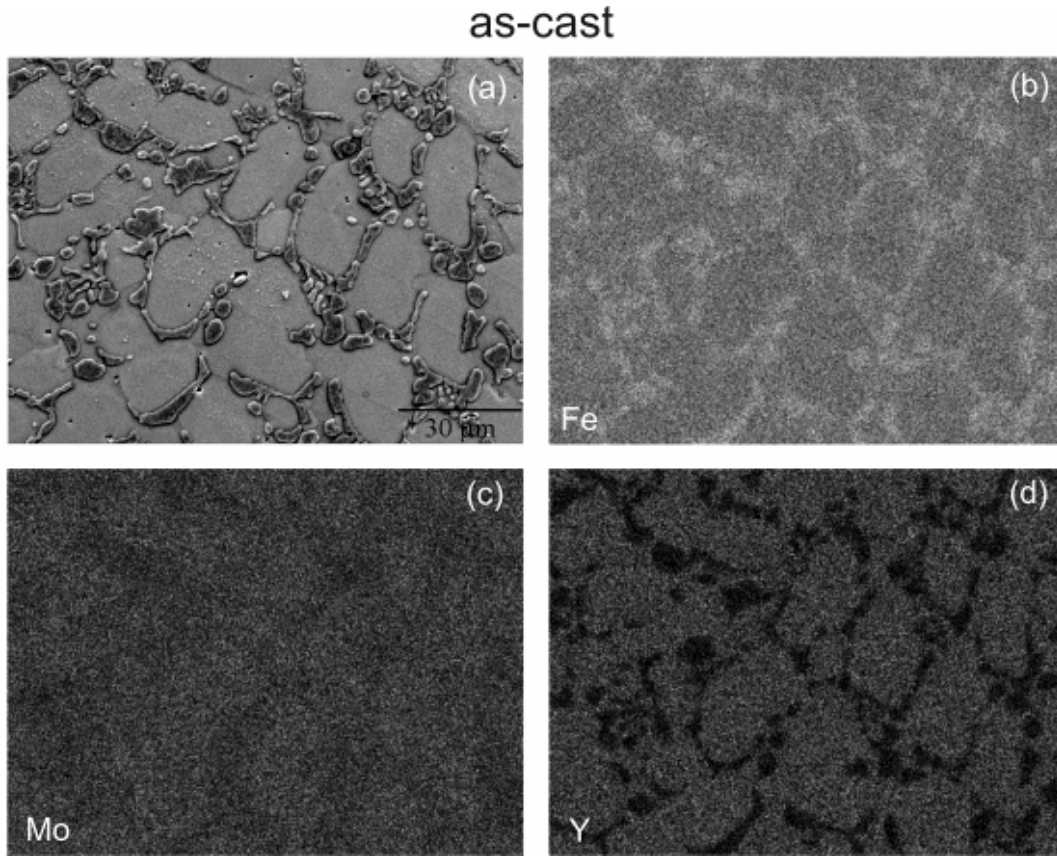
Figure 29 –Y:11Fe:Mo alloy under the as-cast condition (etched sample). (a) Secondary electron image of the corresponding X-ray maps for Fe (b), Mo (c) and Y (d). EDS point analyses showed that the cellular structure corresponds to a primary crystallization of $YFe_{11-x}Mo_y$ with a α-Fe(Mo) + $YFe_{11-x}Mo_y$ eutectic mixture at the intercellular regions.

The microstructure of the cast/annealed condition presented in Figures 30 (a) and 31 (a) shows that the $YFe_{11-x}Mo_y$ phase did not coarsen significantly during annealing (compare with Figure 29 (a)). The Mo maps evidence that the concentration of this element decreased in α-Fe(Mo) during the heat treatment (compare Figure 30 (c) with Figure 29 (c)). The Y maps point to Y segregation from the $YFe_{11-x}Mo_y$ phase, with precipitation in the intercellular regions (Figures 29 (d), 30 (d) and 31 (b)). The sample preparation process resulted in the oxidation of the Y precipitates, as the oxygen map in Figure 31 (c) and the SE image in Figure 31 (d)) evidence. Figure 32 presents averaged and normalized EDS spectra obtained at $YFe_{11-x}Mo_y$ grains under both splat-quenched (a) and splat/annealed (b) conditions. The difference between the $YFe_{11-x}Mo_y$ spectra in Figure 32 (c) shows that a strong Fe rejection occurred during the annealing treatment.

As a result of this segregation there was an iron enrichment in the α-Fe(Mo) phase. This justifies the lower Mo concentration at the interdendritic regions observed in the X-ray maps (compare Figure 30 (c) with 29 (c)), as well as the lattice parameter reduction inferred from the XRD peak shift of the α-Fe(Mo) phase. However, the lattice parameter reduction of α-Fe(Mo) was not accompanied by comparable (but opposite) variations for the $YFe_{11-x}Mo_y$ phase. The better definition of the XRD peaks for $YFe_{11-x}Mo_y$ after annealing indicates a structural reorganization in the $ThMn_{12}$-type phase.
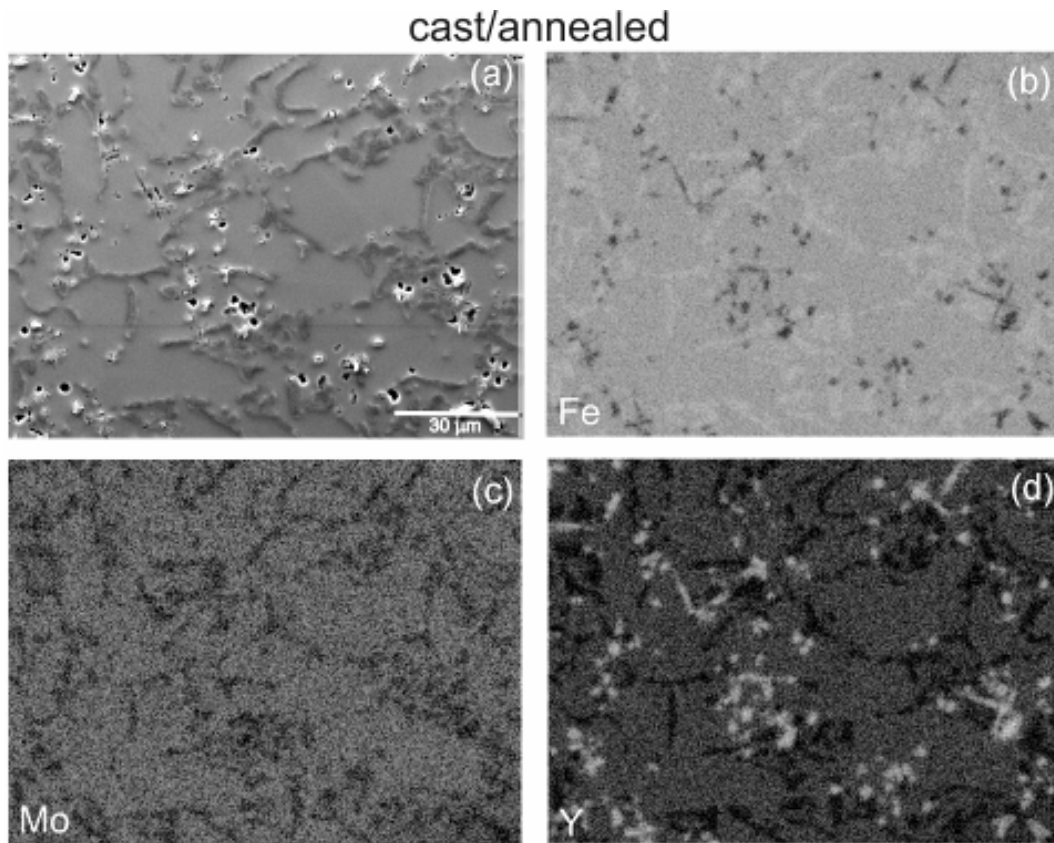
Figure 30 – Y:11Fe:Mo alloy under the cast/annealed condition (slightly etched). (a) Backscattered electron image. Corresponding X-ray maps for Fe (b), Mo (c), Y (d).
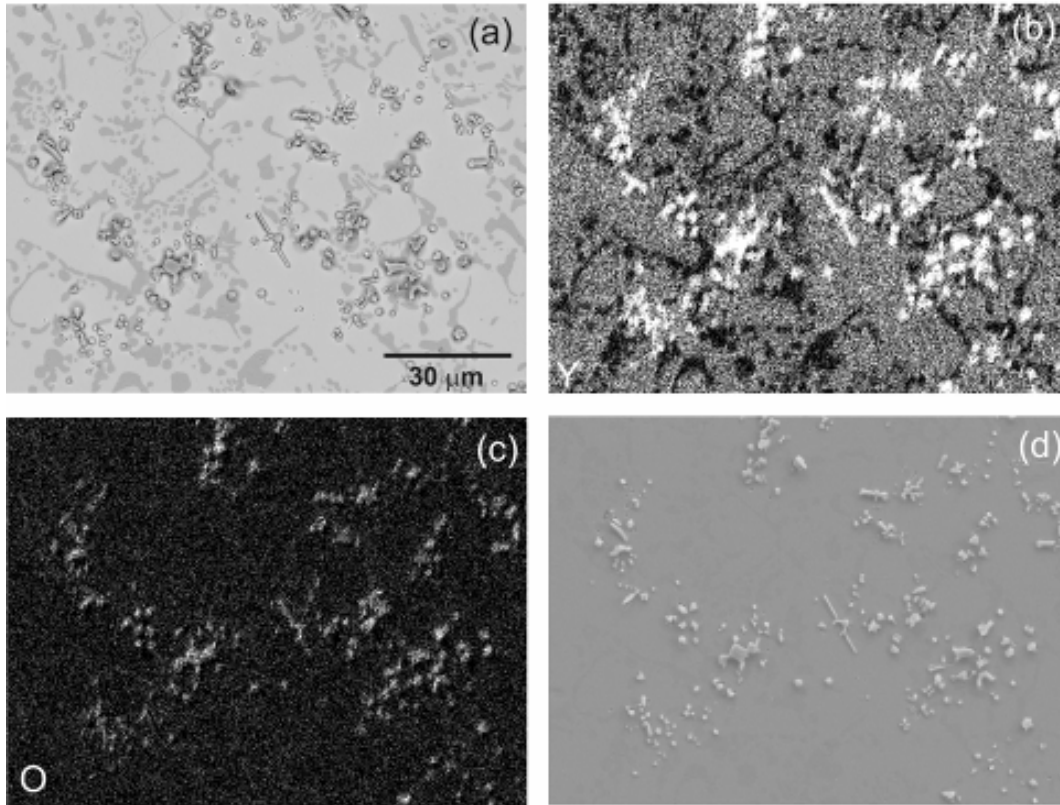
Figure 31 – Y:11Fe:Mo alloy under the cast/annealed condition (non-etched). (a) Backscattered electron image. Corresponding X-ray maps for Y (b), O (c) and secondary electron image (d).
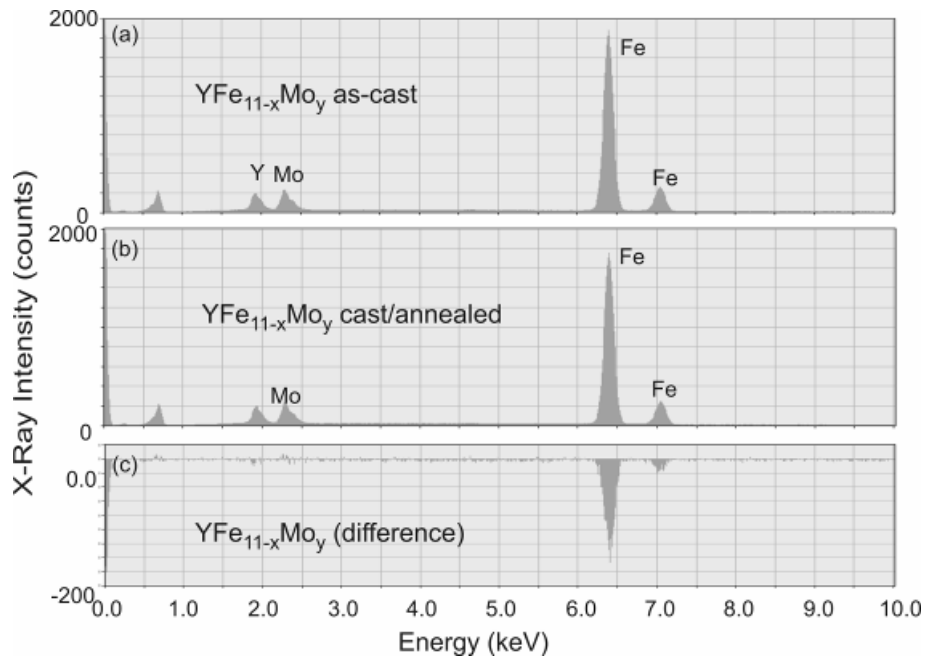

Figure 32 - EDS spectra obtained with Y:11Fe:Mo material. Averaged spectra resulting from 5 point analyses performed on the $YFe_{11-x}Mo_y$ phase under as-cast (a) and cast/annealed (b) conditions. These averaged spectra were normalized by equalizing the Y counts. (c) Difference between the averaged spectra.

Figure 33 shows MFM images of the cast/annealed material. The $YFe_{11-x}Mo_y$ grains exhibit reverse spikes with transverse linear dimensions under 500 nm.
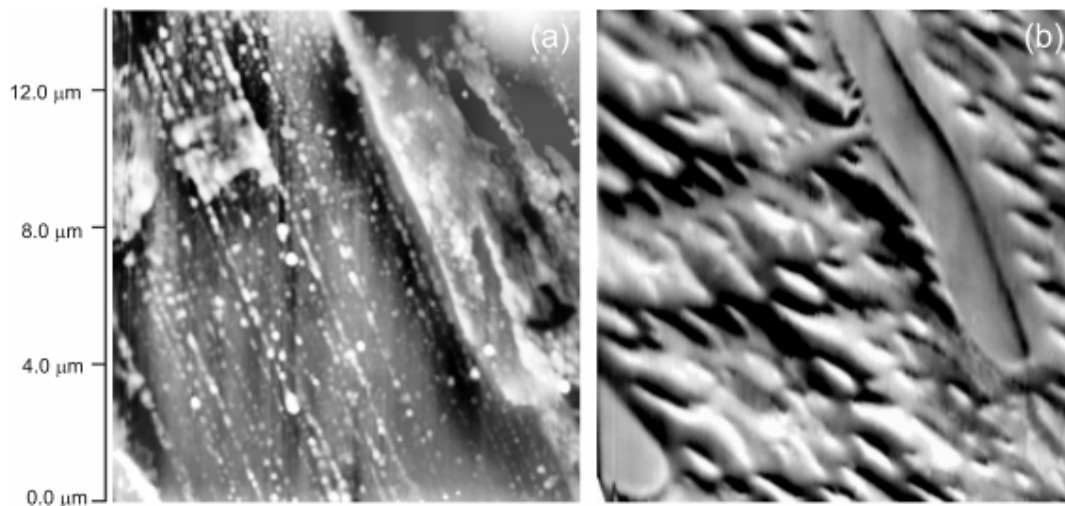
Figure 33 – MFM images of the cast/annealed material. (a) Topographical image (tapping mode) where the bright elevated regions correspond to sample preparation residues. (b) Phase image obtained under lift mode with a magnetized CoCr tip over the same area as (a) where the phase range is 35°.

Splat-quenched and splat/annealed microstructures

The bright-field image and the over and underfocused Fresnel images in Figure 34 present the typical microstructure and magnetic domain configuration of the splat-quenched Y:11Fe:Mo material under thin film form. Only α-Fe(Mo) and $YFe_{11-x}Mo_y$ phases have been detected by EDS point analysis. The grain sizes of α-Fe(Mo) lied typically within 100 to 500 nm and the ones of $YFe_{11-x}Mo_x$ within 500 to 2000 nm. Large $YFe_{11-x}Mo_y$ grains displayed internal domain walls following stripe/maze patterns characteristic of high anisotropy thin films, with 50-200 nm widths (see Figure 34 (b) and (c)). Vortex domains were common in α-Fe(Mo) (see arrows in Figure 34). Figure 35 evidences domain wall continuity across a $YFe_{11-x}Mo_y$ grain boundary in the splat-quenched Y:11Fe:Mo material.
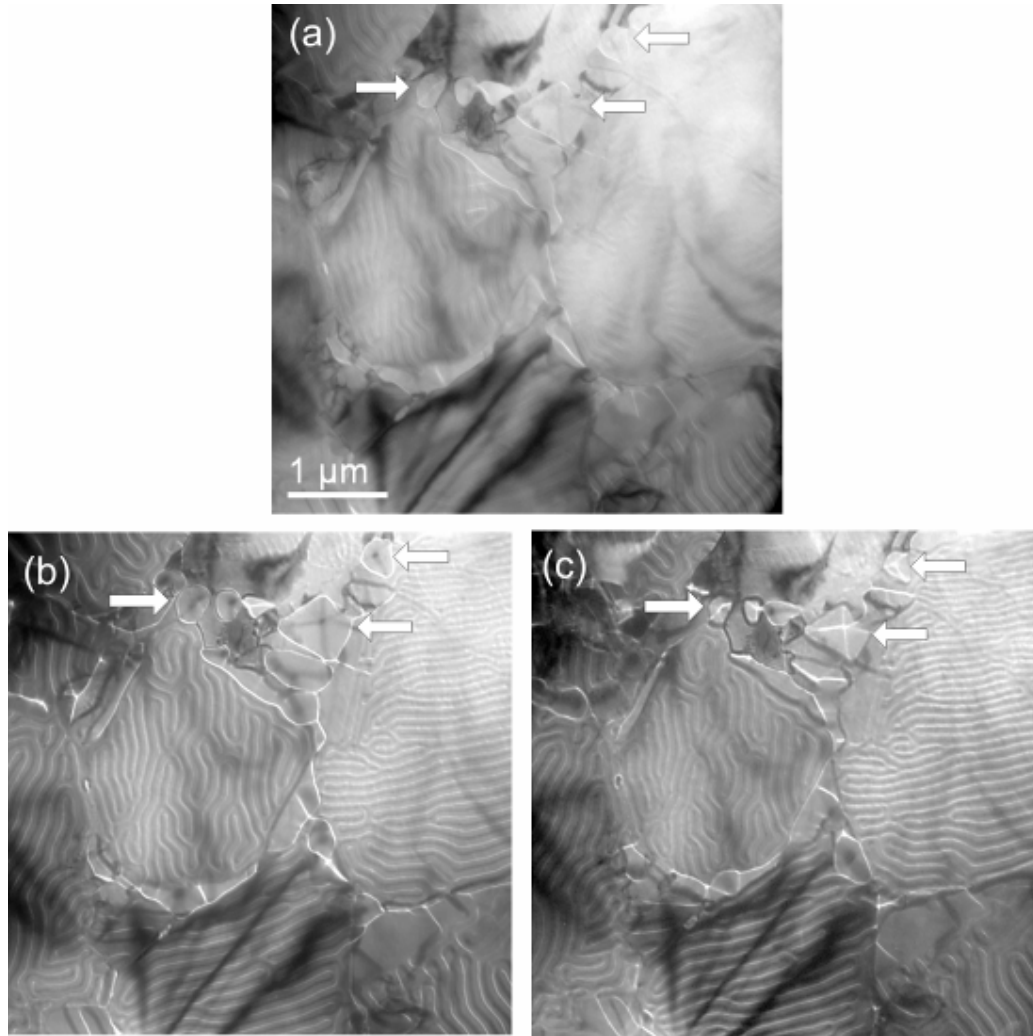
Figure 34 – Microstructure and domain configuration of the Y:11Fe:Mo splat-quenched material. (a) nearly in focus: $\Delta f = 0$ mm, (b) overfocused: $\Delta f = +114$ mm, (c) underfocused: $\Delta f = -176$ mm. The dark contrast at the bottom grain results from bending contours.
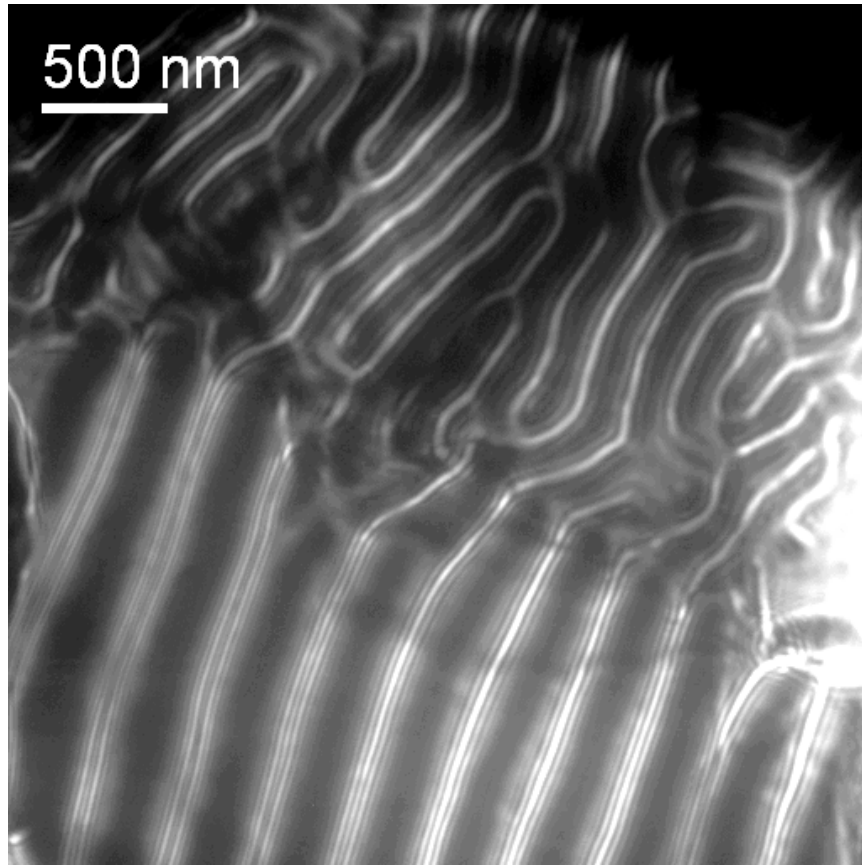
Figure 35 – Domain wall branching at a grain boundary in the Y:11Fe:Mo splat-quenched material (overfocused image). The sets of electron diffraction fringes running parallel to the wall result from the high coherency of the beam.

Figure 36 presents the typical microstructure and magnetic domain configuration of the splat/annealed Y:11Fe:Mo material under thin film form. The annealing treatment has not induced significant changes either in the grain size or magnetic domain arrangement of the $YFe_{11-x}Mo_y$ phase (compare with Figure 34), which continues to display domain walls following stripe/maze patterns characteristic of high anisotropy thin films with widths in the 50 to 200 nm range. Although some coarsening of the α-Fe(Mo) phase could be detected, the approximately constant scale of the microstructure shows that the material presents a remarkable thermal stability.
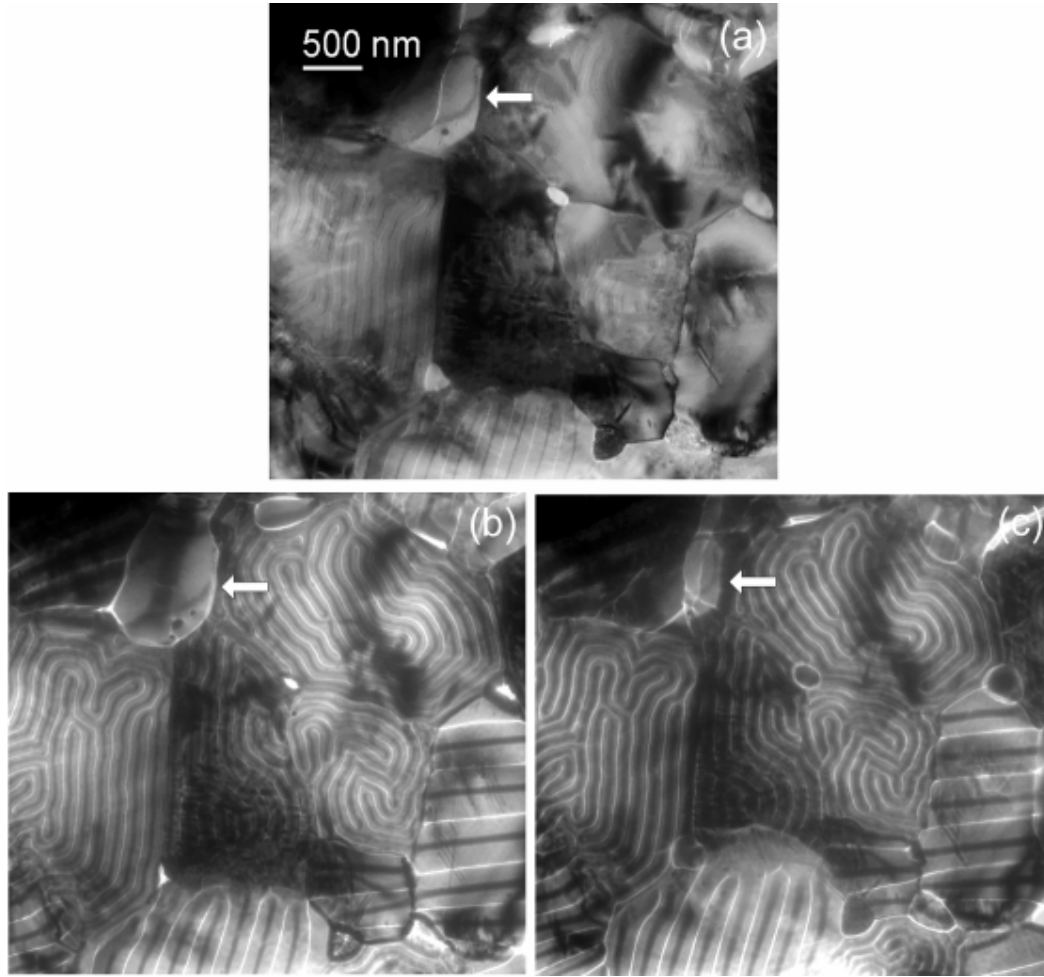
Figure 36 – Microstructure and domain configuration of the Y:11Fe:Mo splat/annealed material, (a) in focus: $\Delta f = 0$ mm, (b) overfocused: $\Delta f = +196$ mm, and (c) underfocused: $\Delta f = -208$ mm.

Averaged EDS spectra obtained at $YFe_{11-x}Mo_y$ splat-quenched and splat/annealed grains are presented, respectively, in Figure 37 (a) and (b). Figure 37 (c) presents the difference between the averaged $YFe_{11-x}Mo_y$ spectra. The EDS results show that a strong Fe segregation from the $ThMn_{12}$-type phase occurred during annealing, with a corresponding iron enrichment of the α-Fe(Mo). This justifies the peak shift and the lattice parameter reduction observed for this phase, which however were not accompanied by comparable (but opposite) variations for the $YFe_{11-x}Mo_y$ phase.

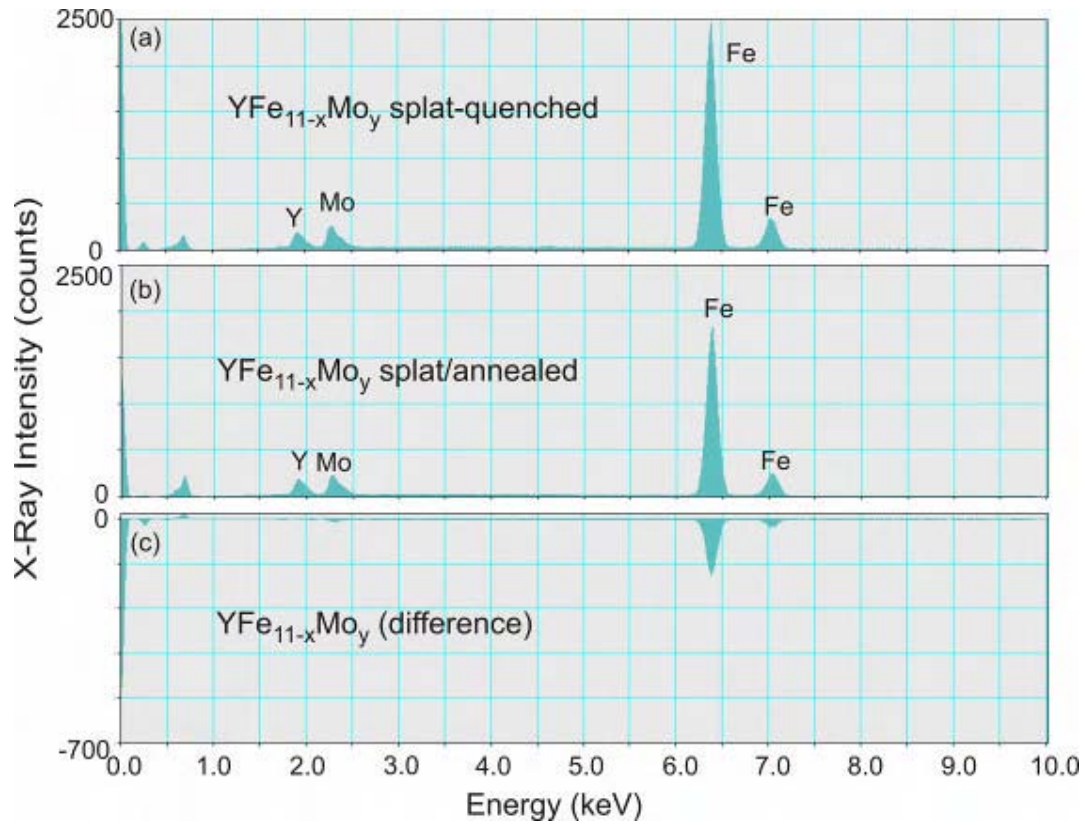Figure 37 – Typical EDS spectra obtained with the Y:11Fe:Mo splat-quenched material at an $YFe_{11-x}Mo_y$ grain(a), and at an α–Fe(Mo) grain (b). The Cu peak originates from specimen supporting copper rings. (c) Difference between 5 averaged spectra obtained at $YFe_{11-x}Mo_y$ splat/annealed grains and 5 averaged spectra obtained at $YFe_{11-x}Mo_y$ splat-quenched grains. The averaged spectra were normalized by equalizing the Y counts.

Figures 38 and 39 present typical MFM results obtained, respectively, at the surfaces of bulk splat-quenched and splat/annealed Y:11Fe:Mo materials. The domain contrast in the phase images showed no correlation with the surface topography and, moreover, no phase contrast difference was detected after changing scan direction. Domain configurations and their scales are analogous in both situations. The magnetic microstructure shows that the $YFe_{11-x}Mo_y$ phase under bulk form, produced by splat-quenching/annealing, displays stripe/maze domain configurations with widths typically bellow 300 nm. The scale of the domain configurations is comparable to the scan height (60 nm) justifying the observed domain (and not wall) contrast.
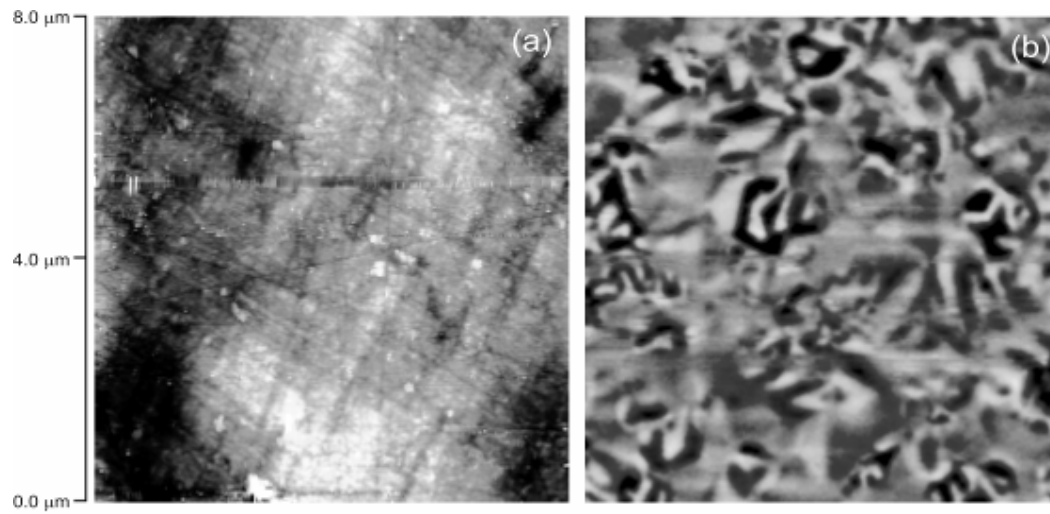
Figure 38 – MFM images of the splat-quenched material surface. (a) Topographical image (tapping mode) where the bright elevated region is foreign matter, (b) phase image obtained under lift mode with a magnetized CoCr tip over the same area as (a) where the phase range is 53°.
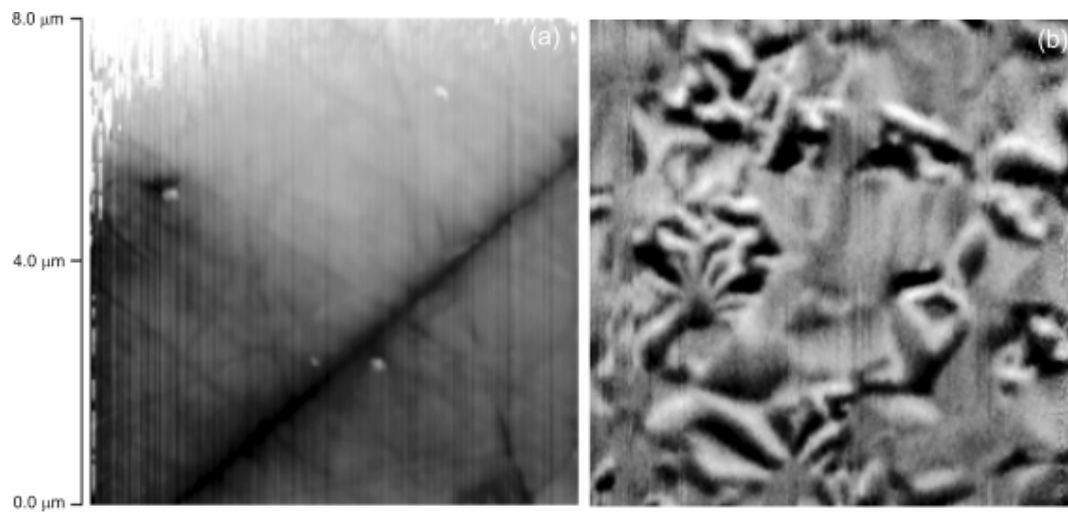

Figure 39 - MFM images of the splat/annealed material surface. (a) Topographical image (tapping mode), (b) phase image obtained under lift mode with a magnetized CoCr tip over the same area as (a) where the phase range is 34°.

Magnetization measurements

Magnetization curves at room temperature obtained with the splat-quenched and splat/annealed materials are presented in Figure 40. The smooth appearance indicates that both magnetic phases, $YFe_{11-x}Mo_y$ and $\alpha-Fe(Mo)$, exhibit similar magnetization behavior with combined saturation magnetization (M_s) at 5 Tesla of 18.1 μ_B/fu and 18.0 μ_B/fu for the splat-quenched and splat-annealed conditions, respectively.
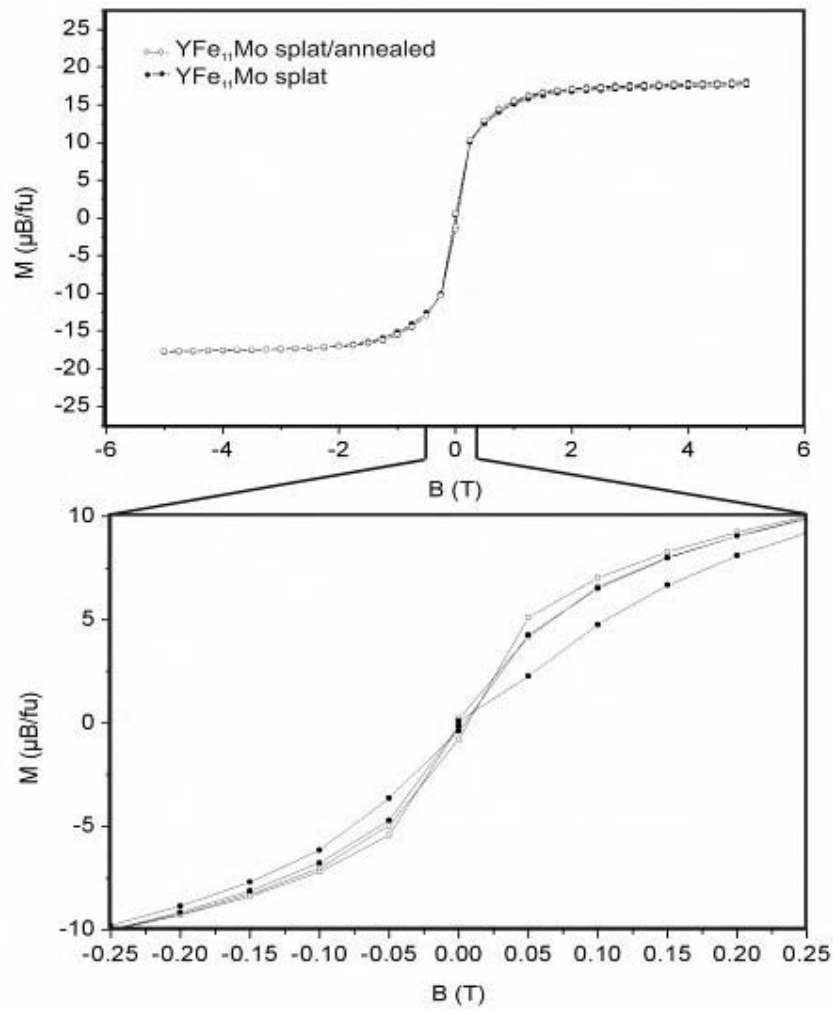

Figure 40 – Magnetic field dependence of the magnetization at 298 K for the splat-quenched and splat-annealed materials.

4.4. Discussion

Structural Stability

The microstructure morphologies and EDS results show that the primary crystallization phase in the Y:11Fe:Mo alloy is the $ThMn_{12}$-type $YFe_{11-x}Mo_y$ compound. As with Y:11Fe:Ti, the presence of α-Fe(Mo) could not be suppressed during any of the processing routes and no other phases, derived from $CaCu_5$, could not detected.

The presence of α-Fe(Mo) demonstrates active solute partition between the liquid and solid phases during both solidification processes. However, contrarily to the Y:11Fe:Ti case, the slightly lower α-Fe(Mo) volume fraction for the splat material indicates that splat-quenching established more stringent conditions for segregation than arc melting (compare the splat-quenched and as-cast materials diffractograms in Figure 28 and Figure 16). In the literature, α-Fe(Mo) has been also been reported in a series of R:11Fe:Mo alloys (with R = Y, Ho) prepared by melting in a crucible induction at temperatures around 900°C [82].

The high α-Fe(Mo) peak intensity after annealing at 800 and 950 °C reveals that the equilibrium iron content of the $ThMn_{12}$-type structure at these temperatures is considerably lower than stipulated by the $RFe_{11}M$ stoichiometry. The EDS results in Figures 29 to 32 show that the as-cast material underwent a $ThMn_{12}$-type $\rightarrow$ $ThMn_{12}$-type + α-Fe(Mo) + Y transformation during annealing at 950 °C, evidenced by Y precipitation and Fe segregation. In the case of the splat-quenched material, Figure 36 shows that Fe was also strongly segregated from the $YFe_{11-x}Mo_y$ during annealing at 800 °C. A comparison between the α-Fe(Mo) peaks under the cast/annealed vs splat/annealed conditions indicate a higher proportion for the latter material, which corresponds to a lower iron content in the $YFe_{11-x}Mo_y$ phase, in agreement with the EDS results. Nevertheless, in spite of the differences in Fe and Mo contents in the $ThMn_{12}$-type phase, only limited variations in the lattice parameters could be detected for the conditions studied (see legend in Figure 28).

The iron segregation in the studied conditions point to a homogeneity range such as the ones reported for Nd-Fe-Mo [65], and Gd-Fe-Mo [68] systems. This behavior has been proposed to result from the presence of structural point defects involving partial substitution of Fe/M by rare-earth atoms at the *8i* sites and from the presence of Fe vacancies at the *8f* and *8j* sites [48]. However, in view of the Y-Y and Y-Fe/Mo interatomic distances (determined from the structure simulated with PowderCell: ~4.8 Å and ~3.0 Å, respectively), and considering the difference in metallic radius (1.26 Å for Fe, 139 Å for Mo and 1.81 Å for Y, for a coordination number of 12 [69]) and (iii) taking into account the limited lattice parameter variations observed for the $ThMn_{12}$-type phase, vacancies are more likely to be occurring.

Magnetic microstructure

The reverse spikes observed in the as-cast $YFe_{11-x}Mo_y$ grains (Figure 32) result from fine domain branching at the surface due to minimization of closure energy [63]. This undulation of the main domains in maze structures near the surface of bulk samples has origin in the reduction of magnetostatic energy at the cost of a larger total Bloch wall area [72].

Contrarily to the Y:11Fe:Ti alloy, the necessary small grain sizes for single domain behaviour have not been attained by splat-quenching. The images presented in Figures 34 to 36, 38 and 39 show that the microstructures and domain configurations are analogous under splat and splat/annealed conditions for both thin film and bulk form. Under both conditions, grain boundaries were usually associated with domain walls and large $YFe_{11-x}Mo_y$ crystallites presented stripe/maze domain configurations characteristic of high-anisotropy materials; however, as with the Y:11Fe:Ti material, vortex domains in α-(Fe,Mo) grains have been observed in thin films and are expected to result from accommodation to the demagnetizing fields of neighbouring $YFe_{11-x}Mo_y$ grains.

The domain wall continuity across a grain boundary in Figure 35 shows that the two grains are magnetized parallel, i.e., exchanged coupled, although the domain configurations indicate different crystallographic orientations. The maze configuration at the top grain points to an orientation close to the [0001] zone axis, the easy magnetization direction, whereas the parallel configuration at the bottom grain points to an

in-plane magnetization. The difference in domain width reflects the magnetic anisotropy, which is accommodated at the grain boundary by domain branching.

The materials show no coercivity indicating high domain mobility and a reduced pinning effect of grain boundaries. The fact that the saturation magnetization and the anisotropy constant of $YFe_{11}Mo$ at 273 K could not be found in the literature, hindered the estimation of the domain wall energy using Kittel's model [74,75] with basis on parallel domain widths. Nevertheless, the typically larger domain widths observed in $YFe_{11-x}Mo_y$ as compared with $YFe_{11-xT}Ti_y$ suggest higher domain wall energy.

4.5. Summary

- The as-cast and splat-quenched materials crystallized essentially adopting the $ThMn_{12}$-type structure, though the $RFe_{11}M$ stoichiometry was not strictly followed. The occurrence of other phases derived from $CaCu_5$ could not be detected.
- In spite of significant differences in iron segregation, only limited variations in the lattice parameters could be detected for $YFe_{11-x}Mo_y$ under the conditions studied.
- The homogeneity range with lattice parameter evolution supports the hypothesis of Fe vacancies in the $ThMn_{12}$-type structure and suggests that the fraction of structural point defects adapt to the annealing temperature.
- Similar domain configurations were observed for both the splat-quenched and splat/annealed conditions. Grain boundaries were usually associated with domain walls and large $YFe_{11-x}Mo_y$ crystallites presented stripe/maze domain configurations characteristic of high-anisotropy materials, with widths of 50-200 nm. However, vortex domains in α-Fe(Mo) grains appear to be a thin film feature and are expected to result from accommodation to the demagnetizing fields of neighbouring $YFe_{11-x}Mo_y$ grains.
- The materials show no coercivity indicating high domain mobility and a reduced pinning effect of grain boundaries.

5. Nd-Fe-Ti system (Nd:11Fe:Ti alloy)

5.1. Introduction

Among the iron-based $ThMn_{12}$-type systems, the $NdFe_{11}Ti$ compound has been extensively investigated [9,30-35]. In this compound, the rare-earth (4f) sublattice presents planar anisotropy, whereas the Fe (3d) sublattice presents uniaxial anisotropy. The competitive anisotropy contributions from the two sublattices lead to spin reorientation as the temperatures changes, and a conversion in magnetocrystalline anisotropy from planar to uniaxial due to a second-order crystal-field parameter change from negative to positive [31]. At room temperature $NdFe_{11}Ti$ has a negative anisotropy constant, which results in planar anisotropy [32]. Regarding the stability of the $ThMn_{12}$-type phase, Jang and Stadelmaier proposed that the $NdFe_{11}Ti$ compound is unstable at temperatures below 1000 °C, decomposing by a solid-state reaction into $Nd_2(Fe,Ti)_{17}$ (with a rhombohedral Th_2Zn_{17}-type structure), Fe_2Ti and α-Fe(Ti) [66].

In spite of the vast number of fundamental studies on the magnetic behavior of $NdFe_{11}Ti$ compounds, only limited studies have been reported on magnetic domain configuration [46] and scarce microstructural characterization has been performed on these materials [47,48].

5.2. Experimental details

Alloys preparation and heat treatments

The alloys were prepared by melting the elements with ≥99.9 % purity in an arc furnace, under argon atmosphere and on a water-cooled crucible. In order to increase homogeneity, the samples were melted at least three times (as-cast condition). The weighted elemental quantities corresponding to the $NdFe_{11}Ti$ stoichiometry were 1.3355 mg for iron, 0.3135 mg for neodymium and 0.1046 mg for titanium, with a mass loss after fusion of ~0.1 %.

Part of the as-cast material was subsequently sealed in evacuated quartz tubes and annealed at 950 °C for 1536 h (cast/annealed condition). Another portion of the as-cast material was remolten and splat-quenched by cooling down a droplet of the prepared alloy between two copper pistons shot against each other at ~9 ms^{-1}. A cooling rate of ~10^6 Ks^{-1} is obtained by this method and the resulting disks have a diameter of ~20 mm and a thickness of ~100 μm (splat condition). A fraction of the splat-quenched material was subsequently sealed in evacuated quartz tubes and annealed at 800 °C for 1289 h (splat/annealed condition).

X-ray powder diffractograms

X-ray powder diffractograms of the materials have been obtained at room temperature using a Panalytical X'Pert Pro powder diffractometer. Samples were crushed down to a fine powder and deposited onto a low noise (single crystalline Si) sample holder. The data acquisition was made with a 2θ - step size of 0.03°. The software package PowderCell [57] was used to simulate diffractograms for comparison with experimental data. An NdFe$_{11}$Ti unit cell with ThMn$_{12}$-type of structure was built based on the crystallographic information listed in [58], and by assuming that 75% of the *8i* positions were occupied by Fe and 25% by Ti, and using the lattice parameters reported in [9]. Cells of the Th$_2$Zn$_{17}$ type and Th$_2$Ni$_{17}$ type were built based on the crystallographic information and lattice parameters reported in [60], assuming an Nd$_2$Fe$_{17}$ stoichiometry. A cell for Nd$_3$(Fe,Ti)$_{29}$-type structure has also been built considering the *A2/m* space group with base on the crystallographic information listed in [61] and using the lattice parameters presented in [62]. This phase has a composition close to the one corresponding to the ThMn$_{12}$-type phase and a structure derived as well from CaCu$_5$ [64].

SEM

For scanning electron microscopy sample preparation involved grinding with silicon carbide paper and consecutive polishing with 6, 3 and 1 μm diamond suspensions. Final polishing and light etching were obtained with a commercial alumina suspension in an acid solution (OPS-Struers). The observations have been performed with a Hitachi S2400 and JEOL 7001F instruments equipped for energy dispersive X-ray spectrometry after further etching with an aqueous solution of HF, HCl and HNO$_3$.

AFM and MFM

Sample preparation for atomic and magnetic force microscopy involved the metallographic steps described above plus final polishing with a 0.1 µm diamond suspension. The observations have been performed with a Veeco di CP-II atomic force microscope using commercially available MFM cantilevers (MESP-CPMT) with nominal length of 225 µm and nominal spring constant of 2.8 N/m. The MESP-CPMT tips are coated by a CoCr alloy and have a nominal curvature radius of 25 nm. The tips are magnetized along their axis and have a coercivity of ~400 Oe. In lift mode the tip-sample separation (Z) was kept around 60 nm. MFM observations have been carried out under dynamic conditions using a sequential two-scan method.

TEM

For transmission electron microscopy, sample preparation involved cutting a disc with a diameter of 3 millimetres, and grinding until a thickness around 80 micrometers was reached. The samples were thinned to electron transparency by argon ion milling using a Gatan-Duo Mill machine, operating at an accelerated voltage of 4 kV, with a 14° incident angle. TEM observations have been performed at a Hitachi H8100 microscope, equipped for energy dispersive X-ray spectroscopy.

Magnetization isotherm cycles

Magnetization isotherm cycles at room temperature were performed using a multipurpose characterization system *MagLab* 2000 (Oxford Instruments) with magnetic fields up to 5 T. Crushed powder particles of the splat-quenched and splat/annealed materials were fixed under random orientation with acetone soluble glue, which prevented rotation of individual particles under the applied magnetic field.

5.3. Results

X- Ray Diffraction

Figure 41 presents experimental X-ray diffractograms of the Nd:11Fe:Ti alloy obtained for the as-cast, splat-quenched and annealed conditions, along with simulations for the $ThMn_{12}$ structure and other related structures. The results indicate that both the as-cast and splat-quenched materials crystallized adopting essentially the $ThMn_{12}$-type structure. Nevertheless, the peaks at 36.5° and 47.5° in the as-cast condition, as well as in the cast/annealed and splat/annealed conditions suggest the presence of the Th_2Zn_{17}-type phase (the literature parameters for the Th_2Zn_{17}-type phase resulted in a slight shift to the right of the simulated diffraction pattern when compared with the experimental results). The peak at 44.5° demonstrates that α-Fe(Ti) is present in all conditions. The peaks at 40.9° and 45.3° indicate the presence of Fe_2Ti. The proportion of α-Fe(Ti) in the as-cast material remained approximately constant after annealing at 950 °C, whereas for the splat condition annealing at 800 °C induced a strong increase of its volume fraction. As the R:11Fe:M stoichiometry is probably not followed, the $ThMn_{12}$-type phase will be hereafter denominated $NdFe_{11-x}Ti_y$, where x and y are variables that depend on the material condition. The lattice parameters of the this phase in all the studied conditions (legends in Figure 40) are in fair agreement with the ones reported for $NdFe_{11}Ti$ [1,83,84]. The α-Fe(Ti) lattice parameter was $a_{cast} = 0.288$ nm for the as-cast condition and $a_{splat} = 0.288$ nm for the splat condition, the annealing treatments induced lattice parameter decreases of $\left(a_{cast/annealed} - a_{cast} \right) / a_{cast}$ = ~0.0 % and $\left(a_{splat/annealed} - a_{splat} \right) / a_{splat}$ = -0.3 %, respectively.
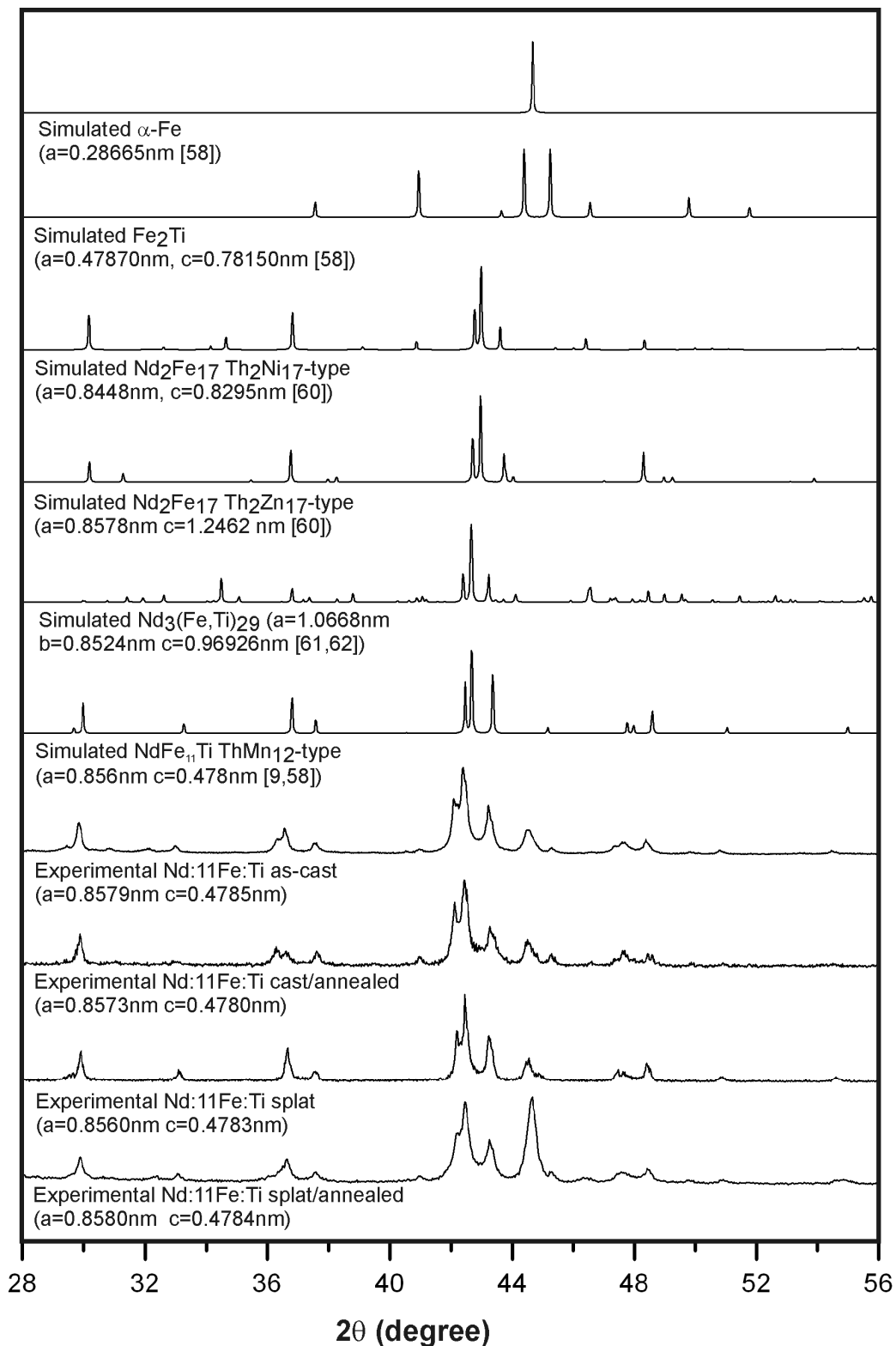
Figure 41 – Experimental X-ray diffractograms for the Nd:11Fe:Ti alloy under as-cast, cast/annealed, splat and splat/annealed conditions (simulations for α-Fe, NdFe$_{11}$Ti (ThMn$_{12}$-type), Nd$_2$Fe$_{17}$ (Th$_2$Zn$_{17}$ and Th$_2$Ni$_{17}$-types) and Nd$_3$(Fe,Ti)$_{29}$-type are included. Lattice parameters, determined assuming a stoichiometric NdFe$_{11}$Ti structure, are indicated above each experimental diffractogram.

Figure 42 presents an image of the typical microstructure of the as-cast material obtained by SEM, and corresponding EDS maps. As expected from the XRD results, the predominant phase in the as-cast microstructure is the $ThMn_{12}$-type $NdFe_{11-x}Ti_y$. However, another rare-earth phase, with slightly higher Nd and lower Ti contents, is also present. According to the XRD results this phase corresponds to $ThZn_{17}$-type $Nd_2(Fe,Ti)_{17-w}$. Coarse α-Fe(Ti) regions with a dendritic morphology, Nd-rich patches (bright regions in the BSE image), Fe_2Ti and Ti-rich cuboids (that may correspond to Ti oxide) were also found in the microstructure. The observations demonstrated that the solidification sequence for the major phases is: α-Fe(Ti) $\rightarrow$ $NdFe_{11-x}Ti_y$ $\rightarrow$ $Nd_2(Fe,Ti)_{17-w}$. These results show that the high temperature rare-earth phase is $NdFe_{11-x}Ti_y$ and that the surrounding $Nd_2(Fe,Ti)_{17-w}$ phase is formed by a L + $ThMn_{12}$-type $\rightarrow$ $ThZn_{17}$-type peritectic reaction. The role of the Nd-rich phase is not clear and it is likely that this phase participates in the peritectic reaction, either as a reactant or as a reaction product. Figure 43 shows averaged and normalized EDS spectra obtained at $NdFe_{11-x}Ti_y$ and at $Nd_2(Fe,Ti)_{17-w}$ grains as well as their difference.

The microstructure of the cast/annealed condition, shown in Figure 44, evidences a significant evolution: there has been a consumption of $NdFe_{11-x}Ti_y$ and an enhancement of the $Nd_2(Fe,Ti)_{17-w}$ volume fraction (brighter regions), as well as an increase of Fe_2Ti presence, which precipitated at the interfaces between the rare-earth compounds and α-Fe(Ti). Consequently, the heat-treatment induced a $ThMn_{12}$-type $\rightarrow$ $ThZn_{17}$-type + α-Fe(Ti) solid state transformation. No Nd-rich patches were found in the microstructure after the heat treatment and this phase may have been consumed in the solid state reaction. Figure 45 shows averaged and normalized EDS spectra obtained at $NdFe_{11-x}Ti_y$ and at $Nd_2(Fe,Ti)_{17-w}$ grains as well as their difference. The EDS analyses show that, contrarily to the other compounds studied, in the present case the $ThMn_{12}$-type phase incorporated some iron and rejected titanium during the heat treatment (Figure 45 (d)). On the other hand, the $Nd_2(Fe,Ti)_{17-w}$ phase is poorer than $NdFe_{11-x}Ti_y$ in both Fe and Ti,. and its presence is responsible for the increased volume fraction of α-Fe(Ti) in the annealed microstructure (see Figure 44 (a) .

as-cast

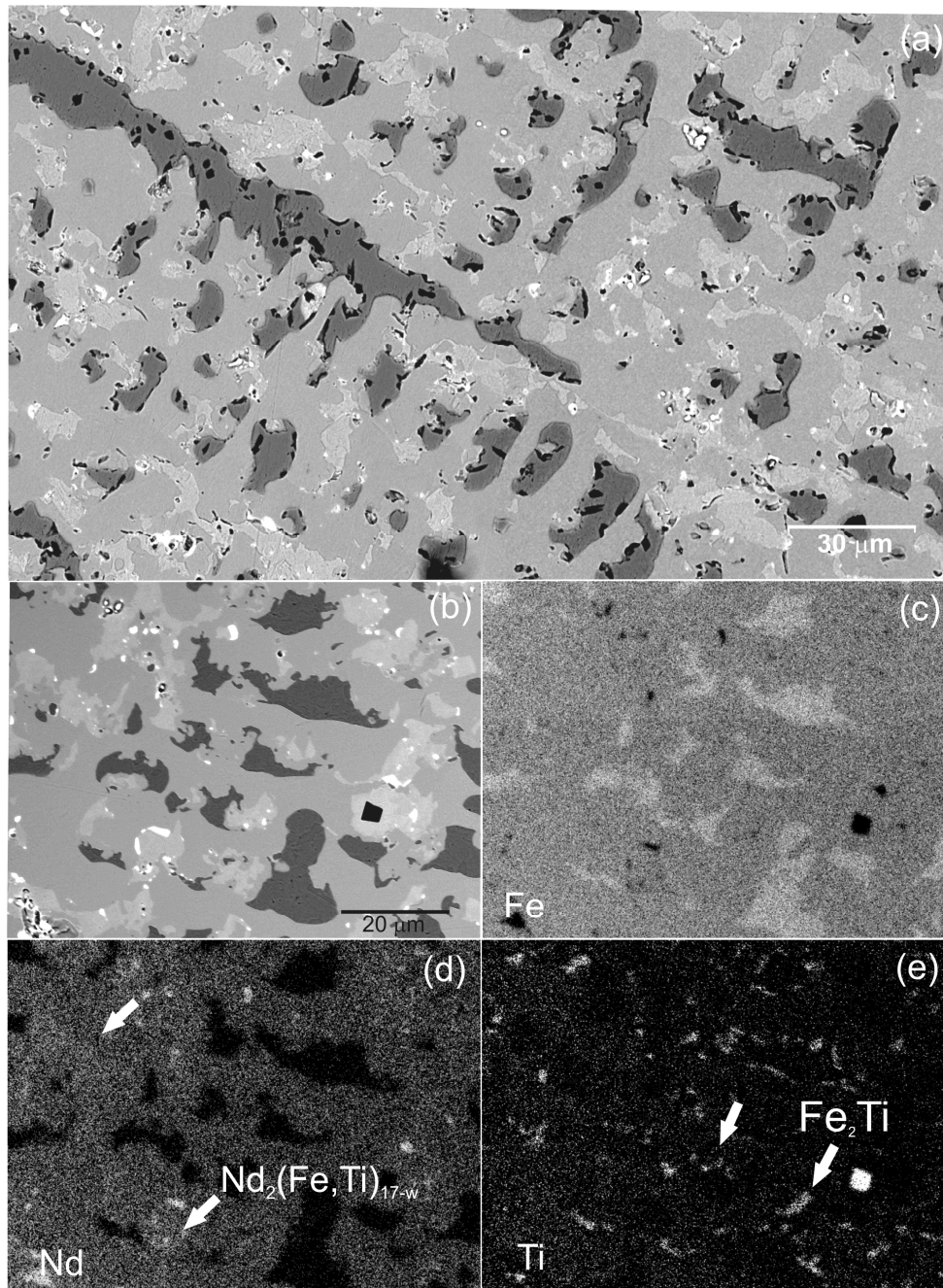
Figure 42 – (a) Backscattered electron image of the etched as-cast microstructure of the Nd:11Fe:Ti alloy showing the dendritic morphology of the α–Fe(Ti) phase. (b) Backscattered electron image of the etched as-cast microstructure corresponding to the X-ray maps for Fe (c), Nd (d) and Ti (e). These results show the presence of two rare-earth compounds, α-Fe(Ti), Fe_2Ti and scattered titanium-rich cuboids.
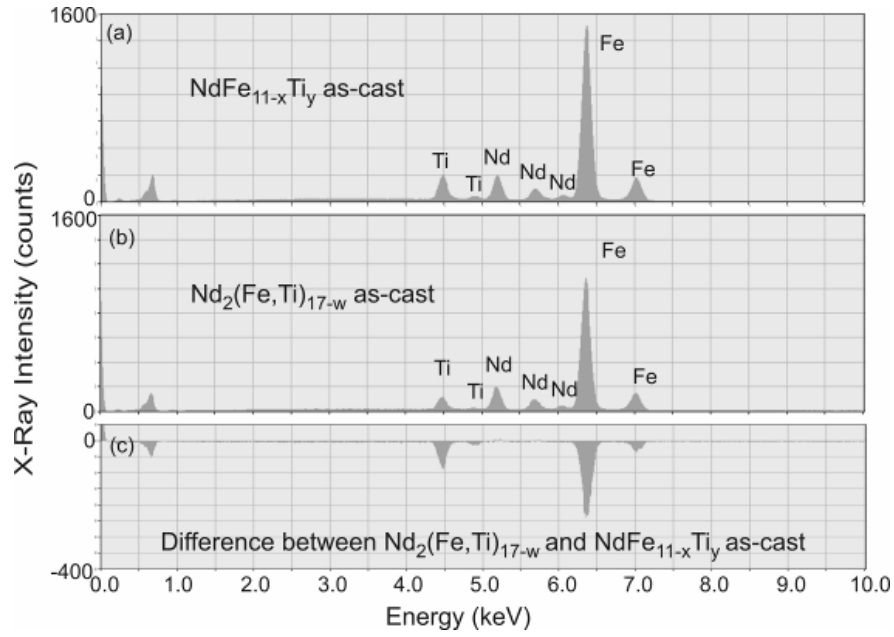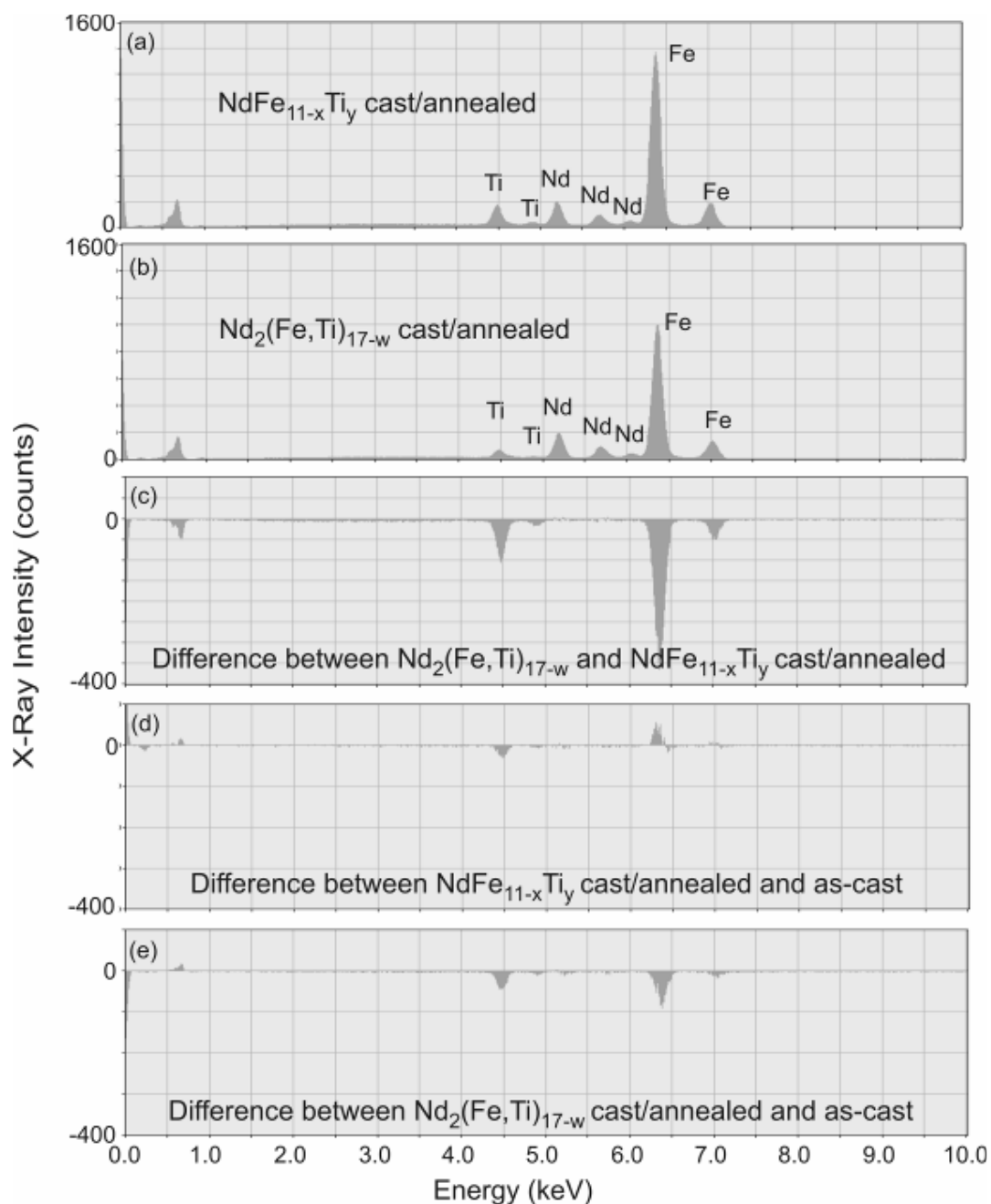
Figure 43 - EDS spectra obtained with Nd:11Fe:Ti material under the as-cast condition . Averaged spectra resulting from 5 point analyses performed on the $NdFe_{11-x}Ti_y$ (a) and on the $Nd_2(Fe,Ti)_{17-w}$ (b) phases. These averaged spectra were normalized by equalizing the Nd counts. (c) Difference between the two as-cast phases.
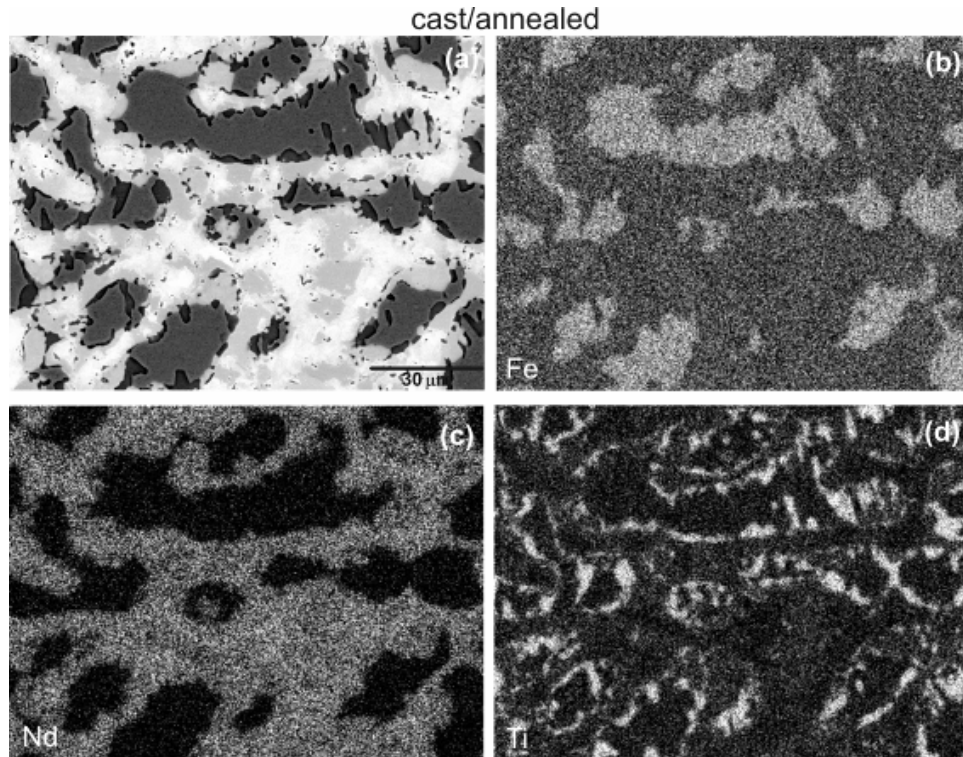
Figure 44 - Backscattered electron images and X-ray maps of the etched annealed Nd:11Fe:Ti alloy. Cast/annealed microstructure (a) and corresponding X-ray maps for Fe (b), Nd (c) and Ti (d), showing α-Fe(Ti) dendrite arms and two rare-earth compounds at the interdendritic regions. The darker rare-earth compound is $ThMn_{12}$-type $NdFe_{11-x}Ti_y$ and the brighter is Th_2Zn_{17}-type $Nd_2(Fe,Ti)_{17-w}$. The presence of Fe_2Ti is clearly evident in the Ti map.

Figure 45 - EDS spectra obtained with Nd:11Fe:Ti material under the cast/annealed condition. Averaged spectra resulting from 5 point analyses performed on the $NdFe_{11-x}Ti_y$ (a) and on the $Nd_2(Fe,Ti)_{17-w}$ (b) phases. These averaged spectra were normalized by equalizing the Nd counts. (c) Difference between the two cast-annealed rare-earth phases. (d) Difference between the cast-annealed and as-cast $NdFe_{11-x}Ti_y$ phase. (d) Difference between the cast-annealed and as-cast $Nd_2(Fe,Ti)_{17-w}$ phase.

Figure 46 shows a typical magnetic microstructure of the cast/annealed material observed by MFM. In this image grains with about 4 μm in size exhibit domains with mixed stripe/maze patterns with linear transverse dimensions under 200 nm, characteristic of magnetocrystalline anisotropic phases. The top left grain presents undulated domains. The striped central grain is surrounded by grains that present branching behaviour near the interface.
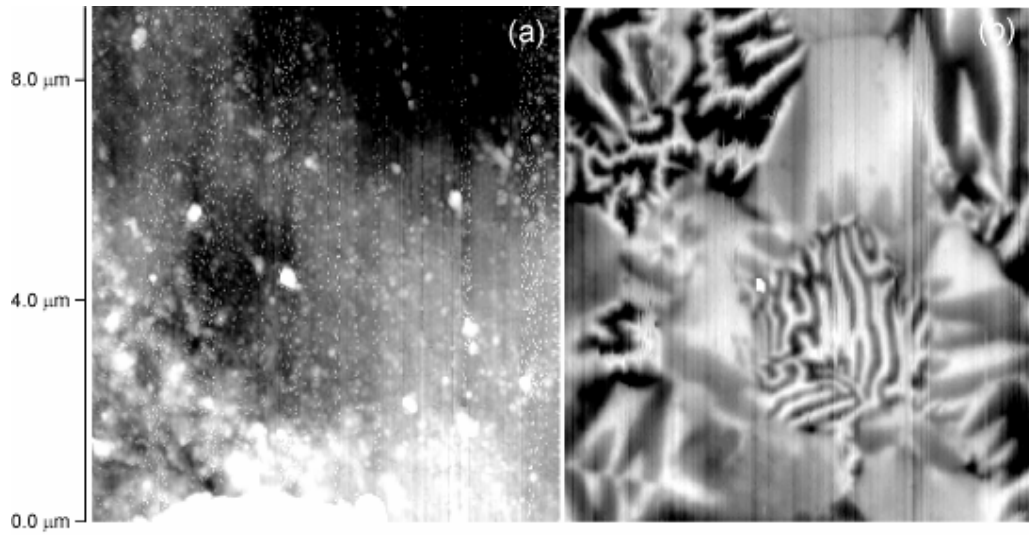

Figure 46 – MFM images of the cast/annealed material etched surface. (a) Topographical image (tapping mode) where the bright elevated regions correspond to residues resulting from sample preparation, (b) phase image obtained under lift mode with a magnetized CoCr tip over the same area as (a) where the phase range is 27°.

Splat-quenched and splat/annealed microstructures

Figure 47 presents the fine microstructure of the splat-quenched Nd:11Fe:Ti material. EDS analyses showed the presence of $NdFe_{11-x}Ti_y$ phase and α-Fe(Ti), while no Fe_2Ti or $Nd_2(Fe,Ti)_{17-w}$ could be detected. These results are in agreement with the XRD results, which indicate the absence of both phases, and demonstrate that the splat-quenched treatment suppresses the appearance of peritectic Th_2Zn_{17} $Nd_2(Fe,Ti)_{17-w}$. The grain size for both α-Fe(Ti) and $NdFe_{11-x}Ti_x$ grains lies typically within 100 to 200 nm.
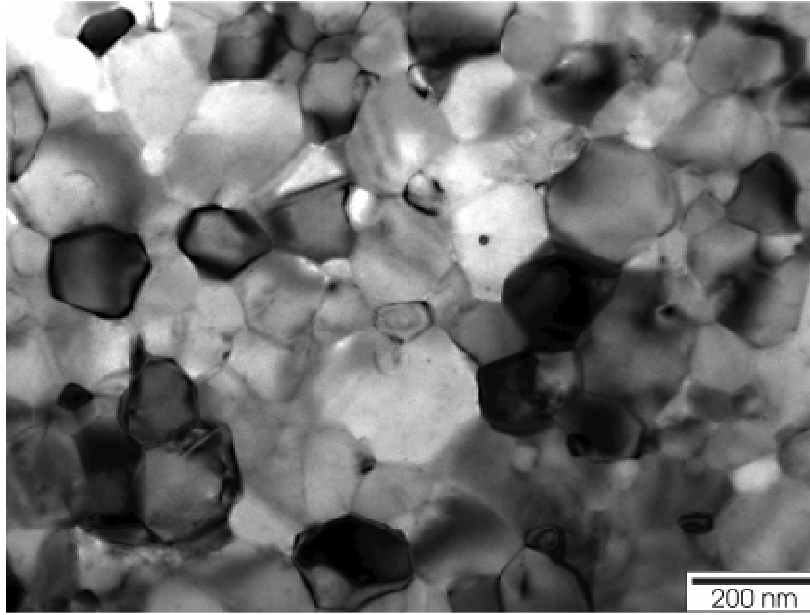
Figure 47 – Microstructure of the Nd:11Fe:Ti splat-quenched material presenting a fine mixture of $NdFe_{11-x}Ti_y$ and α-Fe(Ti) phases.

Figure 48 presents typical MFM results obtained with the Nd:11Fe:Ti splat-quenched material, showing a fine domain configuration in bulk surfaces, in agreement with the fine microstructure, where each crystallite corresponds essentially to a magnetic domain.
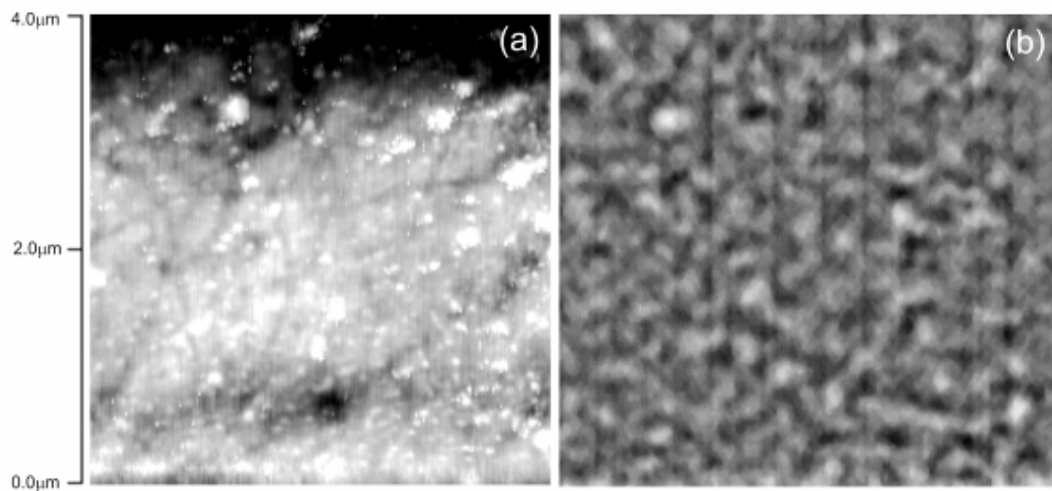

Figure 48- MFM images of the splat-quenched material surface. (a) Topographical image (tapping mode) where the bright elevated regions correspond to residues resulting from sample preparation, (b) phase image obtained under lift mode with a magnetized CoCr tip over the same area as (a) where the phase range is 67°.

Figure 49 presents the typical microstructure of the Nd:11Fe:Ti splat/annealed material. The annealing treatment induced an overall grain growth to the 200-1000 nm range as compared to the 100-200 nm observed for the splat-quenched condition. EDS analyses showed the presence of α-Fe(Ti), Fe_2Ti, $NdFe_{11-x}Ti_y$ and another rare-earth phase with slightly higher Nd and lower Ti contents, exhibiting a random distribution of planar defects (Figure 50).
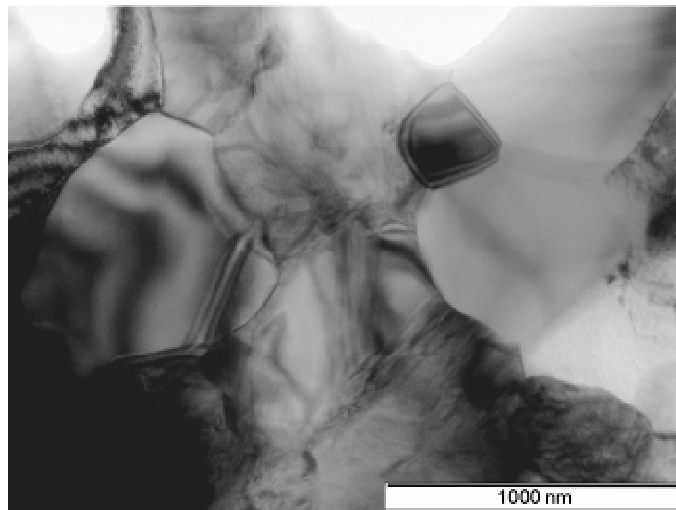

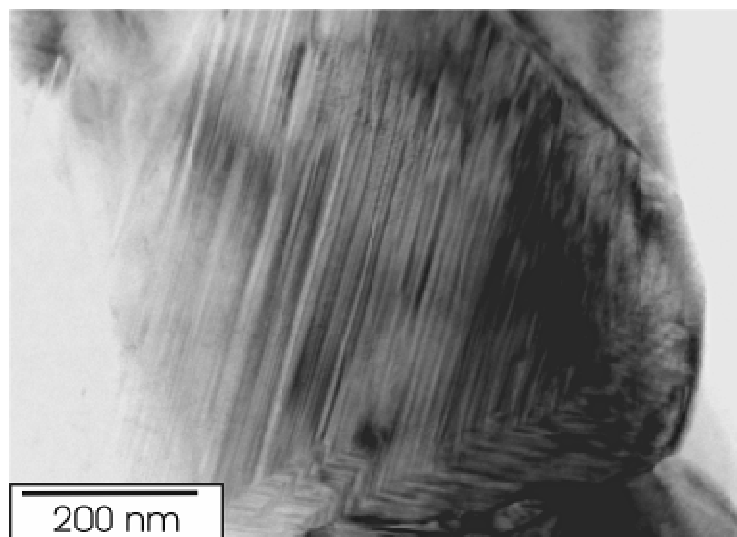Figure 49 – (a) Microstructure of the Nd:11Fe:Ti splat/annealed material.

Figure 50 - (a) Randomly distributed planar defects in a rare-earth compound grain.

Figure 51 shows average EDS spectra obtained at $ThMn_{12}$-type $NdFe_{11-x}Ti_y$ grains under the splat-quenched (a) and splat/annealed (b) conditions, as well as their composition difference. Figure 52 presents EDS results obtained at grains exhibiting a random distribution of planar defects.
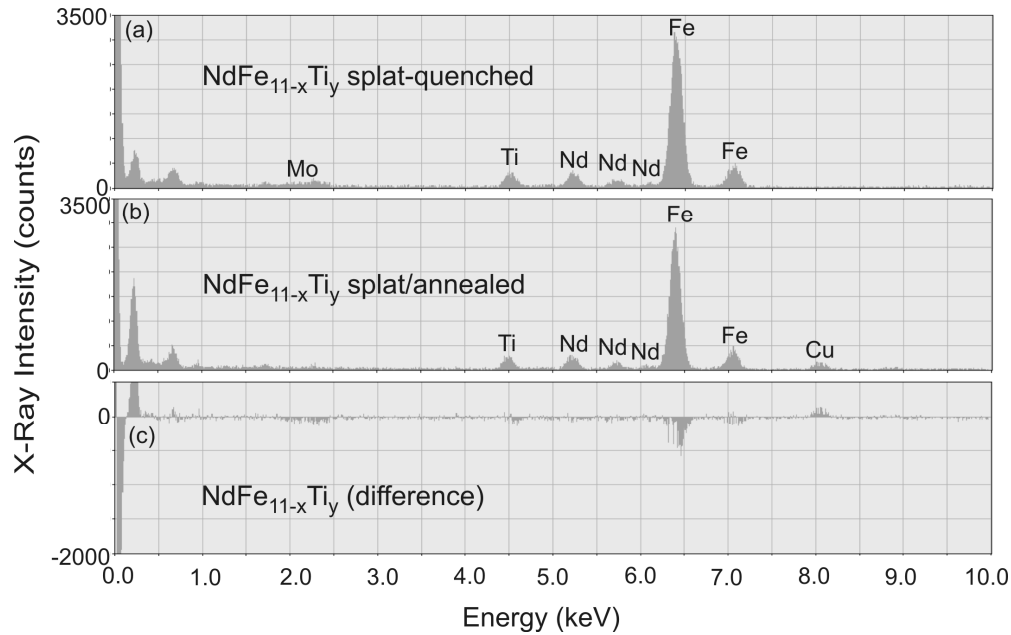

Figure 51 - EDS spectra obtained with Nd:11Fe:Ti material under the splat and splat/annealed materials. Averaged spectra resulting from 5 point analyses performed on (a) splat-quenched $NdFe_{11-x}Ti_y$ grains, (b) splat/annealed $NdFe_{11-x}Ti_y$ grains and (c) difference between splat/annealed and splat $NdFe_{11-x}Ti_y$ grains. The averaged spectra were normalized by equalizing the Nd counts.
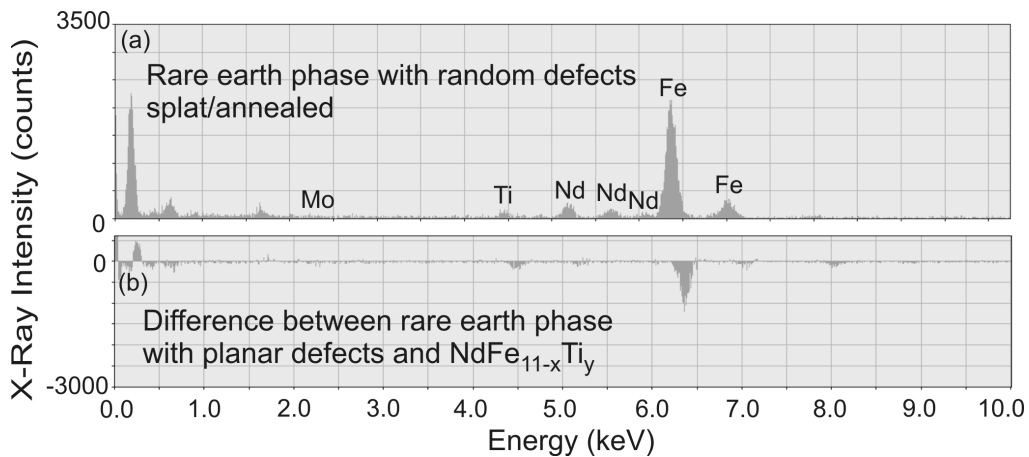

Figure 52 – (a) EDS spectra obtained with the Nd:11Fe:Ti splat/annealed material. Averaged spectrum resulting from 5 point analyses performed on grains exhibiting a random distribution of planar defects. (b) Difference between the defective grains average spectrum and the spectrum presented in Figure 51 (b). The averaged spectra were normalized by equalizing the Nd counts.

Electron microdiffraction experiments were also used to confirm that rare-earth grains with uniform contrast corresponded to the ThMn$_{12}$-type NdFe$_{11-x}$Ti$_y$ phase. Figure 53 presents the result of a set of diffraction experiments carried out in one of those crystallites, together with the respective simulated diffraction patterns.
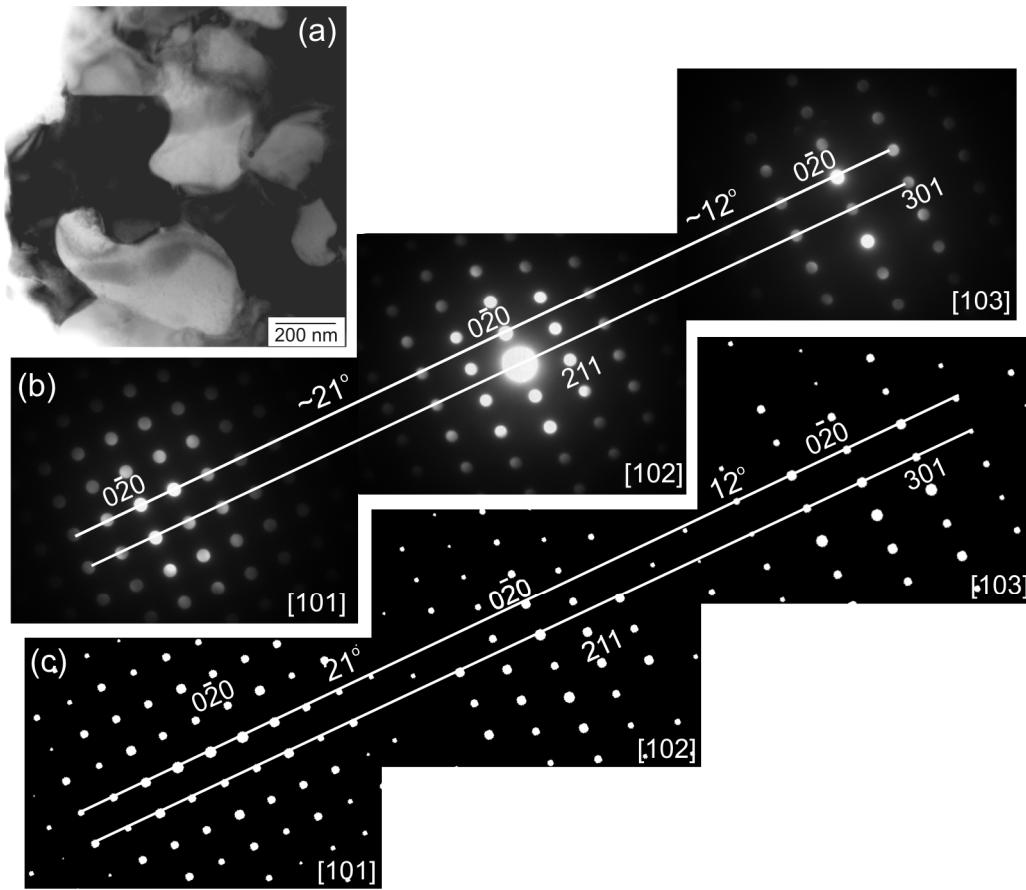

Figure 53 – (a) ThMn$_{12}$-type grain (dark contrast). (b) Microdiffraction patterns obtained by tilting the dark crystal in into 3 different low-index zone axes while keeping excited the $(0\bar{2}0)$ reflection. (c) Simulated diffraction patterns for a ThMn$_{12}$-type NdFe$_{11-x}$Ti$_y$ phase with 100 nm thickness.

A series of 3-D microdiffraction experiments has been obtained from crystallites presenting random distributions of planar defects. The indexed diffractograms obtained showed that the defective grains correspond to a fine mixture of the $ThMn_{12}$-type and Th_2Zn_{17}-type structures, exhibiting the following orientation relation:

$$(020)_{1:12}//(003)_{2:17} \text{ and } [100]_{1:12}//[110]_{2:17}$$

with the planar defects present on $(022)_{1:12}$ // $(3\bar{3}3)_{2:17}$ planes. Figures 54 to 59 present these results in detail together with the corresponding simulated patterns. A careful inspection reveals that in all cases the spots of both phases are perfectly indexed to individual reflections or can be assigned to the streaked rows.
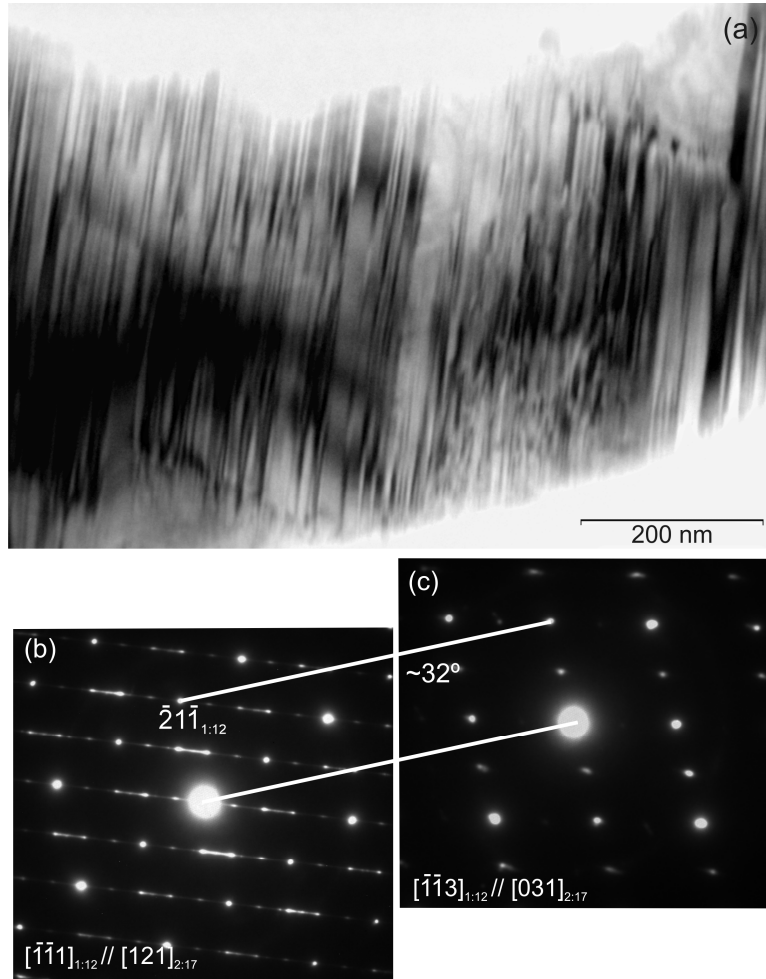

Figure 54 – (a) Grain with a random distribution of planar defects. (b) Experimental microdiffraction pattern obtained along $[\bar{1}11]_{1:12}$ // $[121]_{2:17}$. (c) Experimental microdiffraction pattern obtained along $[\bar{1}13]_{1:12}$ // $[031]_{2:17}$ after tilting ~32° from the previous orientation while keeping excited the $(\bar{2}1\bar{1})_{1:12}$ reflection.
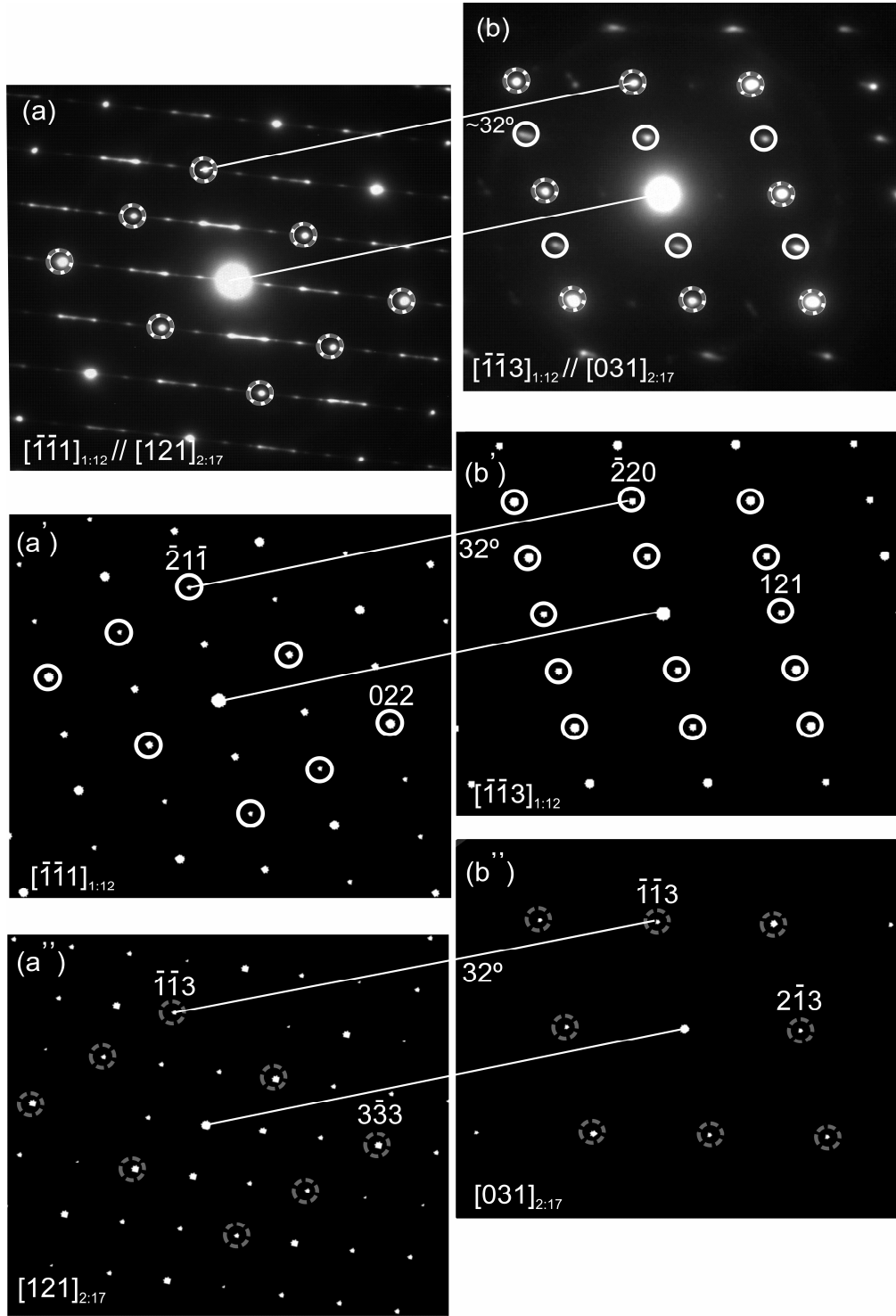
Figure 55 – (a) and (b) Experimental microdiffraction patterns of Figure 54, where the superposition of white and dashed-gray circles represents the match for reflections of a ThMn$_{12}$-type of structure and a Th$_2$Zn$_{17}$-type of structure, respectively. (a') Simulated diffraction pattern along a $[\bar{1}\bar{1}1]$ assuming a ThMn$_{12}$-type structure. (b') Simulated diffraction pattern along a $[\bar{1}\bar{1}3]$ assuming a ThMn$_{12}$-type structure. (a'') Simulated diffraction pattern along $[121]$ assuming a Th$_2$Zn$_{17}$-type structure (b'') Simulated diffraction pattern along $[031]$ assuming a Th$_2$Zn$_{17}$-type structure. The simulations were carried out for a 30 nm crystal thickness. Notice the planar defects lie on $(022)_{1:12}$ // $(3\bar{3}3)_{2:17}$.

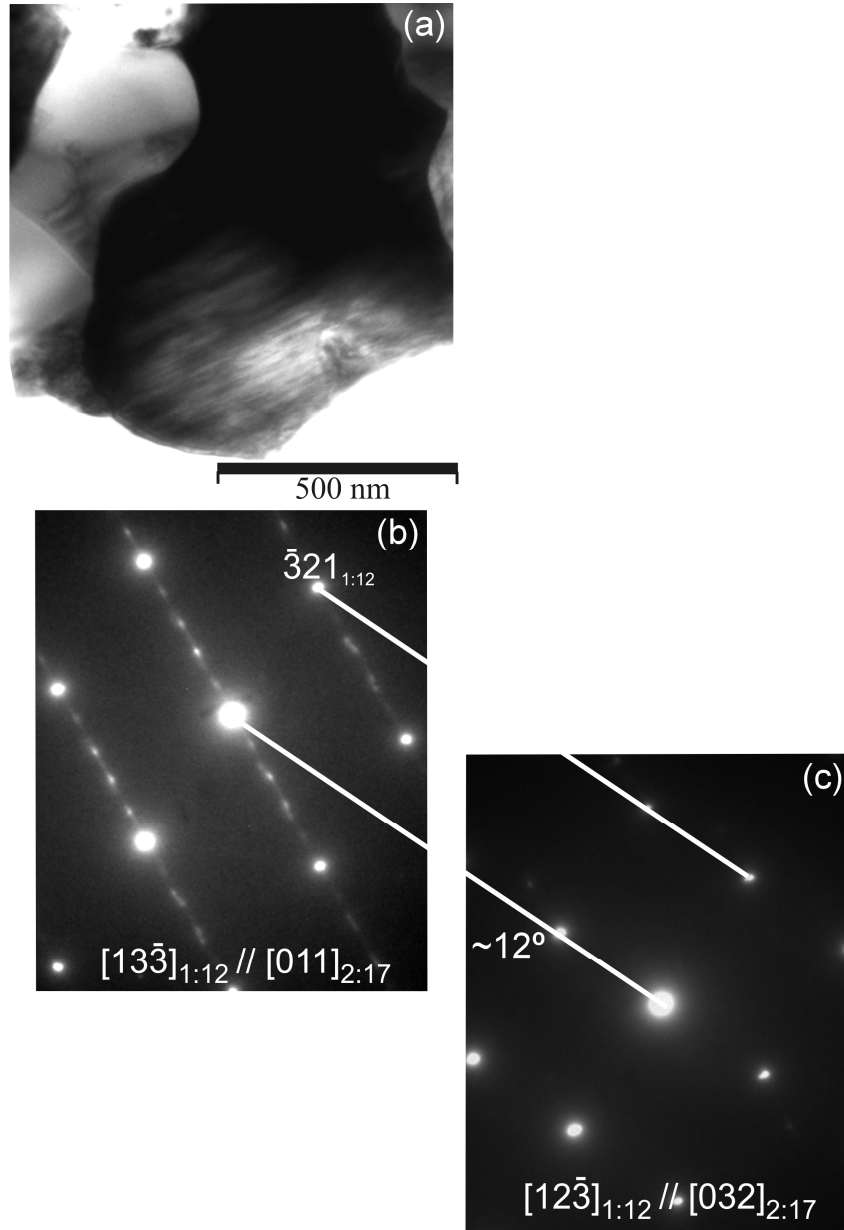Figure 56 – (a) Grain with a random distribution of planar defects. (b) Experimental microdiffraction pattern obtained along $[13\bar{3}]_{1:12}$ // $[011]_{2:17}$. (c) Experimental microdiffraction pattern obtained along $[12\bar{3}]_{1:12}$ // $[032]_{2:17}$ after tilting ~12° from the previous orientation while keeping excited the $(\bar{3}21)_{1:12}$ reflection.
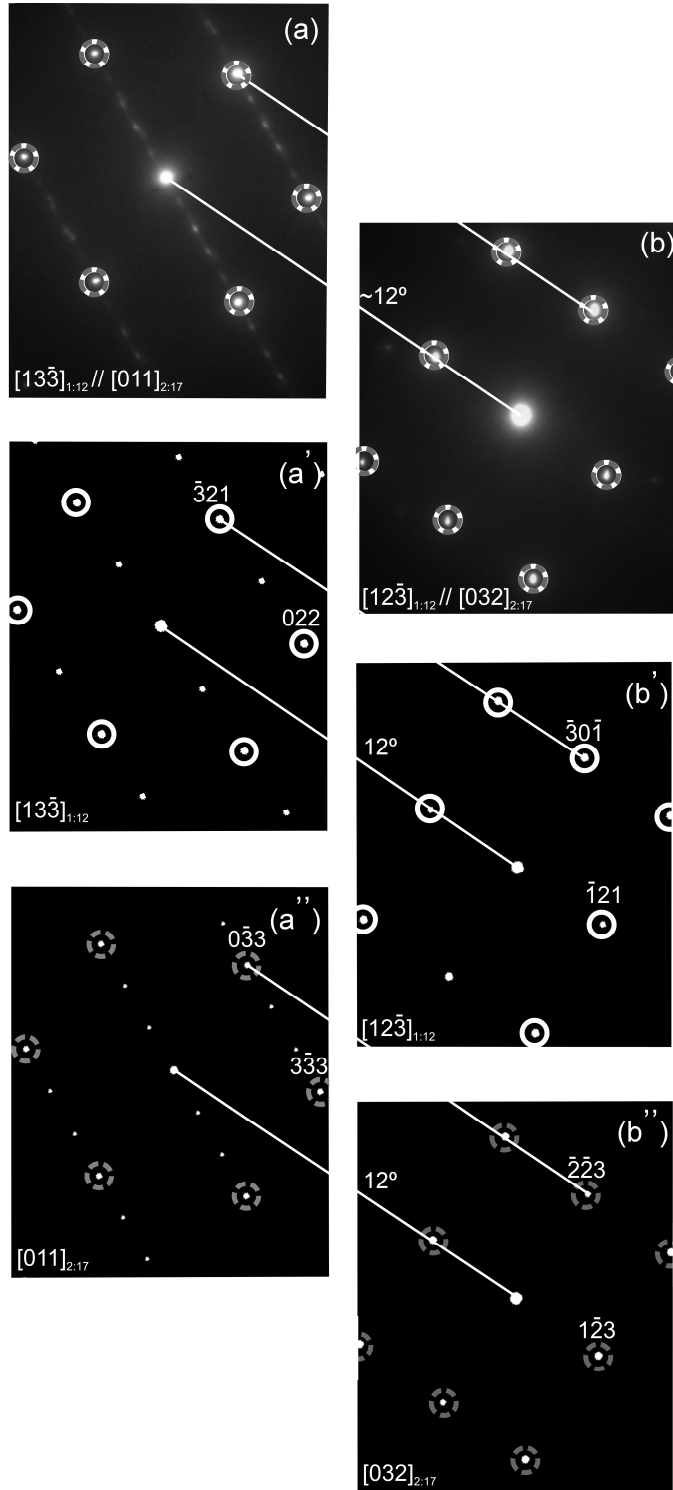
Figure 57 – (a) and (b) Experimental microdiffraction patterns of Figure 56, where the superposition of white and dashed-gray circles represents the match for reflections of a $ThMn_{12}$-type of structure and a Th_2Zn_{17}-type of structure, respectively. (a') Simulated diffraction pattern along $[13\bar{3}]$ assuming a $ThMn_{12}$-type structure. (b') Simulated diffraction pattern along $[12\bar{3}]$ assuming a $ThMn_{12}$-type structure. (a'') Simulated diffraction pattern along $[011]$ assuming a Th_2Zn_{17}-type structure. (b'') Simulated diffraction pattern along $[032]$ assuming a Th_2Zn_{17}-type structure. The simulations were carried out for a 30 nm crystal thickness. Notice the planar defects lie on $(022)_{1:12}$ // $(3\bar{3}3)_{2:17}$.
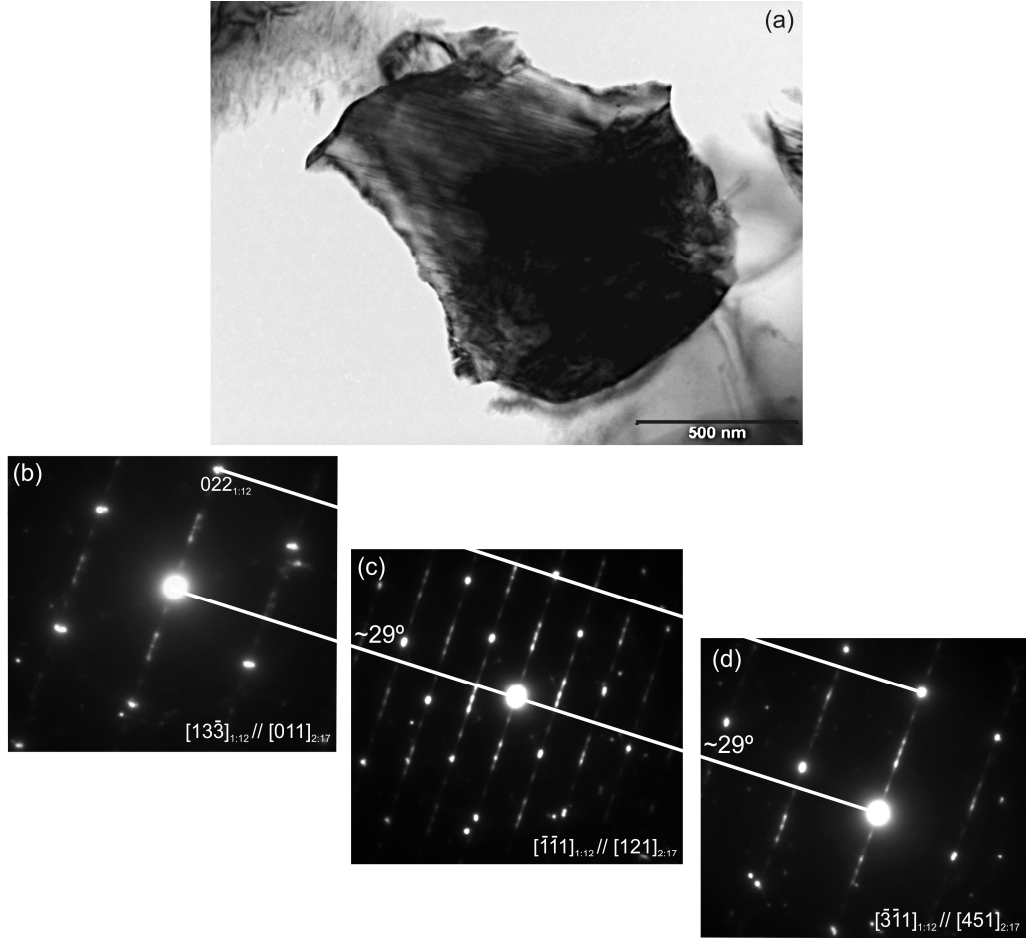
Figure 58 – (a) Grain with a random distribution of planar defects. (b) Experimental microdiffraction pattern along $[13\bar{3}]_{1:12}$ // $[011]_{2:17}$. (c) Experimental microdiffraction pattern along $[\bar{1}1l]_{1:12}$ // $[121]_{2:17}$ fter tilting ~29° from the previous orientation while keeping excited the $(022)_{1:12}$ reflection. (d) Experimental microdiffraction pattern along $[\bar{3}1l]_{1:12}$ // $[451]_{2:17}$ after tilting ~29° from the previous orientation while keeping excited the $(022)_{1:12}$ reflection.
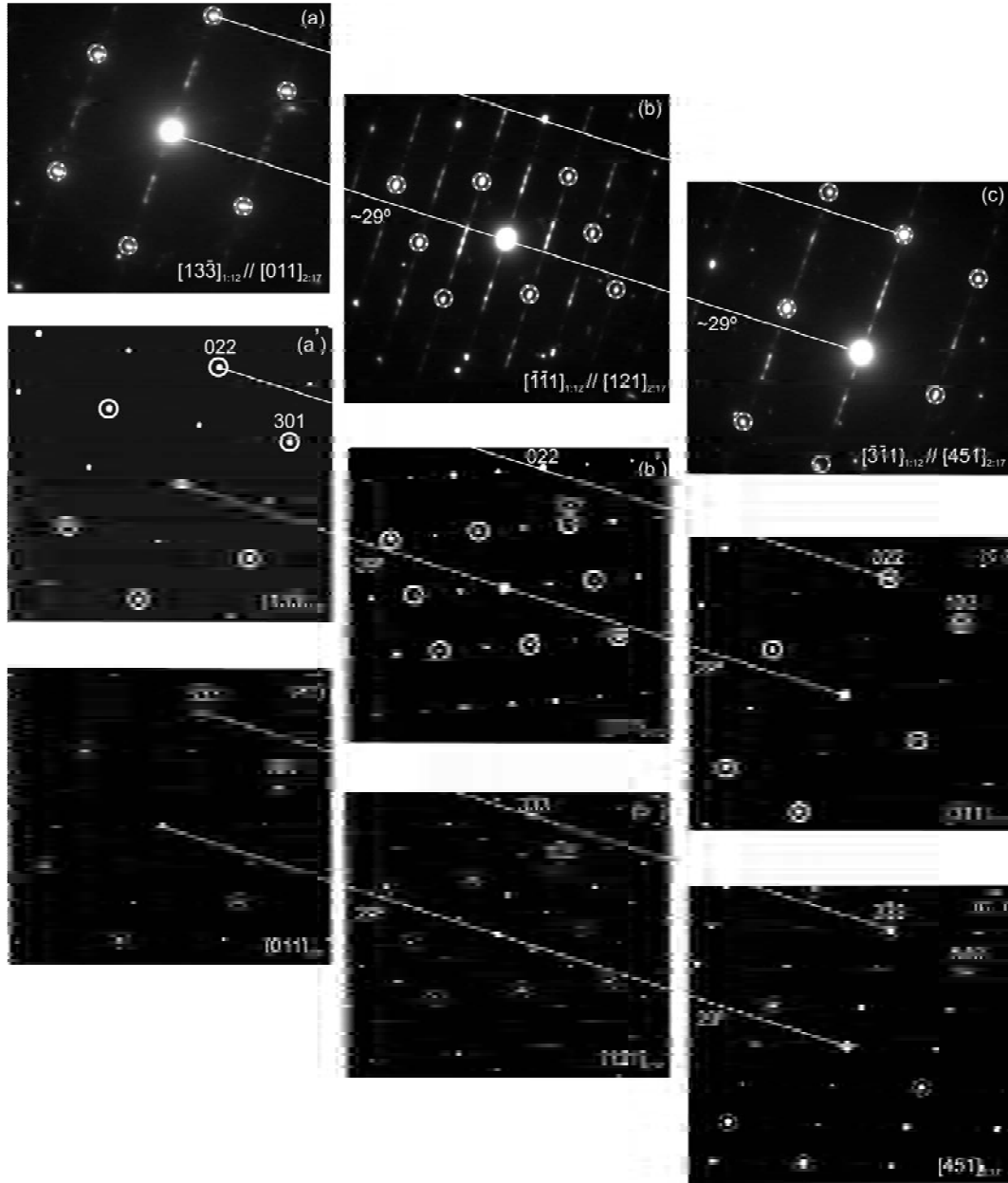
Figure 59 - (a), (b) and (c) Experimental microdiffraction patterns of Figure 58, where the superposition of white and dashed-gray circles represents the match for reflections of a $ThMn_{12}$-type of structure and a Th_2Zn_{17}-type of structure, respectively. (a') Simulated diffraction pattern along $[13\bar{3}]$ assuming a $ThMn_{12}$-type structure. (b') Simulated diffraction pattern along $[\bar{1}\bar{1}1]$ assuming a $ThMn_{12}$-type-type structure. (c') Simulated diffraction pattern along $[\bar{3}\bar{1}1]$ assuming a $ThMn_{12}$-type structure. (a'') Simulated diffraction pattern along $[011]$ assuming a Th_2Zn_{17}-type structure zone. (b'') Simulated diffraction pattern along $[121]$ assuming a Th_2Zn_{17}-type structure. (c'') Simulated diffraction pattern along $[451]$ assuming a Th_2Zn_{17}-type structure. The simulations were carried out for a 30 nm crystal thickness. Notice the planar defects lie on $(022)_{1:12}$ // $(3\bar{3}3)_{2:17}$.

Magnetization curves at room temperature obtained with the splat-quenched and splat/annealed materials are presented in Figure 60. The smooth appearance of the curves indicates that the magnetic phases, $NdFe_{11-x}Ti_y$, $Nd_2(Fe,Ti)_{17-w}$ and α-Fe(Ti), exhibit similar magnetization behavior with combined saturation magnetization (M_s) at 5 Tesla of 22.7 μ_B/fu and 17.5 μ_B/fu for the splat-quenched and splat/annealed conditions, respectively. These results are slightly higher than the value published in the literature for $NdFe_{11}Ti$, 16.8 μ_B/fu at 293K [1].
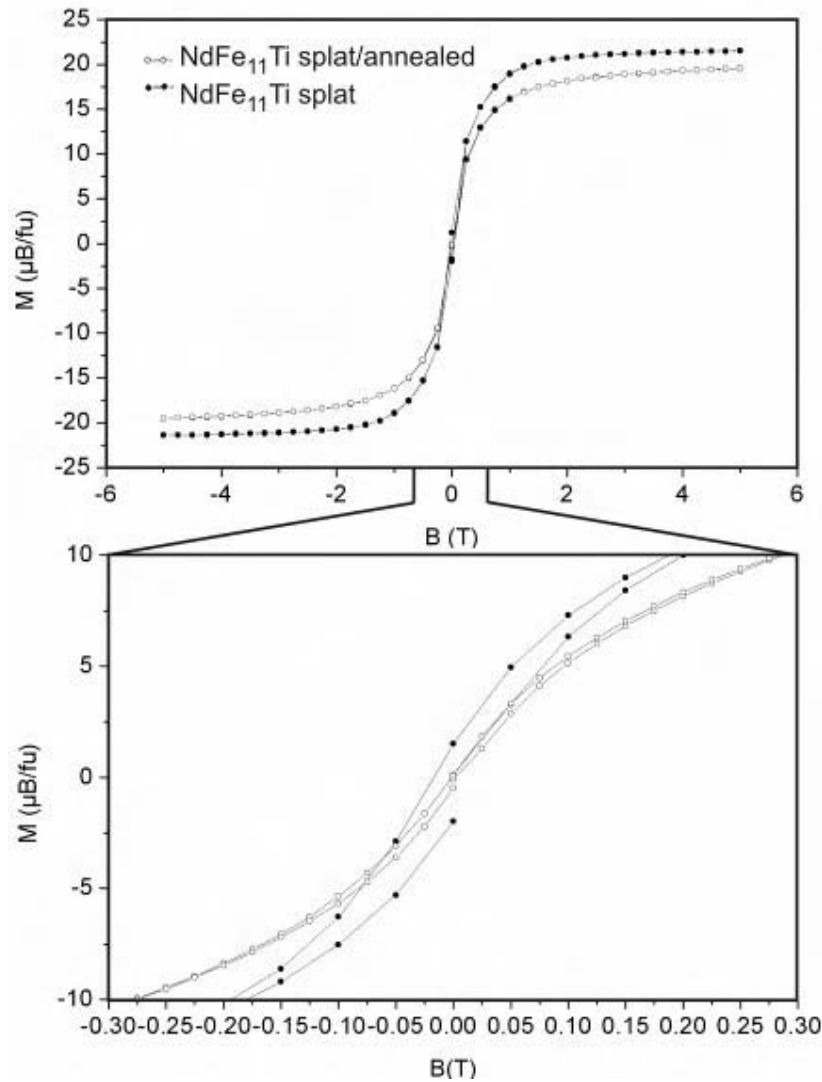

Figure 60 – Magnetic field dependence of the magnetization at 298 K for the splat-quenched and splat-annealed materials.

5.4. Discussion

Structural Stability

As with the Y:11Fe:Ti, and Y:11Fe:Mo alloys, the presence of α-Fe(Ti) in the Nd:11Fe:Mo alloy could not be avoided during solidification/heat-treatments. Nevertheless, and contrarily to these systems, the occurrence of another phase derived from $CaCu_5$, the Th_2Zn_{17}-type phase, could be detected in the as-cast, cast/annealed and splat/annealed conditions.

The microstructure morphologies and EDS results show that at moderate cooling rates a secondary crystallization phase, $Nd_2(Fe,Ti)_{17-w}$, appears in the Nd:11Fe:Ti alloy as result of a peritectic reaction. This lower temperature phase was however not detected in the splat-quenched material, where the high cooling rate route suppressed its crystallization. The results demonstrate that segregation occurred under both solidification routes and therefore that the cooling rate associated with splat-quenching was nevertheless too low to set the solid/liquid interface under the severe non-equilibrium conditions necessary to prevent partition.

Figure 61 presents a schematic explanation of the solidification path and solid state reactions observed:

- In the as-cast condition, the alloy crystallized forming primary α-Fe(Ti) dendrites, followed by $ThMn_{12}$-type $NdFe_{11-x}Ti_y$ and later by $ThZn_{17}$-type $Nd_2(Fe,Ti)_{17-w}$. The results indicate that the formation of the peritectic $Nd_2(Fe,Ti)_{17-w}$ phase was incomplete during the solidification route, since a solid state $ThMn_{12}$-type $\rightarrow$ $ThZn_{17}$-type + α-Fe(Ti) reaction occurred during the annealing treatment, together with the precipitation of Fe_2Ti crystallites close to the α-Fe(Ti)/rare-earth compound interfaces.
- In the splat-quenched condition, the high cooling rate suppressed completely the formation of $Nd_2(Fe,Ti)_{17-w}$ and only α-Fe(Ti) and $NdFe_{11-x}Ti_y$ were present. The subsequent heat-treatment induced also a $ThMn_{12}$-type $\rightarrow$ $ThZn_{17}$-type + α-Fe(Ti) reaction.

The solid state reaction produced a fine mixture of the two phases with (pseudo)invariant atomic planes at $(022)_{1:12}$ // $(3\bar{3}3)_{2:17}$, indicating that the transformation has a partly displacive character.
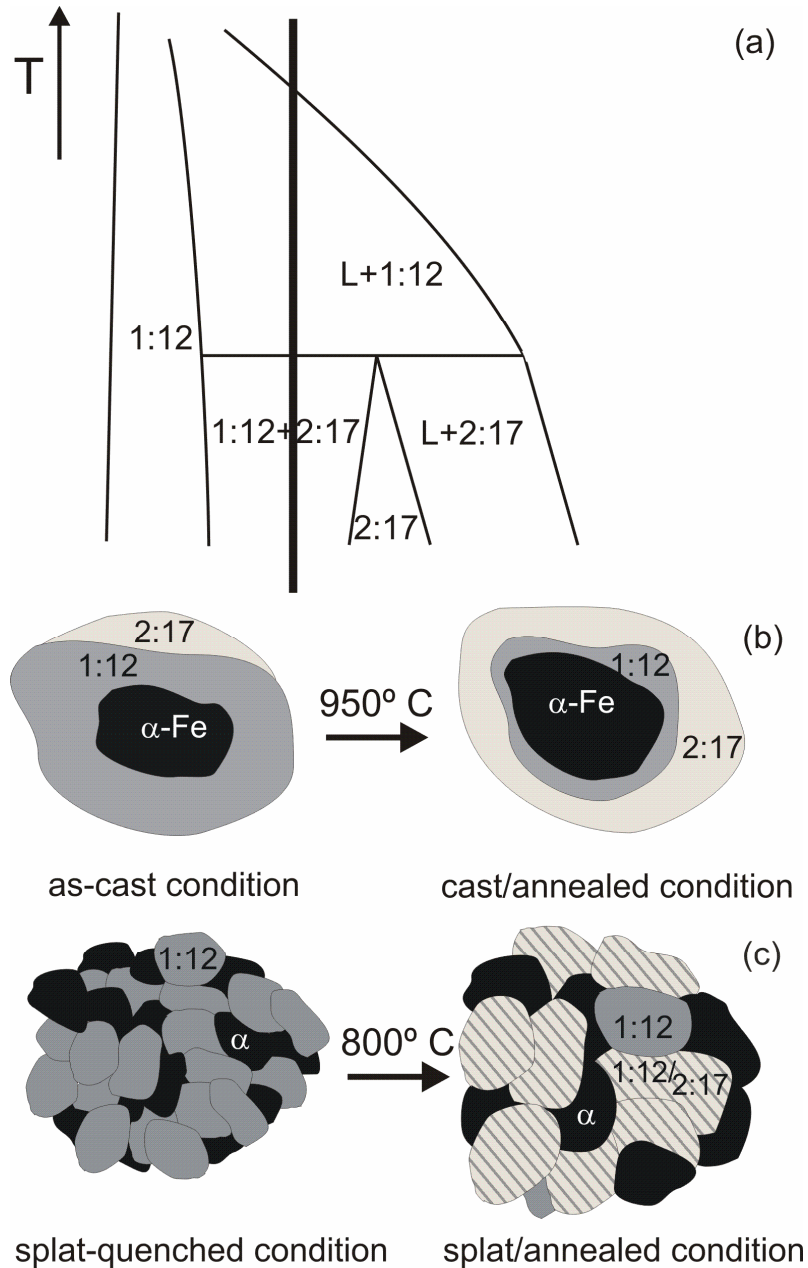

Figure 61 – (a) Scheme of the solidification path and solid state reactions (b) Phase configurations transformation in the as-cast material before and after heat treatment. (c) Phase configurations in the splat-quenched material before and after heat treatment.

The domain contrast in the phase images showed no correlation with the surface topography and, moreover, no phase contrast difference was detected after changing scan direction. Domain (and not wall) contrast was detected due to the fact that the scale of the domain configurations is comparable to the scan height (60 nm). The undulation of the maze domains near the surface observed in Figure 43 (b) results from reduction in the magnetostatic energy at the cost of a larger total Bloch wall area [72]. The grain with stripe domains in the central part of Figure 43 (b) is surrounded by a softer phase with a domain configuration, exhibiting an accommodation to the demagnetizing fields of the striped grain. This softer phase, which is expected to be α-Fe(Ti) presents domain branching at the grain boundary with antiparallel alignment of the magnetization on either side.

The fine domain configuration of Nd:11Fe:Ti splat-quenched material reveals that the magnetic domains correspond roughly to individual crystallites (compare Figures 44 and 45) . Therefore, formation of domain walls in the fine crystallites is energetically unfavorable and domain walls have been essentially expelled to the grain boundaries. The results indicate that the critical size for single-domain behavior around 200 nm.

The values of coercivity and saturation magnetization obtained for the Nd:11Fe:Ti alloy under the splat condition are slightly higher than the ones obtained for the other alloys. Nevertheless, the low coercivity obtained for Nd:11Fe:Ti demonstrates high domain mobility and therefore that grain boundaries and planar defects are not effective pinning sites for domain walls. In particular, no pinning effect by the planar defects present in $NdFe_{11-x}Ti_y/Nd_2(Fe,Ti)_{17-w}$ could be detected in the MFM observations.

5.5. Summary

- The as-cast and splat-quenched materials crystallized essentially adopting the $ThMn_{12}$-type structure, though the $RFe_{11}M$ stoichiometry was not strictly followed. The Th_2Zn_{17-w}-type $Nd_2(Fe,Ti)_{17-w}$ phase could also be detected in the as-cast microstructure.

- Nd:11Fe:Ti splat-quenched material presented a fine microstructure composed of α-Fe(Ti) and $NdFe_{11-x}Ti_y$ crystallites while no Fe_2Ti or $Nd_2(Fe,Ti)_{17-w}$ could be detected. Under this condition, the grain size for both α-Fe(Ti) and $NdFe_{11-x}Ti_x$ lied typically within 100 to 200 nm. MFM showed a fine domain configuration in bulk surfaces in agreement with the microstructural scale.

- The annealing treatments induced a $NdFe_{11-x}Ti_y \rightarrow Nd_2(Fe,Ti)_{17-w} + \alpha$-Fe(Ti) transformation as well precipitation of Fe_2Ti.

- The solid state reaction produced a fine mixture of the two phases with (pseudo)invariant atomic planes at $(022)_{1:12}//(3\bar{3}3)_{2:17}$, indicating that the solid state transformation has a partly displacive character.

- The coercivity and saturation magnetization measured for the Nd:11Fe:Ti alloy under the splat condition are slightly higher than the ones obtained for the other alloys. Nevertheless, the still low coercivity demonstrates that grain boundaries and planar defects are not effective pinning sites for domain walls.

6. Conclusions

- All the as-cast and splat-quenched materials crystallized adopting essentially the $ThMn_{12}$-type structure. However, the $RFe_{11}M$ stoichiometry was not strictly followed.

- The variation of the α-Fe phase proportion in the studied conditions demonstrates homogeneity ranges, which together with the limited latticed parameter evolutions, supports the hypothesis of iron vacancies in the $ThMn_{12}$-type structure.

- At the finer microstructural scales, the observed magnetic domains corresponded essentially to single crystallites, indicating that single domain behaviour occurs for sizes between 100-200 nm in all the phases.

- Vortex configurations resulting from accommodation to the demagnetizing fields of neighboring $RFe_{11-x}M_y$ were common in large α-Fe(Ti)/ α-Fe(Mo) grains under thin film form. Out-of-plane Bloch and in-plane Néel character could be detected in the vortex walls.

- Planar defects with twin appearance and other 2-D defects displaying the strong contrast and contours characteristic of thermal antiphase boundaries have been observed in $YFe_{11-x}Ti_y$ grains.

- A domain wall energy of 8-17 mJ/m^2 has been estimated for $YFe_{11-x}Ti_y$.

- A L + $ThMn_{12}$-type $\rightarrow$ $ThZn_{17}$-type peritectic reaction occurred during the arc-furnace solidification of the Nd:11Fe:Ti alloy. A subsequent heat-treatments induced a $ThMn_{12}$-type $\rightarrow$ $ThZn_{17}$-type + α-Fe(Ti) solid state reaction.

- The solid state reaction produced a fine mixture of $ThMn_{12}$ and $ThZn_{17}$-type phases with (pseudo)invariant atomic planes at $(022)_{1:12}$//$(3\bar{3}3)_{2:17}$, indicating that the solid state transformation has a partly displacive character.

- The coercivity and saturation magnetization measured for the Nd:11Fe:Ti alloy under the splat condition are slightly higher than the ones obtained for the other alloys. Nevertheless, the overall low coercivity demonstrates that grain boundaries and planar defects are not effective pinning sites for domain walls in any of the compounds.

7. References

[1] H.S. Li, J.M.D. Coey, Handbook of Magnetic Materials, Vol. 6 (ed. K. H. J. Buschow), North-Holland, Amsterdam, 1991

[2] W. Suski, Handbook on the Physics and Chemistry of Rare Earths, Vol. 22 (eds. K.A. Gschneidner Jr, L. Eyring), North-Holland, Amsterdam, 1996

[3] Y.C. Yang, X.D. Zhang, L.S. Kong, Q. Pan, S.L. Ge, J. Appl. Phys. Lett. 58 (1991) 2042

[4] D.P.F. Hurley, J.M.D. Coey, J. Phys.: Condens. Matter 4 (1992) 5573

[5] O. Isnard, S. Miraglia, M. Guillot, D. Fruchart, J. Alloys Comp. 277 (1998) 637

[6] A.S. Fernando, J.P. Woods, S.S. Jaswal, D. Welipitiya, B.M. Patterson, and D.J. Sellmyer, J. Appl. Phys. 75 (1994) 6303

[7] H. Sun, Y. Morii, H. Fuji, M. Akayama, and S. Funahashi, Phys. Rev. B. 48 (1993) 13333

[8] C. Abadia, P.A. Algarabel, B. Garcia-Landa, M.R. Ibarra, A. del Moral, N.V. Kudrevatiykh, P.E. Martin, J. Phys.: Condens. Matter. 10 (1998) 349

[9] B.P. Hu, H.S. Li, J.P. Gavigan, J.M.D. Coey, J. Phys. C: Condens Matter, 1 (1989) 755

[10] E.B. Boltich, B.M. Ma, L.Y. Zhang, F. Pourarian, S.K. Malik, S.G. Sankar, W.E. Wallace, J. Magn. Magn. Mater. 78 (1989) 364

[11] L.Y. Zhang, E.B. Boltich, V.K. Sinha, W.E. Wallace, IEEE Trans. Mag. 25 (1989) 3303

[12] B.P. Hu, H.S. Li, J.M.D. Coey, J. Appl. Phys. 67 (1990) 4838

[13] X.C. Kou, T.S. Zhao, R. Grossinger, H.R. Kirchmayr, X. Li, F.R. Boer, Phys. Rev. B, 47 (1993) 3231

[14] R. Grossinger, X. C. Kou, G. Wiesinger, IEEE Trans. Mag. 30 (1994) 1018

[15] K. Shimizu, F. Ogasawara, K. Ichinose, Physica B 237-238 (1997) 584

[16] A.V. Andreev, S.M. Zadvorkin, Phil Mag B, 77 (1998) 147

[17] S.A. Nikitin, T.I. Ivanova, I.S. Tereshina, Inorg. Mater. 34 (1998) 458

[18] V. Zubenko, I. Tereshina, I. Telegina, E. Tereshina, D. Luchev, N. Pankratov

[19] S.A. Nikitin, I.S. Tereshina, V.N.Verbetski, A.A. Salamova, J. Alloy Comp. 316 (2001) 46

[20] C. Piquer, F. Grandjean, O. Isnard, G.L. Long, J. Appl. Phys. 93 (2003) 3414

[21] C. Piquer, R.P. Hermann, F. Grandjean, O. Iisnard, G.J. Long, J. Phys.: Condens. Matter 15 (2003) 7395

[22] I.S. Tereshina, S.A. Nikitin, G.A. Bezkorovajnaja, W. Suski, D. Badurski, Phys. Stat Sol. 236 (2003) 462

[23] J. Chaboy, M.A. Laguna-Marco, C. Sanchez, Phys. Rev B 69 (2004) 134421

[24] MA. Laguna-Marco, J. Chaboy, M.C. Sanches, H. Maruyama, N. Kkawamura, M. Suzuki, J. Magn. Magn. Mater. 272-276 (2004) 2144

[25] P. Qian, N.-X. Chen, J. Shen, Solid Stat Comm, 134 (2005) 771

[26] C.Piquer, F.Grandjean, G.J. Long, O. Isnard, J. Alloys Comp. 388, (2005) 6

[27] Y.Z. Wang, B.P Hu and G.C. Liu, W.Y Lai, J. Appl. Phys. 76 (1994) 6383

[28] W. Mao, J.Yang, B. Cheng, Y. Yang, H. Du, Y. Xue, B. Zhang, C. Ye, and J. Yang, J. Phys.: Condens. Matter 10 (1998) 4379-4385

[29] Y.C. Wang, Y.G. Xiao, J.Y. Zhang, G.Y. Liu, J.B. Li, and G.H Rao, J. Magn. Magn. Mater, 313 (2007) 107

[30] S. Jaswal. Phys. Rev. B 48 (1993) 6156

[31] Z.Q. Jin, W. Tang, J. R. Zhang, H. X. Qin, and Y.W. Du. Eur. Phys. J. B. 3 (1998) 41

[32] A. Amirabadizadeh, N. Tajabor, M.R. Alinejd, H. Salamati, and F. Pourarian. Phys. Stat. Sol. 201 (2004) 121

[33] M.R. Jian, T.S Chin, J.L. Tsai, H.W. Zhang, and B-G. Shen. J. Magn. Magn. Mater. 209 (2000) 205

[34] N. Tajabor, A. Amirabadizadeh, M.R. Alinejad, H. Salamati, and F.Pouraian. J. Magn. Magn. Mater. 272 (2004) 2093

[35] T.S. Chin, W.C. Chang, H.C. Ku, C.C. Weng, H.T. Lee, and M.P. Hung. IEEE Trans. Mag. 25 (1989) 3300

[36] S.-H. Huang, T.-S. Chin, J. Appl. Phys. 70 (1991) 4439

[37] Y.B. Kim, S. Sugimoto, M. Okada, M. Homma, J. Alloys Comp. 176 (1991) 215

[38] A. Margarian, J. B. Dunlop and R. K. Day, W. Kalceff, J. Appl. Phys. 76 (1994) 15

[39] E.W. Singleton, J. Strzeszewski, G.C. Hadjipanayis, D.J. Sellmeyer, J. Appl. Phys. 64 (1988) 5717

[40] C.D. Meekison, J.P. Jakubovics, J.M.D. Coey, J. Ding, J. Magn. Magn. Mater. 104 (1992) 1161

[41] Y.G. Pastushenkov, K.P. Skokov, Y. Skourski, L. Lebedeva, T. Ivanova, A. Grushichev, K.-H. Müller, J. Magn Magn. Mater. 300 (2006) e500

[42] C. Koestler, L. Schultz, G. Thomas, J. Appl. Phys. 67 (1990) 2532

[43] L Kepinski, W. Suski, K.J. Wochowski, J. Alloys Comp. 213 (1994) 520

[44] J. Yang, W.Mao, B. Cheng, Y. Yang, H. Xu, B. Han, S. Ge, W. Ku, Appl. Phys. Lett. 71 (1997) 3290

[45] S.L.Tang, C.H. Wu, B.W.Wang, X.M. Jin, G.s. Li, B.Z. Ding, Y.C. Chuang, J. Mag. Mag Mater. 188 (1998) 387

[46] J. Hu, T. Dragon, A. Forkl, H. Kronmüller, Phys. Stat. Sol. (a), 154 (1996) 749

[47] M.R. Jian, T.S Chin, J.L. Tsai, H.W. Zhang, and B-G. Shen. J. Magn. Magn. Mater. 209 (2000) 205

[48] T. Horikawa, K. Miura, M. Itoh, K.I. Machida, IEEE Trans. Mag. 41 (2005) 2064

[49] D.Brandon, and W.D.Kaplan. Microstructural charecterization of materials, John Wiley and sons, Chichester (1999)

[50] J. I. Goldstein, D. E. Newbury, P. Echlin, D.C. Joy, C. Fiori, and E. Lifshin. Scanning Electron Microscopy and X-Ray Microanalysis, Plenum Press, New York (1981).

[51] J.N. Chapnam, Mater. Sci. Eng. B3 (1989) 355

[52] D. Paganin, K. Nugent, Phys. Rev. Lett. 80 (1998) 2586

[53] M.R. Teague, J. Opt. Soc. Am. 72 (1982) 1199

[54] V.V. Volkov, Y. Zhu, M de Graef, Micros (2002) 411

[55] R. Wiesendanger, Scanning Probe Microscopy and Spectroscopy, Cambridge University Press, Cambridge (1994)

[56] P. Grütter, H. J. Mamin and D. Rugar in Scanning Tunnelling Microscopy II, edited by R. Weisendanger and H.-J. Güntheroft (Springer, Berlinm 1992) pp.151-207.

[57] W. Krauss, G. Nolze, J. Appl. Cryst. 29 (1996) 301

[58] D. Villars, L. D. Calvert. "Pearson's Handbook of Crystallographic Data for Intermetallic Phases", 2nd ed, Vol 2, ASM International

[59] R. Coehoorn, Phys Rev B, 39 (1989) 13072

[60] L.X. Liao, Z. Altounian, D.H. Ryan, Phys. Rev. B47 (1993) 11230

[61] W.B. Yelon, Z. Hu, J. Appl. Phys. 79 (1996) 1330

[62] H.S. Li, D. Courtois, J.M. Cadogan, J.M. Xu, S.X. Dou, J. Phys.: Condens. Matter 6 (1994) L771

[63] Y. Luo, N. Zhang, J. Appl. Phys. 61 (1987) 3445

[64] M. H. Yu, Z. D. Zhang, Q. F. Xiao, W. Liu, and X. G. Zhao, J. Appl. Phys, 88 (2000) 4226

[65] W. Kurz, D. J. Fisher, Fundamentals of Solidification, Trans Tech Publications, 3rd edition, Aedermannsdorf, Switzerland (1992)

[66] T.S.Jang, H.H. Stadelmaier, J. Appl. Phys. 67 (1990) 4957

[67] A. Müller, J. Appl. Phys. 64 (1988) 249

[68] M. Zinkevich, N. Mattern, B. Wolf, K. Wetzig, Phys. Stat. Sol. (a) 178 (2000) 671

[69] B.K Vainshtein, V.M. Fridkin, V.L. Indenbom, Modern Crystallography II, Structure of crystals, Springer-Verlag, Berlin, 1982, Vol. 21, p. 71

[70] M. Solzi, l.Pareti, O. Moze, W.I.F. David, J. Appl. Phy. 64 (1988) 5084

[71] L. Folks, R. C. Woodward, J. Magn Magn. Mater.190 (1998) 28

[72] W. Szmaja, J. Magn Magn. Mater., 301 (2006) 546

[73] Y. Zhu, V.V. Volkov, M. De Graef, J. Electron Mic 50 (2001) 447.

[74] C. Kittel Phys. Rev. 70 (1946) 965

[75] C. Kooy and U. Enz, Philips Res. Rep. 15,(1960) 7

[76] R. Szymczak, J. Appl. Phys. 39 (1968) 875

[77] W. Szmaja, J. Grobelny, M. Cichomski, Appl. Phys. Lett. 85 (2004) 2878

[78] J. Kaczér, Sov. Phys. JETP 19 (1964) 1204

[79] B. Garcia-Landa, D. Fruchart, D. Gignoux, J.L. Soubeyrux, and R. Vert, J. Magn Magn. Mater.182 (1998) 207-215

[80] X. Xu, R. Tucker, and S.A. Shahenn, J. Appl. Phys. 75 (1994) 6021

[81] R. Lorenz and J. Hafner, J.Appl. Phys. 78 (1996) 5051

[82] J. A. de Campos, L. P. Ferreira, M. M. Cruz, J. M. Gil, P. J. Mendes, I. C. Ferreira, M. Bacmann, J-L Fruchart, M. Godinho, and N. A. de Campos. J. Phys. Consens Matter II (1999) 687

[83] N. Tajabor, A. Amirabadizadeh, M.R. Alinejad, H. Salamati, and F.Pouraian. J. Magn. Magn. Mater. 272 (2004) 2093

[84] T.S. Chin, W.C. Chang, H.C. Ku, C.C. Weng, H.T. Lee, and M.P. Hung. IEEE Trans. Mag. 25 (1989) 3300